DEVELOPMENT OF A FUEL-POWERED COMPACT

SMA (SHAPE MEMORY ALLOY) ACTUATOR SYSTEM

A Dissertation

by

HYOUNG YOLL JUN

Submitted to the Office of Graduate Studies of
Texas A&M University
in partial fulfillment of the requirements for the degree of

DOCTOR OF PHILOSOPHY

December 2003

Major Subject: Aerospace Engineering

DEVELOPMENT OF A FUEL-POWERED COMPACT

SMA (SHAPE MEMORY ALLOY) ACTUATOR SYSTEM

A Dissertation

by

HYOUNG YOLL JUN

Submitted to Texas A&M University
in partial fulfillment of the requirements
for the degree of

DOCTOR OF PHILOSOPHY

Approved as to style and content by:

Othon K. Rediniotis	Dimitris C. Lagoudas
(Co-Chair of Committee)	(Co-Chair of Committee)
Gerald Morrison	Sai Lau
(Member)	(Member)
Walter Haisler	
(Head of Department)	

December 2003

Major Subject: Aerospace Engineering

ABSTRACT

Development of a Fuel-Powered Compact

SMA (Shape Memory Alloy) Actuator System. (December 2003)

Hyoung Yoll Jun, B.S., Inha University;

M.S., Inha University, Inchun, Korea

Co-Chairs of Advisory Committee: Dr. Othon K. Rediniotis
                                   Dr. Dimitiris C. Lagoudas

The work presents investigations into the development of a fuel-powered compact SMA actuator system. For the final SMA actuator, the K-alloy SMA strip (0.9 mm x 2.5 mm), actuated by a forced convection heat transfer mechanism, was embedded in a rectangular channel. In this channel, a rectangular piston, with a slot to accommodate the SMA strip, ran along the strip and was utilized to prevent mixing between the hot and the cold fluid in order to increase the energy density of the system. The fuel, such as propane, was utilized as main energy source in order to achieve high energy and power densities of the SMA actuator system. Numerical analysis was carried out to determine optimal channel geometry and to estimate maximum available force, strain and actuation frequency. Multi-channel combustor/heat exchanger and micro-tube heat exchanger were designed and tested to achieve high heat transfer rate and high compactness. The final SMA actuator system was composed of pumps, valves, bellows, multi-channel combustor/heat exchanger, micro-tube heat exchanger and control unit. The experimental tests of the final system resulted in 250 N force with 2 mm

displacement and 1.0 Hz actuation frequency in closed-loop operation, in which the hot

and the cold fluid were re-circulated by pumps.

I would like to dedicate this work to my parents and my family

for their constant love and support.

ACKNOWLEDGMENTS

TABLE OF CONTENTS

LIST OF FIGURES

Page

Page

LIST OF TABLES

CHAPTER I

INTRODUCTION

1. SMA (Shape Memory Alloy)

1.1. Introduction to SMAs

SMAs are metallic alloys that can recover permanent strain by changes either in stress, temperature or a combination of both [1, 2]. These changes induce a phase transformation. The main characteristic of all SMAs is the occurrence of a martensite phase transformation, which means the phase transformation from austenite phase to martensite phase. The martensite phase is low temperature phase, can be easily deformed and is low-symmetric state, while the austenite is high temperature phase, is relatively hard and is high symmetric state.

Martensite
(monoclinic)

Austenite
(cubic)
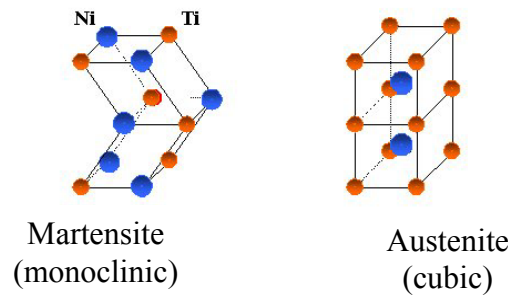
Figure 1. Crystalline structure of the two possible phases of Nitinol.

_____

This dissertation follows the format of *Smart Materials and Structures*.

This martensite transformation is a shear dominant diffusionless solid to solid phase transformation induced by nucleation and growth of the martensite phase from the parent austenite phase [3]. During the transformation, SMAs exhibit and recover considerable amounts of strain.

Figure 1 shows the crystalline structures of the two possible phases of NiTi SMA. The most commonly used type of the SMAs is Nitinol, composed of nearly 50 % nickel and 50 % titanium [4]. Nitinol was the shape memory alloy that was discovered in 1961 [5] and was less expensive, easier to work with and less dangerous compared to previously discovered alloys such as Au-Cd alloys [5]. This name comes from the two element symbols, Ti and Ni, and the abbreviation of the lab where it was discovered, Naval Ordinance Laboratories (NOL) [5]. The shape memory properties of Nitinol become evident once a specimen has been properly annealed. Shape memory alloys have two typical material characteristics, Shape Memory Effect (SME) and pseudoelasticity.

Figure 2 shows SMA stress-temperature phase diagram and phase transformation processes, which were schematically represented in this phase diagram. The phase transformation can be induced thermally without any applied stress as shown in Figure 2 (thermally induced transformation at zero stress). This kind of martensite transformation starts at a temperature value of M^{os} (martensite start), and finishes when SMA reaches a temperature value of M^{of} (martensite finish). During the heating from the martensite phase (M$\rightarrow$A), the austenite begins at a temperature of A^{os} (austenite start) and it is fully transformed when SMA reaches a temperature of A^{of} (austenite finish) as shown in

Figure 2. The stored elastic energy causes the spreading of the cycle (A^{of}- A^{os}), while the energy dissipated during the transformation associates with hysteresis (A^{os}- M^{of}) [6].

If there is no applied stress during the cooling from austenite to below M^{os}, the grains of material form a twinned structure by arranging themselves symmetrically across grain boundaries as shown in Figure 3. During the twining, there is no observable macroscopic shape change. By applying sufficient force, the twinned structure of matenisite will be forced to yield and reorient (detwin) to detwinned structure, in which all grains are aligned in one direction such as shown in Figure 3. During detwinning, large macroscopic inelastic strain is observed. Also the detwinned martensite can be generated by pure stress loading (Stress Induced Martensite, SIM) from a temperature above M^{os}. The transformation temperatures are function of stress as shown in Figure 2.
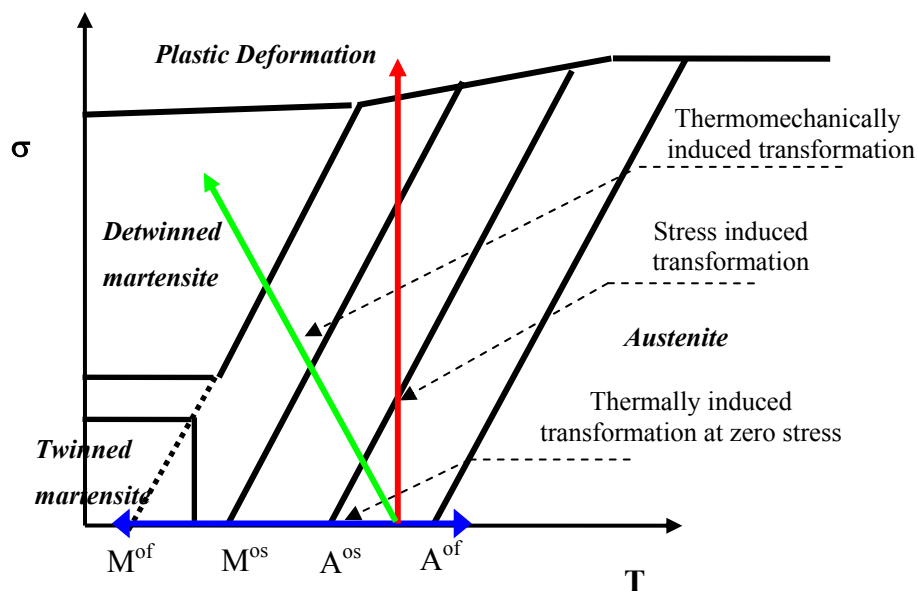
Figure 2. SMA stress-temperature phase diagram.
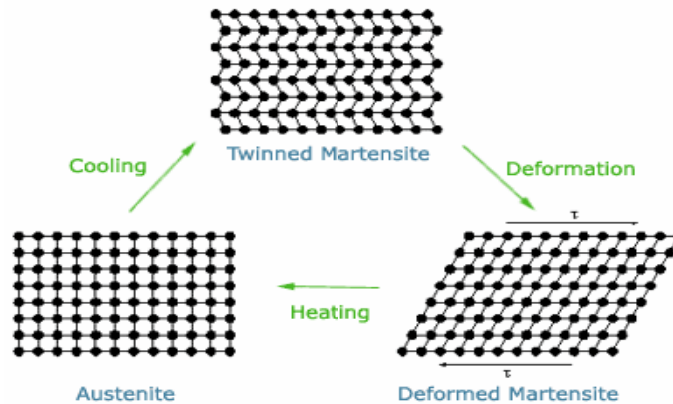
Figure 3. Material crystalline arrangement during the Shape Memory Effect [5].

1.1.1. Shape Memory Effect (SME)

The basis of SME is phase transformation between two phases, i.e., the martensite phase at low temperatures, and the austenite phase at high temperatures. The SMA alloys can be plastically deformed at martensite phase and then be heated to return to, or remember their original memorized configurations [6]. The SME can be defined as a one-way effect or a two-way effect.

1.1.1.1. One-way effect

Heating an SMA, which is deformed at matensite phase (twinned martensite to detwinned martensite as shown in Figure 3), above austenitic finish temperature will allow it to recover to its original memorized shape (detwinned martensite to austenite as shown in Figure 3). This is called the one-way shape memory effect (or simply, shape memory effect) because the shape recovery is achieved only during heating. Figure 4

shows schematic of a stress-strain-temperature curve showing this shape memory effect (one-way effect).

The first step (cooling in Figure 4) induces the development of the self-accommodated martensitic structure, twinned martensite, from the austenite and no macroscopic shape change is observed. The second step (loading) induces the dewinned martensite through the reorientation of the variants to a single variant by the mechanical loading from the twinned martensite and results in a large inelastic strain as shown in Figure 4. The last step (heating) causes the reverse transformation to austenite and the inelastic strain is recovered.
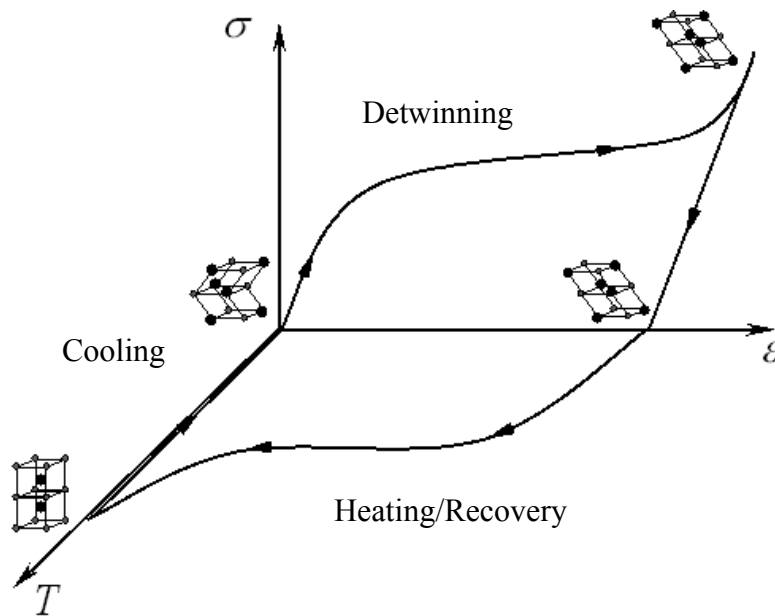
Figure 4. Schematic of a stress-strain-temperature curve showing the Shape Memory Effect (one-way effect) [6].

1.1.1.2. Two way effect

Thermomehanical cycling of the SMAs, which is called training, can make SMAs remember a stable shape at high temperature ($T>A^{of}$) and another stable shape at low temperature ($T<M^{of}$) [7]. This is called as two way shape memory effect (TWSME). These shape changes are obtained without any mechanical loading. The thermomechanical cycling of the SMAs induces the creation of defects and dislocations that lead to the preferential appearance of certain variants of martensite [6,7]. Thus during the cooling, the SMAs keep a stable shape at low temperature.

1.1.2. Pseudoelasticity

Another special property of SMAs is pseudoelasticity. During loading, an SMA can be strained up to substantial amounts (around 6%) due to SIM (stress induced martensite), and revert to its austenite shape without permanent plastic deformation during unloading. This behavior of SMA is observed during loading and unloading above A^{os}. Figure 5 shows a pseudoelasticity of an SMA wire during isothermal loading and unloading. During the stress induced martensite from point 1 to point 2, the SMA can be deformed to large strain.
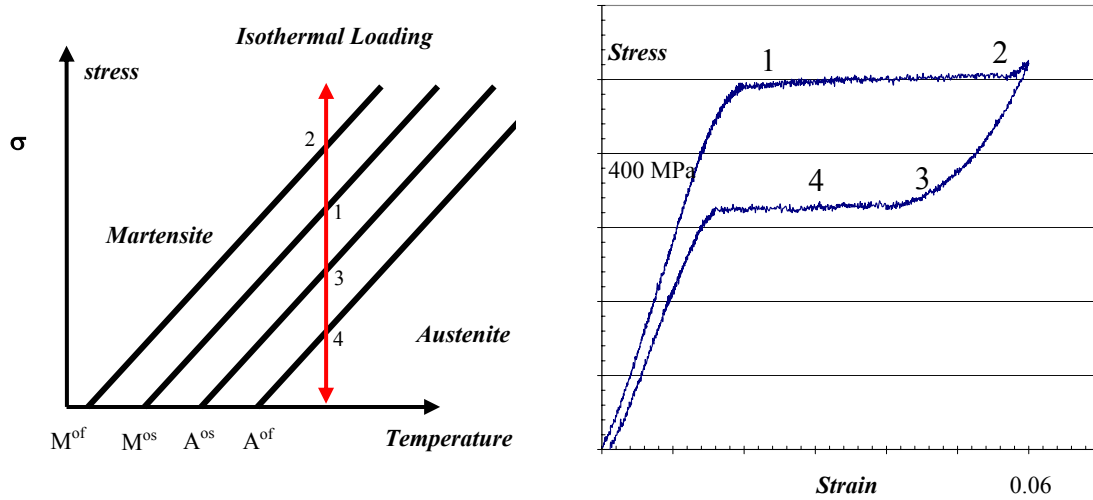
Figure 5. Pseudoelastic behavior of an SMA wire [8].

If the stress is applied above A^{of}, the full recovery of strain is obtained during the unloading as shown in Figure 5.

1.2. SMA actuators

Shape Memory Alloy actuators can provide an interesting alternative to conventional actuation methods such as hydraulic actuators and electric motors. SMA actuators can reduce the size, weight and complexity of a system and to facilitate maintenance, thus increasing the reliability of a system.

1.2.1. Advantages

The SMAs offer important advantages in actuation mechanisms, such as

1.2.1.1. Simplicity and compactness of the mechanism

The SMA actuator is regarded as a "Direct Drive Linear Actuator" [9] that utilizes the solid-to-solid phase transformation of the alloys, and does not require any reduction mechanism. The actuator can be reduced to a single SMA element, i.e. an electrically activated SMA wire or spring. The stroke and force can also be easily modified by the selection of the SMA element, such as SMA wire or SMA spring. Hence the use of SMA can result in a simplified, more compact and more reliable device.

1.2.1.2. Creation of clean and silent working conditions

Due to the absence of friction mechanisms (such as gear reduction systems) in SMA elements, the latter can work without generating dust particles and noise [9, 10]. In micro/miniature and medical applications, where a few small particles can damage the entire system, the SMA actuator can be useful. Only highly sensitive sensors can detect the acoustic noise and sound created by the martensitic transformation because the actuation of an SMA element is nearly noiseless [10]. SMA actuators can be operated under micro-g accelerations (low gravity conditions) compared to conventional actuators. These low gravity conditions along with clean working environment are suitable for space applications such as satellite release mechanisms [11].

1.2.1.3. High power/weight (or power/volume) ratio

SMA actuators can actuate under 300 MPa or higher stress conditions. For example, a 0.10 mm diameter NiTi wire can generate and actuation force of 2.356 N (0.24 kgf) at a

stress level of 300 MPa. If its length is 10 cm, its weight is 5.1 mg. Thus the actuator can

pull up a weight, which is 47,060 times of its own weight, with 3% of strain. Its power

density will be 1386 W/kg (1 Hz x 3 mm x 2.356 N/5.1 mg) or higher according to its

actuation frequency. SMA actuators can attain a high power density especially at low

levels of weight [9]. Thus SMAs are extremely attractive in micro-actuator technology

[9]. Additional advantages of Ni-Ti SMAs are the excellent corrosion resistance and

biocompatibility [10]. Figure 6 shows that SMAs have high energy densities even

compared to other smart materials.
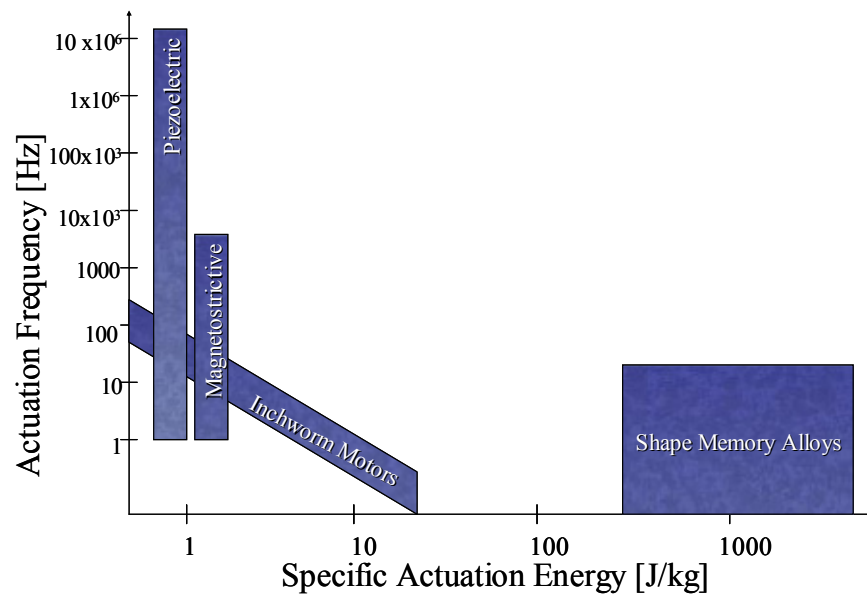
Figure 6. Energy densities and actuation frequencies of smart materials [12].

1.2.2. Disadvantages

Generally, SMA actuators have several disadvantages compared to other conventional actuators. These disadvantages should be considered in selecting and designing SMA actuators.

1.2.2.1. Low energy efficiency

An SMA actuator can be thought as heat engine where the SMA material converts thermal energy into mechanical energy. The theoretical thermal efficiency of every heat engine, including SMA actuators, cannot be above that of the Carnot Cycle. Thus the thermal efficiency of the SMA actuator is restricted to approximately, 10% because of its low working temperatures. However, in practice, the actual efficiency of SMA actuators is below 1% [9]. Gil and Planell [13] calculated the thermal efficiencies of the NiTiCu shape memory by means of calorimetric techniques and mechanical tests, found that thermal efficiencies ranged from 4.7% to 5.3 %.

1.2.2.2. Low actuation frequency

The phase change in a SMA element can be achieved by heat exchange between the SMA element and the surroundings, such as a heat source and a heat sink. Thus the heating and cooling rates determine the response speed of an SMA element. The heating rate can be increased limitlessly by the electrical resistive heating method, given a powerful enough power supply. Resistive heating can however also result in overheating of the SMA elements. But the cooling rate is limited by the heat transfer rate between the

SMA element and the external environment (heat sink). Figure 6 also shows general actuation frequencies of SMA materials along with comparisons.

1.2.2.3. Fatigue

The reliability of SMA actuators depends on global lifetime performance [10]. The material properties and operational ranges of stress and strain mainly influence the fatigue life of SMA. The tests [14] of an air cooled SMA wire (0.17 mm) with 1 Hz actuation frequency showed 150,000 cycle fatigue life before breaking under 150 MPa loading. Preventing overheating can increase the fatigue life of SMA element [9].

1.2.2.4. Control

The change that occurs within a SMA's crystalline structure during the SME is not a thermodynamically reversible process, and is a highly non-linear phenomenon. In other words there is energy dissipation due to internal friction and creation of structural defects [5]. This induces a temperature hysteresis, which makes it challenging to develop modeling and control schemes for a SMA actuator. When the SMA element is heated, its transformation is started at A^s and is finished at A^f, where the SMA element is 100% in the austenite state. When the SMA element is cooled to M^f, martensite begins to form and reaches 100% at M^f.
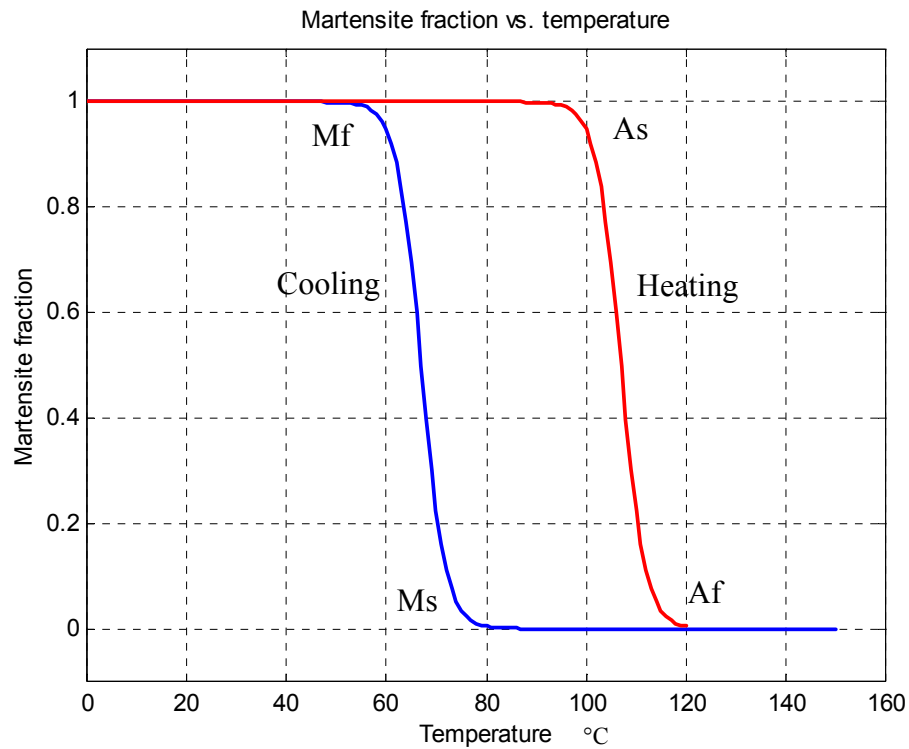
Figure 7. Hysteresis loop in shape memory alloy.

The hysteresis of SMA as shown in Figure 7 is mainly dependent on the composition of the alloy and the manufacturing processes. The entire deflection of an SMA element occurs over a small temperature range of around 40 °C, making it difficult to control accurately in partial transformation. Adding a few percent of copper to NiTi SMA can narrow the width of the hysteresis loop [5].

1.2.3. Actuation methods of SMA actuators

The SMA actuators may be heated up by: 1) passing an electrical current through them, which is called resistive heating (applicable to small diameter SMA wires or springs), 2)

passing an electrical current through a high resistance wire or tape wrapped around the SMA element (applicable for bulk SMA), 3) using thermoelectric Peltier elements, and 4) hot air/water convection or by exposure to thermal radiation [15]. The cooling of the SMA element is the key for the frequency response of SMA actuators since their response is mainly limited by the cooling rate. Experiments have been performed to compare the effect of different cooling techniques such as 1) Peltier elements, 2) natural convection cooling with heat sinks, 3) air forced convection cooling, 4) water immersion and 5) water forced convection cooling. The following explains two types of SMA actuators, which have been developed at the SMART lab of Texas A&M University.

1.2.3.1. Resistive heating and water forced convection cooling

SMA actuators can be actuated by Joule heating. Resistive heating depends heavily on electrical resistivity. Until recently, the heat transfer mechanism for most SMA actuators has been based on resistive heating (M$\rightarrow$A) and cooling with forced convection or natural convection (M$\rightarrow$A). The convection heat transfer is caused by energy transfer due to the bulk motion of the fluid and due to random molecular motion (diffusion). Figure 8 and Figure 9 show a resistive heating and convection cooling SMA actuator, which was used for an SMA actuated biommimetic hydrofoil [16]. The SMA actuator was composed of connectors, tubing and an SMA wire. In addition to physically terminating the SMA wire, the brass connector as shown in Figure 8, also acted as both an electrical terminal and cooling connection for the SMA wire. The SMA wire was embedded in a circular channel/tubing. Elastic silicon tubing was used to allow for the

change in SMA length during actuation. Cold water was used as the working fluid and was circulated by pump constantly and controlled by a flowmeter.

Forced convection cooling by fluid is one of the fastest cooling methods for an SMA element, and therefore many SMA actuators adopted the forced convection cooling method in order to overcome the problem of low actuation frequencies. Since cold water flows through the tube constantly regardless of the heating and cooling cycle, the power consumption or energy loss through the flow is significant. This is a rather inefficient heat exchange mechanism [15, 17, 18] and requires large amounts of electrical power and thus heavy, low-energy-density power supplies or batteries. The resistive rapid heating of an SMA element can easily result in over heating of the SMA element, even if sensitive control methods and sensors are utilized.
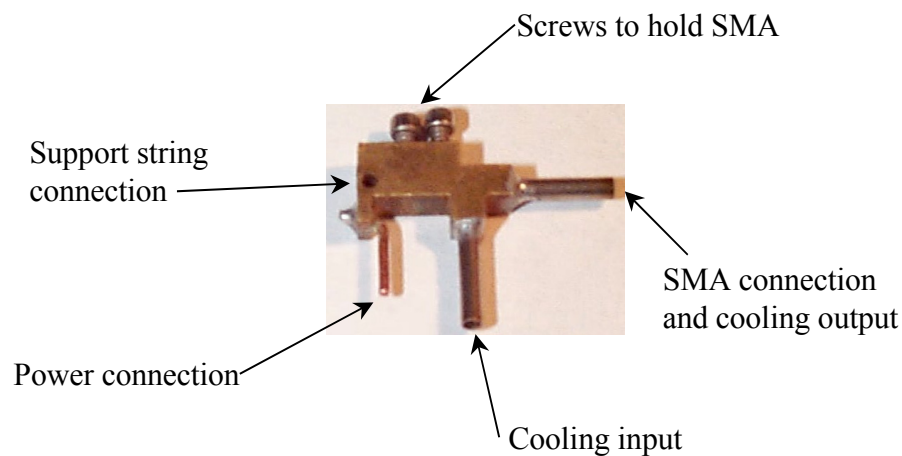
Figure 8. Brass connector for SMA actuator.
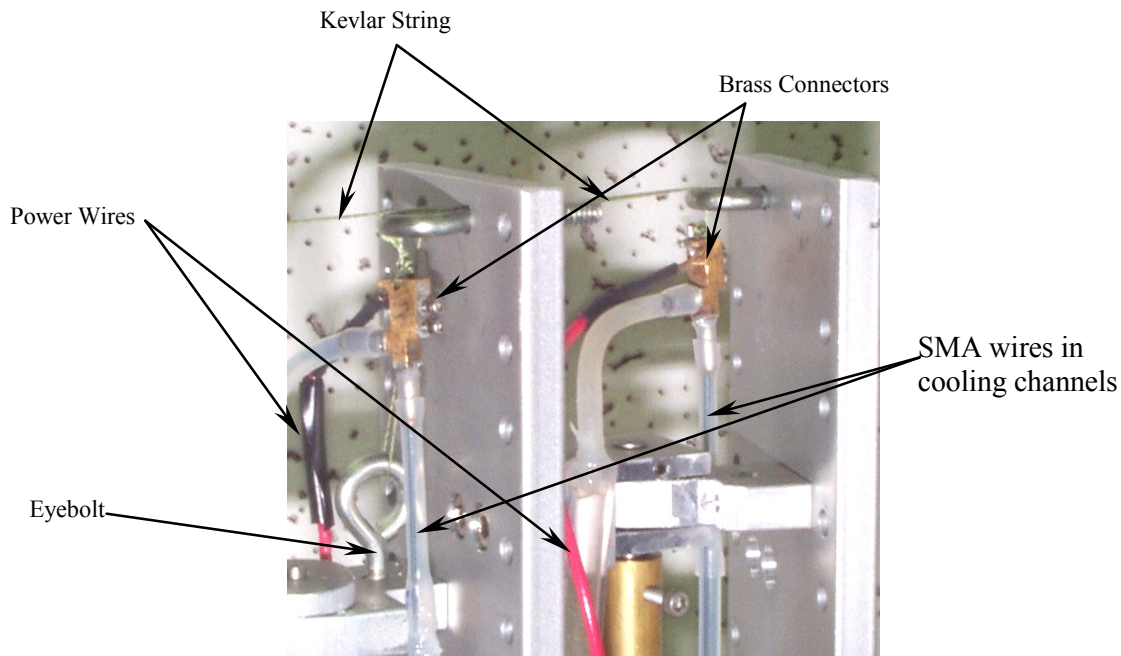
Figure 9. Resistive heating and forced convection cooling SMA actuators for hydrofoil

(circular channels + connectors + SMA wires).

1.2.3.2. Thermoelectric semiconductors (Peltier elements)

Semiconductors have been used for localized cooling, employing the thermoelectric Peltier effect. Depending on the direction of the current, the Peltier effect can be used as a heat sink (refrigeration) or as a heat source (heating) [18]. Figure 10 shows a schematic of a thermoelectric SMA actuator [18]. A thin SMA plate actuator is sandwiched between pairs of negatively doped (N) and positively doped (P) semiconductor elements. Two heat sinks are positioned as shown and the entire assembly is connected to a current source. Each pair of N and P is electrically connected in parallel. When the current is directed from the N to the P element, the Peltier effect causes a reduction in the temperature of the SMA plate. If the direction of the current is reversed, the SMA plate

will be heated. Thus the phase transformation can be induced by temperature change of the SMA plate.
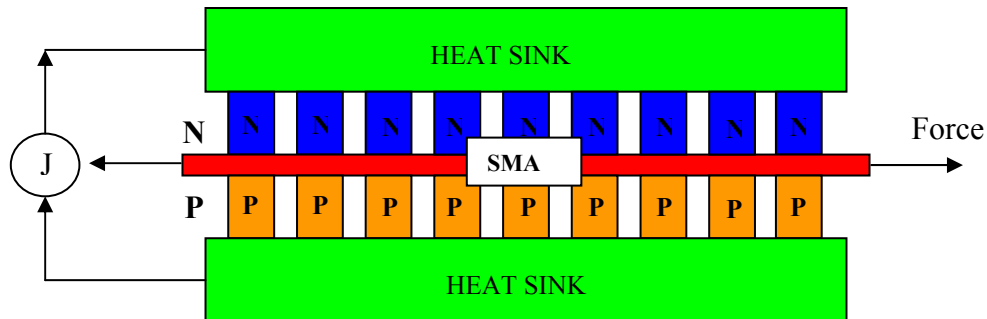
Figure 10. Schematic of thermoelectric SMA actuator [18].

The thermoelectric heat transfer mechanism has demonstrated relatively high actuation frequencies [18]. But a physical connection between the SMA element and the cooling device required to increase the heat transfer rate is very difficult to realize due to the elongation and contraction cycle of the SMA element. The temperature of the overall system may increase quickly during the actuation due to inappropriate/insufficient cooling. Also this kind of device also has a very low efficiency; hence the overall system efficiency is further lowered.

1.3. Research objectives

The SMA actuators have very high power density compared to conventional actuators as mentioned earlier. Since the SMA element, a heat engine [19, 20], is used to convert the thermal energy to mechanical energy, the phase change can be obtained by heat exchanges between a heat source and a heat sink. Thus the actuation frequency of the SMA actuator is only dependent on the rate of the heat transfer mechanisms. Until recently, the heat transfer mechanisms for most SMA actuator have been based on resistive heating and forced convection cooling or natural convection cooling. But unfortunately, this kind of heat transfer mechanism requires large amounts of electrical power. Hence SMA actuators lose their compactness and energy density if the energy sources, such as power supplies and batteries, are considered as one of the parts of the SMA actuators. The thermoelectric heat transfer mechanism, by utilizing semiconductors that employ the Peltier effect, has demonstrated relatively high actuation frequencies, but it suffers from low energy efficiency itself. In other words this kind of actuation method can increase the actuation frequency at the expense of the energy efficiency of the system, or at the expense of the power density/energy density of the system.

Using the high energy of fuels as the main energy source for an SMA actuator can overcome this low energy density of previous SMA actuator systems. Fuels, such as propane, have tremendous energy densities (around 50.4 MJ/kg), which are much higher than those of batteries as shown in Figure 11.
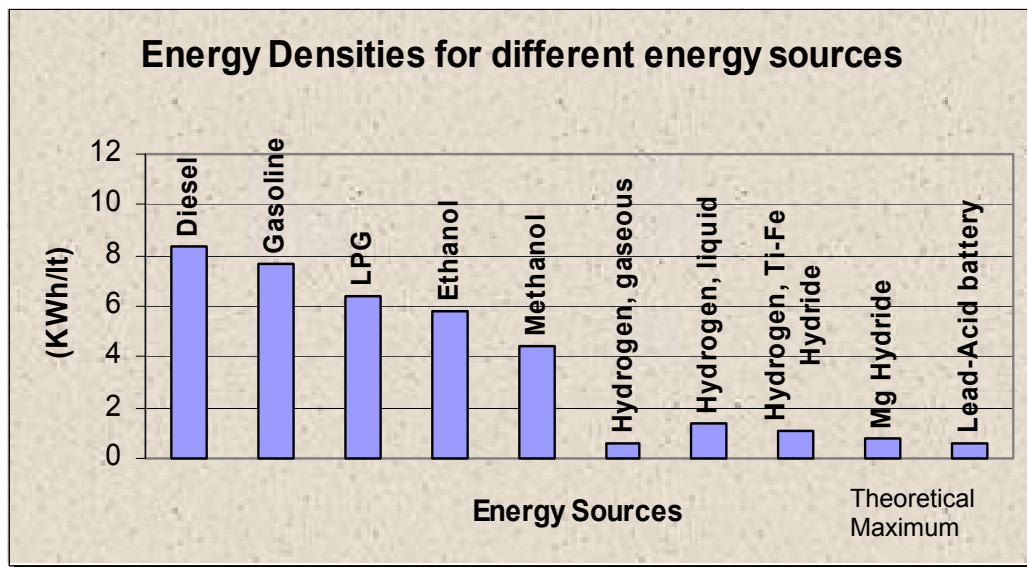
Figure 11. Energy densities for different energy sources [21].

The high energy density benefit of fuels could be materialized if an SMA actuator utilizes the chemical energy of fuels, transferred to a convection fluid, which can cause the phase transformation of an SMA element by forced convection heat transfer. In other words the SMA element can be heated and cooled by using forced convection heat transfer mechanisms. If the velocity and temperature of the fluid are high, the SMA element can be easily and quickly heated. The transformation temperatures of the SMA element are low temperatures compared to conventional internal engines, thus temperature of the working fluid does not need to be very high. Also this kind of actuation mechanism can prevent over heating of the SMA element regardless of sensitive control methods and sensors due to its low operating temperatures.

Thus, the forced convection heating and cooling can be utilized by using fuel energy in order to actuate the SMA actuator. This can overcome the low energy density of resistive heating systems and the low efficiency of the thermoelectric heat transfer mechanism, even though it should need additional devices such as pumps and valves. Also, the high energy of fuel is transferred easily to the fluid through a combustor and a heat exchanger. Researchers have worked on developing highly efficient, compact combustors and heat exchangers, using micro technology [22, 23]. The high energy density of fuels and SMA elements, along with the incorporation of the actuation control hardware and software inside the unit, can result in a highly compact actuator system that can be run wirelessly by low-power, digital, actuator control signals. The high-energy density, high recovery stress and strain of the SMA along with the high energy density of fuel will result in high actuator compactness, force and stroke, respectively. Convection heating and cooling of the SMA, can result in considerable actuation frequencies. In addition, for systems with sufficient parasitic heat, the actuator can utilize the parasitic heat as its energy source, resulting in a relatively high-efficiency actuating system. This actuator design merges the advantages of SMAs and fuels, i.e., the high actuation forces, the large power densities and the silent actuation characteristics of SMAs and the tremendous energy densities of fuels.

The main objective of this research is to design, fabricate and test a highly compact shape memory alloy based actuator that utilizes forced convection heat transfer mechanism by using the high energy density of fuels, such as propane, as the main energy source.

CHAPTER II

DESIGN CONCEPT

2. Design concept and efficiencies of the SMA actuator systems

This chapter presents the principle of the fuel-powered compact SMA actuator system,

comparisons with other actuator systems based on different main energy sources, in

terms of energy and power density, and thermal & Carnot efficiency.

2.1. Energy density and power density

The following data describes the concept design parameters of the SMA element of

actuator systems of Figure 12. This data can be modified accordingly to meet different

requirements for the actuator. A NiTi SMA strip with a rectangular cross section

measuring 12 mm x 1 mm (12 mm^2 cross sectional area) was selected as the SMA

element to increase heat transfer rate compared to a wire having the same cross section

area. Four such strips can be installed in a rectangular channel with 12 mm x 16 mm

cross section. Previous efforts, [24, 25, 26], during the last several years have lead to

precise actuation control techniques for NiTi SMAs at stress levels of 200 MPa and

actuation strains of 3 %. These numbers are used here in this design. In order for the

SMA strip to produce bi-directional loads it will have to be pre-stressed. This could be

achieved via a stress-biasing spring. If, for example, a stress bias level of 100 MPa is

chosen, the SMA strip will be able to produce bi-directional actuation loads at the level

of ±(100 MPa) x (strip cross sectional area), or, ±1,200 N (or 2,400 N uni-directional).

An arrangement of four such strips in an array will yield a combined bi-directional

actuation force of ±4,800 N. For a SMA strip length of 254 mm, the SMA actuation

stroke (at 3 % strain) is 7.62 mm (0.76 cm).
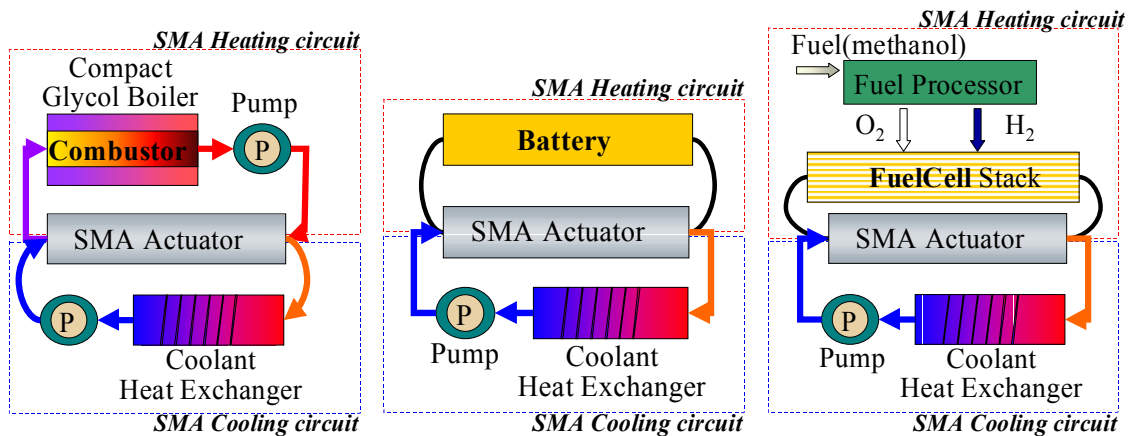
Figure 12. Different, SMA-based, compact actuator systems with fuel+combustor,

battery and fuelcell as the energy source.

The first system in Figure 12, referred to as the SMA-Combustor system,

comprises of two pumps, a combustor, the SMA element, the cooling circuit heat

exchanger and fuel as the energy source. The SMA strips are embedded in a channel.

Heating and cooling fluid medium alternatively circulates through the channel to achieve

the M-to-A and A-to-M transformations, respectively. The heating medium (Ethylene

Glycol or water) is heated through the burning of the fuel in the combustor. The cooling

medium, after it removes the heat from the SMAs goes through a heat exchanger where

it disposes of the energy obtained from the SMA strips. The two pumps that circulate the

two media are equipped with valves that are properly timed through the heating and cooling cycles.

Alternative energy sources like batteries and fuel cells have been considered as energy sources for the SMA actuator in the other two systems of Figure 12. The results of the comparison have been tabulated in Table 1and Table 2 for different cases of actuation cycle numbers (1000, 10000, 100000 actuation cycles). Table 3 shows the energy efficiencies of three systems.

These tables show that the SMA-Combustor compact actuator has high energy and power densities compared to battery and fuel cell powered systems. The fuel cell stack itself has high energy and power densities, but needs additional equipment such as a reformer or a hydrogen tank, a cleanup unit, a compressor and cooling devices [27, 28], especially for a large number of actuation cycles. The main disadvantage of the fuel cell system is the large mass of the fuel processing unit or the mass of the fuel tank. All these factors combined give a low energy/power density for the SMA-Fuel Cell actuator system. In the case of a battery powered SMA (SMA-Battery) actuator system, the mass of the battery increases significantly with the increase in number of actuation cycles, although it has the highest efficiency. This, coupled with the fact that batteries have low energy densities compared to fuel cells or fuels [21, 29], yields the lowest overall energy/power densities for this system.

Table 1. Output energy density (total mechanical work/mass of system).

Actuator Systems	1,000 Cycles	10,000 Cycles	100,000 Cycles
SMA-Combustor	9.887(Wh/kg)	71.04(Wh/kg)	193.6(Wh/kg)
SMA-Battery	3.717(Wh/kg)	4.411(Wh/kg)	4.495(Wh/kg)
SMA-Fuel Cell	0.7605(Wh/kg)	7.038(Wh/kg)	41.1(Wh/kg)

Table 2. Output power density (total mechanical work/(mass of system × cycles)).

Actuator Systems	1,000 Cycles	10,000 Cycles	100,000 Cycles
SMA-Combustor	35.59(W/kg)	25.57(W/kg)	6.971(W/kg)
SMA-Battery	13.38(W/kg)	1.588(W/kg)	0.1618(W/kg)
SMA-Fuel Cell	2.738(W/kg)	2.534(W/kg)	1.48(W/kg)

Table 3. Efficiency of the system.

Actuator Systems	1,000 Cycles	10,000 Cycles	100,000 Cycles
SMA-Combustor	2.253(%)	2.318(%)	2.325(%)
SMA-Battery	2.999(%)	3.003(%)	3.003(%)
SMA-Fuel Cell	2.499(%)	2.502(%)	2.503(%)

2.2. Efficiency

In the design and development of SMA actuators, the available thermal efficiency and its limits must be calculated and considered. Lagoudas and Bhattcharyya [30] evaluated the efficiency of the thermoelectric SMA actuators. Jardine [31] and Gil [13] proposed calorimetric techniques and mechanical tests to evaluate the efficiency of shape memory alloys based on an ideal shape memory effect (SME) heat engine cycle [32].

2.2.1. Transformation temperatures of an SMA strip (DSC test)

The phase transformation temperatures and latent heat were first determined in order to calculate the thermal efficiency of SMA strip (12 mm x 0.9 mm). The strip utilized in this study was provided by Memory Corporation and is a 10 %-Copper NiTi alloy (K alloy). A Perkin-Elmer Pyris 1 Differential Scanning Calorimeter (DSC) was used to determine the phase transformation temperatures and heat of transformation. Latent heat, ΔH, is measured as the total area under the curve during the heating and cooling cycle. The cooling cycle was started after holding for 1.0 minute at 120 °C. The SMA was then cooled from 120 °C to –60 °C at 5 °C/min. The heating cycle began after holding the SMA for 1.0 minute at –60 °C. The SMA was then heated from –60 °C to 120 °C. Figure 13 shows the DSC test results of the SMA strip.
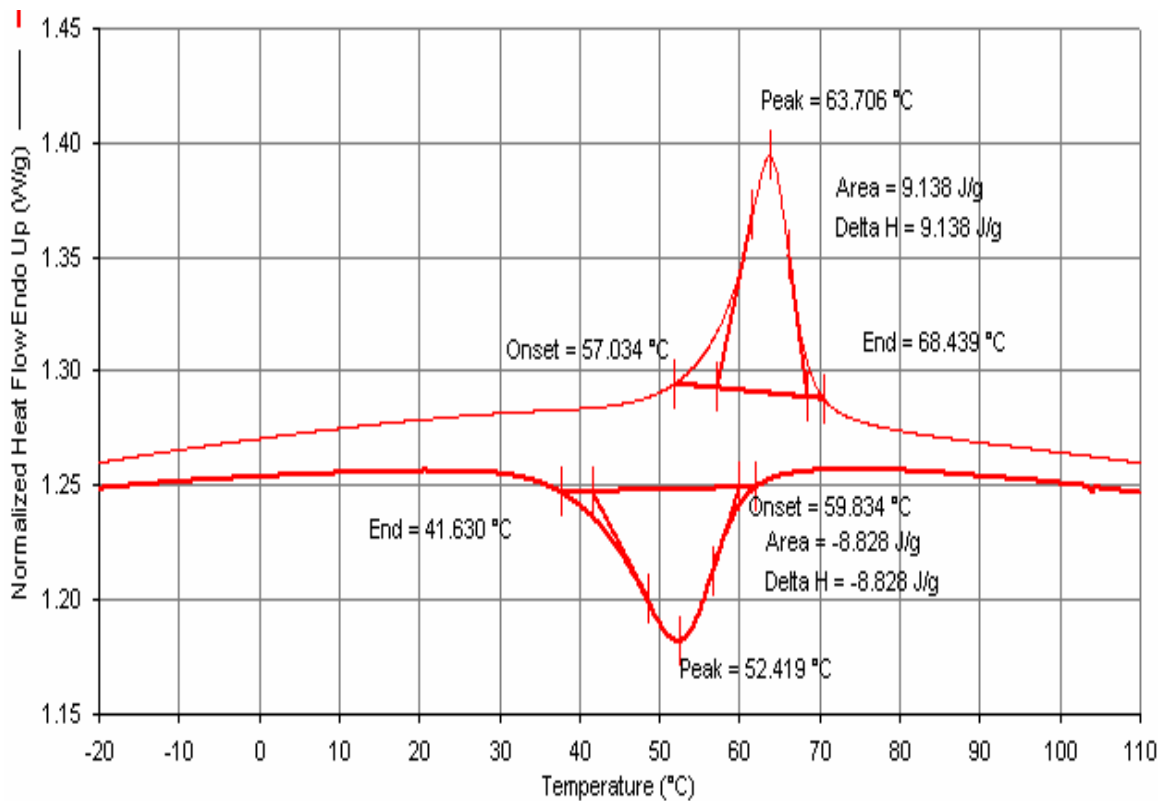
Figure 13. Transformation temperatures and latent heats for an SMA strip (DSC test).

2.2.2 Carnot efficiency

The proportion of the Carnot efficiency that can be usefully realized in practical engines is typically around 60 %. Once the design of an engine has been optimized, the only way to get higher performance is by increasing the Carnot efficiency or by extension of the difference in the temperatures of the source and sink of heat between which the engine operates. The Carnot efficiency of an SMA heat engine is [30, 33]

$$\eta_{Car} = \frac{A^f(\sigma_{max}) - M^f(\sigma \to 0)}{A^f(\sigma_{max})}$$

(1)

$$A^f(\sigma) = A^{of} + \sigma \frac{dA^f}{d\sigma} \tag{2}$$

Where $\dfrac{dA^f}{d\sigma}$ is the slope in the stress-temperature diagram of the SMA strip. Hence,

$$\eta_{Car} = 1 - \frac{M^f(\sigma \to 0)}{A^{of} + \sigma_{max} \dfrac{dA^f(\sigma)}{d\sigma}} \tag{3}$$

Theoretically, $M^f(\sigma \to 0)$ at zero stress and M^{of} should be the same value [13]. Hence the Carnot efficiency is like that,

$$\eta_{Car} = 1 - \frac{M^{of}}{A^{of} + \sigma_{max} \dfrac{dA^f(\sigma)}{d\sigma}} = 15.3\% \tag{4}$$

As seen in the last equation, by substituting in it the values of the transformation temperatures obtained from the DSC test, $dA^f/d\sigma = 1/6.7$ °K/MPa [34] and a stress level of 200 MPa stress, the Carnot efficiency is 15.3 %. The energy efficiency is theoretically restricted by the Carnot efficiency since an SMA actuator is a heat engine operating at low temperature.

2.2.3. Thermal efficiency of ideal SMA heat engine

The thermal efficiencies of SMA (SME) heat engines, which are of interest, have been estimated from thermodynamic magnitudes (enthalpies) and the transformation temperatures of the alloys [31]. The thermal efficiency for the ideal shape memory heat engine cycle is given [13, 31] as

$$\eta_{th} = \frac{\Delta H \times \Delta To}{To \times (C_p \times \Delta To + \Delta H(\sigma))} \tag{5}$$

Where C_p is the specific heat of the material and $\Delta To = To(\sigma) - To$. Also ΔH (latent heat) in the denominator of the efficiency equation is a function of stress,

$$\Delta H(\sigma) = \Delta H \times To(\sigma)/To \tag{6}$$

To is estimated as $To = 1/2 \times (M^{os} + A^{os}), or, 1/2 \times (M^{of} + A^{of})$

To calculate $To(\sigma)$, we take

$$To(\sigma) = 1/2 \times \left[M^s(\sigma) + A^s(\sigma) \right]$$

$$= 1/2 \times \left[M^{os} + (dM^s/d\sigma) \times \sigma + A^{os} + (dA^s/d\sigma) \times \sigma \right]$$

$$= To + (dM^s/d\sigma) \times \sigma \tag{7}$$

The thermal efficiency can be obtain by utilizing DSC test data and $d\sigma/dT = 6.7$ MPa [34] of the K-alloy. $d\sigma/dT = d\sigma/dM^s = d\sigma/dA^s$ is assumed to get *To*. Also the value of σ is assumed to be 200 MPa. Hence the thermal efficiency for the ideal shape memory heat engine cycle can be obtained from equation (5) as,

$$\eta_{th} = \frac{\Delta H \times \Delta To}{To \times (C_p \times \Delta To + \Delta H(\sigma))} = 3.12\% \tag{8}$$

where the value of C_p is 550 J/kg °K [13].

Gil and Planell [13] calculated the thermal efficiency of the NiTiCu shape memory alloys by means of calorimetric techniques and mechanical tests. Thermal efficiencies ranged from 4.7 % to 5.3 %. Generally, the efficiency of SMA alloys is low compared to

conventional heat engines. But the use of Shape Memory Alloys as actuators can reduce the size, weight and complexity of a system. Its power density is remarkably high, such as 100 W/kg or more [9]. Conventional actuators produce a significant amount of noise, while SMA actuation is silent. Thus, SMA actuators can be ideal for such cases as robotic, micro/miniature and medical applications, where power density, simplicity of mechanism and silent actuation are more important than energy efficiency of the system as explained in Chapter I.

The thermal efficiencies of three systems are shown in Table 3. These values are very reasonable considering the 3.12 % of the ideal heat engine efficiency. The battery system efficiencies show higher values than those of other systems due to its high efficiency in converting electrical energy to thermal energy and fewer additional power requirements. In implementation of these systems, the efficiency should be lower than the values of Table 3 due to additional energy losses and additional power requirements. From the comparison with other actuator systems based on the main energy source, SMA combustor system has the highest energy and power density.

CHAPTER III

THE FIRST-GENERATION FUEL-POWERED SMA ACTUATOR SYSTEM

3. The first-generation SMA actuator system

3.1. Design of the first-generation fuel-powered compact SMA actuator system

From the comparison with other actuator systems as explained in Chapter II, the fuel–powered SMA actuator system, having the highest energy and power density, was selected in order to develop the compact SMA actuator system. To measure available force, displacement and actuation frequency, a fuel-powered SMA actuator system was designed. The actuator system is composed of a pump, valves, a combustor, an SMA element, a hot fluid tank, bellows and heat exchangers. The bellows are used to prevent mixing between hot and cold fluid in the actuator system.

Figure 14 shows the first design of the fuel-powered SMA actuator system and the corresponding experimental setup. The load is applied constantly by dead weight for the entire heating and cooling cycle. The SMA strip was put through multiple thermal cycles by cycling its temperature from the martensite finish temperature ($T<M^f$) to the austenite finish temperature ($T>A^f$) under a constant applied stress of 71 MPa and 150 MPa.

(a)

1. SMA Actuator
2. Amplification device
3. Heater
4. Heat exchanger
5. Bellows(cylinder)
6. Pump

(b)
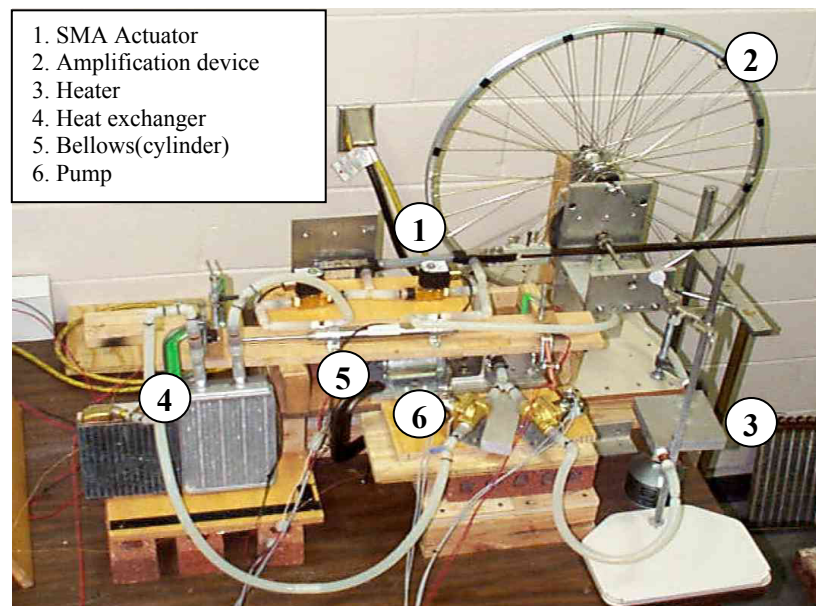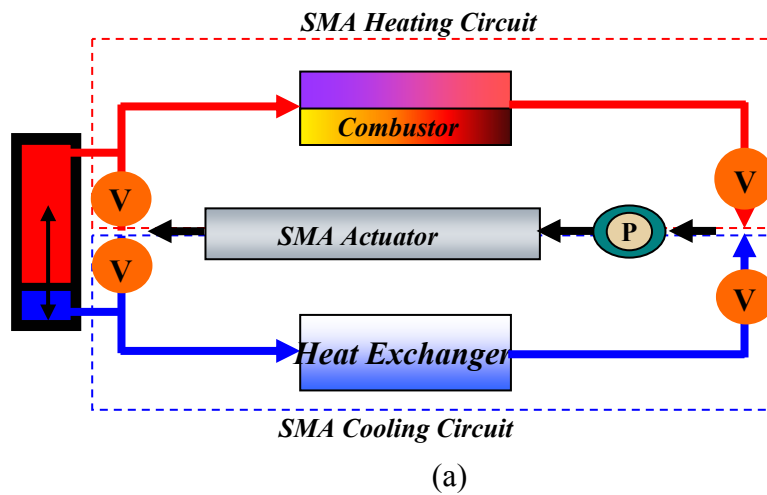
Figure 14. The first design of the fuel-powered SMA actuator system: schematic of

basic architecture (a) and its corresponding experimental setup (b).

Figure 15 shows loading paths during the heating and cooling cycles. At the higher

actuation frequency and under the higher stress condition, the strip can be in partial

transformation due to the reduction of heating duration and the increase of transformation temperatures. The strain and displacement were measured with a LVDT.
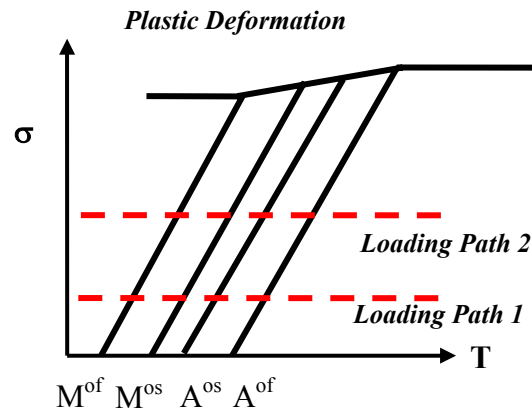
Figure 15. Heating and cooling cycle under constant applied stress.

3.2. Components of the SMA actuator system

3.2.1. SMA actuator

The SMA strip was embedded in a circular silicone tube, which can withstand high temperature and can bend and expand. The inside diameter of the tube is 12.7 mm and the wall thickness is 0.8 mm. Figure 16 shows the SMA actuator. Two steel connectors were utilized to hold the strip, as well as provide supply and return connections for the fluid flow and to transfer the actuation force to the mechanical stroke amplification device, which is shown in Figure 17. The amplification mechanism increases the stroke by 86 times and reduces the force by 82 times. The difference between the force attenuation and stroke magnification factors is due to the friction in the gears. Figure 18 shows the characteristics of the stroke amplification device.
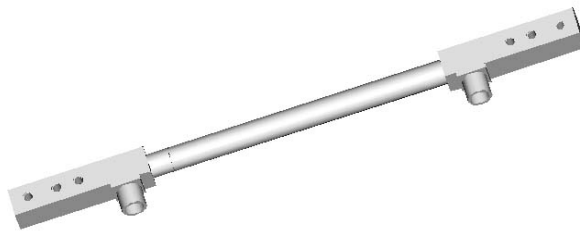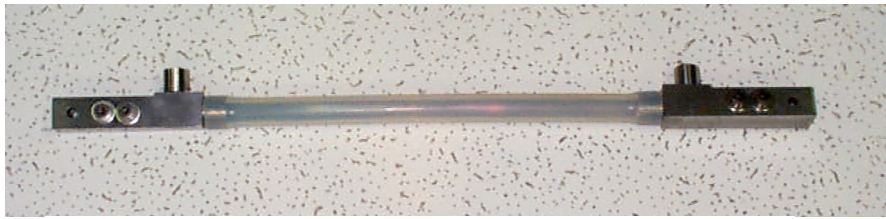
Figure 16. SMA actuator with a circular silicone channel and connectors.
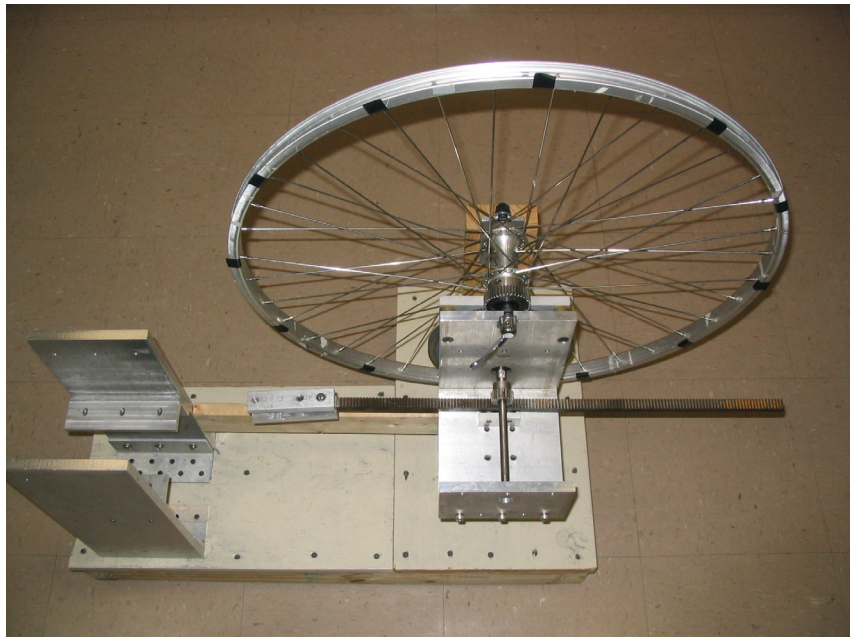
Figure 17. Stroke amplification device.
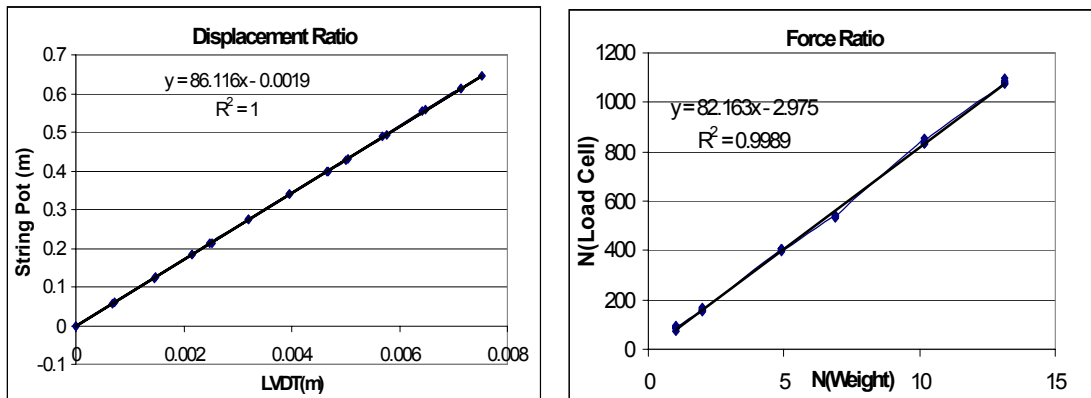
Figure 18. Performance characteristics of the stroke amplification mechanism.

The SMA strip is of the K-alloy type, which is a Ni, Ti and Cu alloy and has a 12 mm x 0.9 mm cross section area and is 254 mm long including connections. Thus, the available length of the actuator is about 210 mm. Out of all the Shape Memory Alloys that have been discovered so far, Nickel-Titanium has proven to be the most flexible and useful in engineering applications. Ni-Ti Shape Memory Alloys have greater ductility, more recoverable motion, excellent corrosion resistance and stable transformation temperatures [5]. Copper can decrease hysteresis and lower the deformation stress (detwinning stress) of the martensite. The strip was annealed at 450 °C for 20 minutes. Figure 19 shows the SMA strip with the annealing frame. The transformation temperatures of the strip were obtained by DSC tests after annealing. This type of SMA alloy has around 70 °C active A^f temperature and shows high-energy efficiency compared to other types of SMA alloys [18]. For the first-generation actuator, one strip was utilized as the SMA element of the actuator.
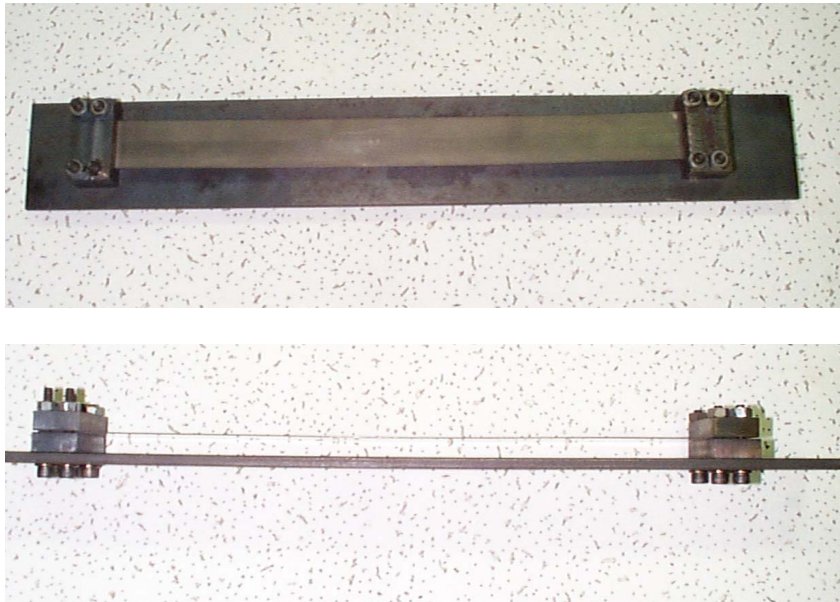
Figure 19. SMA strip with annealing frame.

3.2.2. Combustor and hot fluid tank

A 185 g compact commercial propane burner was utilized as the combustor. Its flame is adjustable up to 4000 Watts and runs on a valved butane and propane mix cartridge, which contains 227 g of fuel. It can boil 1 liter of water within 3 minutes. A 127 mm x 127 mm x 25.4 mm hot fluid tank was fabricated from an aluminum block and has a 635 mm flow path inside of it. This aluminum block was sealed by screws and RTV (high temperature silicone) and was heated directly by the camping stove. A K-type thermocouple was installed inside the aluminum block to measure the temperature of the hot fluid. The efficiency of this propane burner was estimated at around 40 %. Figure 20 shows the combustor (propane burner) and hot fluid tank used for the first-generation SMA actuator system.
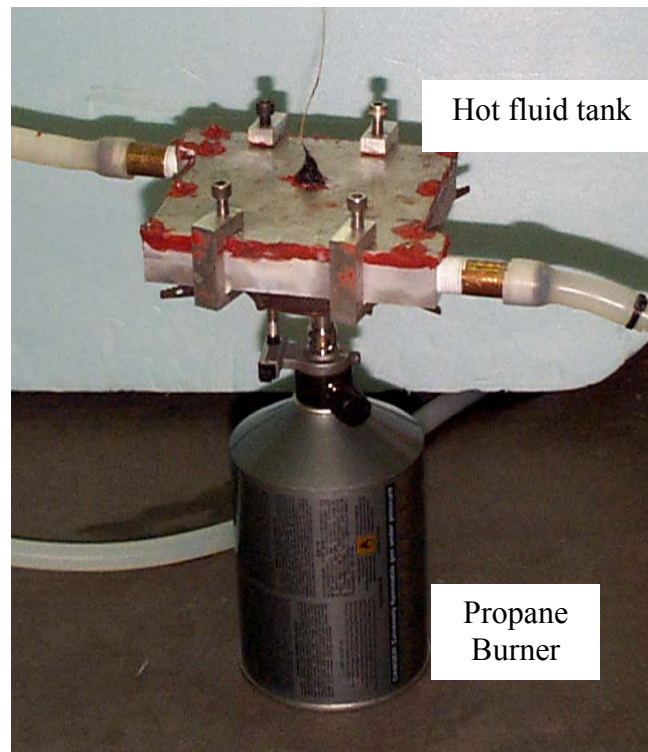
Figure 20. Combustor (propane burner) and hot fluid tank.

3.2.3. Heat exchanger

The cooling medium, after it removes the heat from the SMA strip goes through a heat exchanger where it disposes of that heat. For the first actuator system, two kinds of radiators, with a 59.2 ml/sec fan (125.5 CFM), were used. One is an automobile heater core and the other is a PC cooling radiator, which measures 152 mm x 178 mm x 5.1mm.

3.2.4. Pumps

The brass Omega FPUGR201 gear pump circulates heating and cooling media. Its maximum flow rate is 7.95 l/min at low pressure and can withstand 0.69 MPa and 149

°C. This pump circulates hot fluid and cold fluid alternatively. A one-pump system was selected to increase the energy density of the system. However, it suffers from some energy loss since hot and cold fluid heat and cool the gear pump itself. The pump was run by a DC motor. The pump runs constantly regardless of heating and cooling cycles. The solenoid valves control the heating and cooling medium circulated by the pump.

3.2.5. Solenoid valves

Four solenoid valves were utilized to control the heat and cooling circuits. The valves located before the pump in Figure 14 were GC direct-operated-diaphragm 2 way solenoid valves. They can be operated in pressure ranges from 0 Pa to 0.69 MPa, up to 145 °C of fluid temperature and have a Cv of 3.3. The other two valves were Parker 0.83 Cv direct acting valves. The Cv represents the actual amount of water in GPM (Gallon Per Minute), which passes through the valve with 1 psi pressure drop across the valve. The operating pressure and temperature ranges are from 0 Pa to 0.138 MPa and up to 85 °C, respectively. The GC valves are operated by on/off signal coming from a controller, while the other two valves are controlled by bellows and switches.

3.2.6. Bellows

Mixing between hot and cold media must be avoided to reduce energy losses. A bellows was utilized to prevent mixing between hot and cold fluid caused by sharing common flow paths such as the actuator channel and the volume inside the pump. Also, it can generate some amount of force to aid in the fluid media circulation. A 152 mm stroke,

double-acting double-rods American air cylinder, as shown in Figure 21 was used as a bellows. For the first-generation actuator system, the bellows and switches controlled two solenoid valves, which are located downstream of the SMA actuator (Figure 14). An SR latch switch algorithm was utilized.

Figure 21. Double-rod double-acting cylinder and switch.

3.2.7. Control and data acquisition

The data acquisition board used was a National Instrument AT-MIO-16XE-50. The board has 16-bit resolution and eight differential inputs. Two digital channels were used for the switches, three differential channels for thermocouples and the LVDT. A HP6268B DC power supply provided the power to the system. A power splitter board was controlled through a National Instrument PCI-6704 D/A board. The power splitter board takes the single input from the HP 6268B power supply and splits it into six

individually controlled channels, which are used to supply controlled power to the motor and the solenoid valves. A Lab-Windows program was put together to control the hardware and acquire data.

3.3. Experimental results and discussion

Water was selected as the heating and cooling medium, based on numerical results because it was easy to handle and the boiling temperature of water is high enough to heat and cool the SMA strip under high stress (150 MPa). The inlet velocity and inlet temperature were also determined based on numerical analysis. The volume flow rate of the hot water and the cold water was set as 0.11 l/sec by adjusting the power of the pump, thus the flow velocity inside the SMA channel was around 1 m/sec. The actuator system was tested under a constant load of 735 N (71 MPa). Figure 22 shows the displacement of the strip under 735 N of load for the closed-loop system. The hot water, after heating the SMA strip, returned back to the heater, which added enough energy to the water to compensate for its energy loss due to the heating of the SMA strip and other energy dissipations. The cold water, after cooling the SMA strip, returned back to the radiator where the thermal energy removed from SMA strip was dissipated to the surroundings by forced air convection.

A 2.4 % strain (5 mm stroke) and 0.1 Hz (heating time: 5 sec, cooling time: 5 sec) actuation frequency was obtained from the closed-loop test. This result shows lower strain and slower frequency compared to the open-loop system, in which the hot and the cold water were not re-circulated in the system. Figure 23 and Figure 24 show the results

for the open-loop system. The SMA actuator system can generate enough recovery stressand strain at 0.5 Hz actuation frequency. Figure 23 shows higher frequency under 735N than Figure 24 under 1560 N. The maximum operating pressure of the close-loop system is about 69 K Pa in the heating (hot fluid) circuit due to pressure losses in the system and the generation of water vapor.
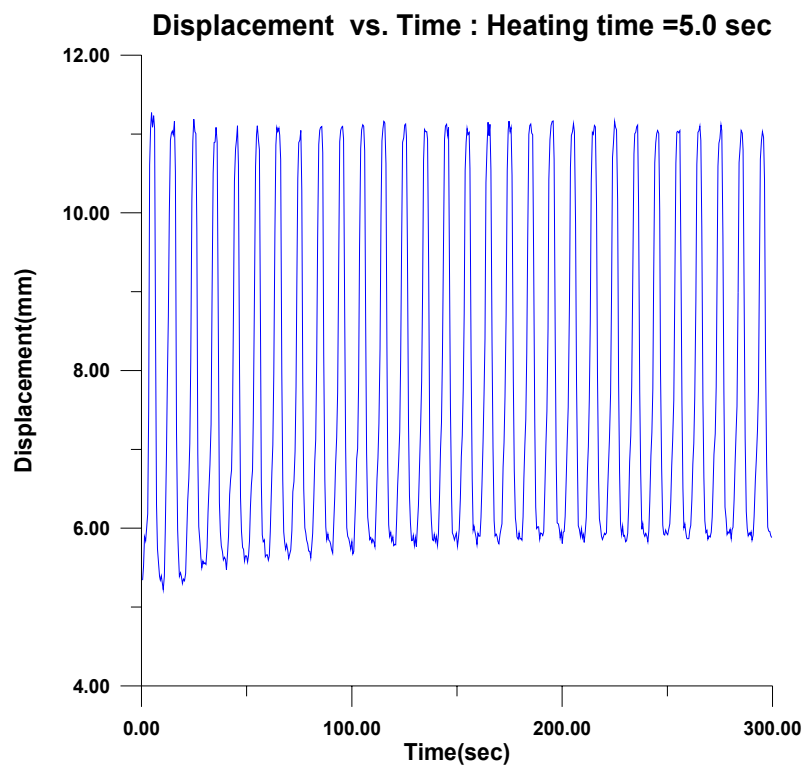
Figure 22. Displacement vs. time under 735 N (71 M Pa) for the closed-loop system.
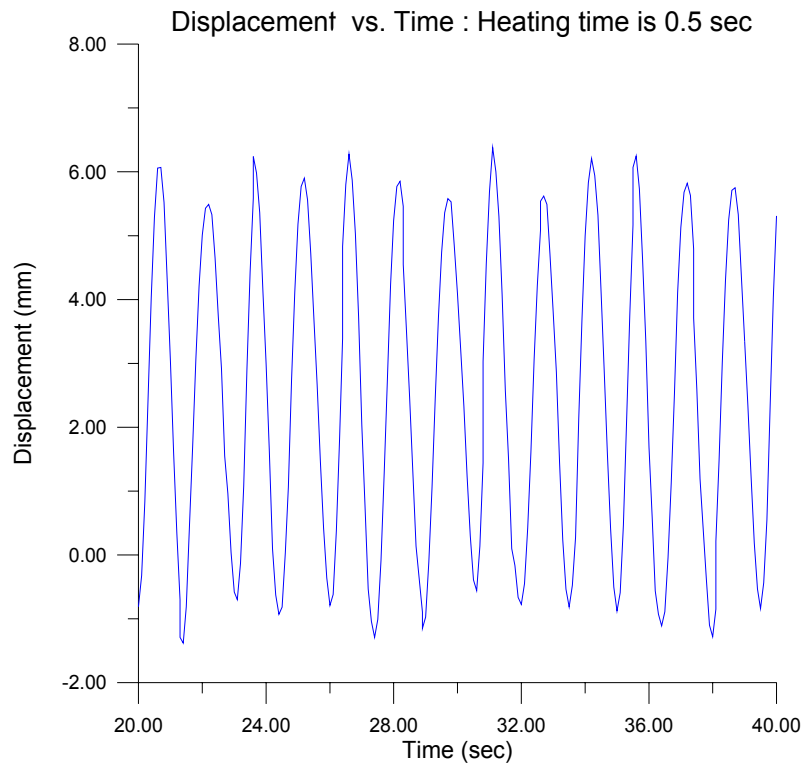
Figure 23. Displacement vs. time under 735 N (71 MPa) for the open-loop system.

In the open-loop test, the actuation frequency of the SMA actuator (K-alloy, 12 mm x 0.9 mm) can be raised to 1 Hz (heating and cooling cycle) under 71 MPa of load (735 N), and up to 0.5 Hz under 150 MPa of load (1560 N).

The lower strain and slower actuation frequency in the closed-loop system was mainly due to the mixing between hot and cold fluid in the system. As the number of cycles increases, the energy loss caused by the mixing increases. The cylinder and pump are also heat loss devices because they contain heating and cooling medium, alternatively.
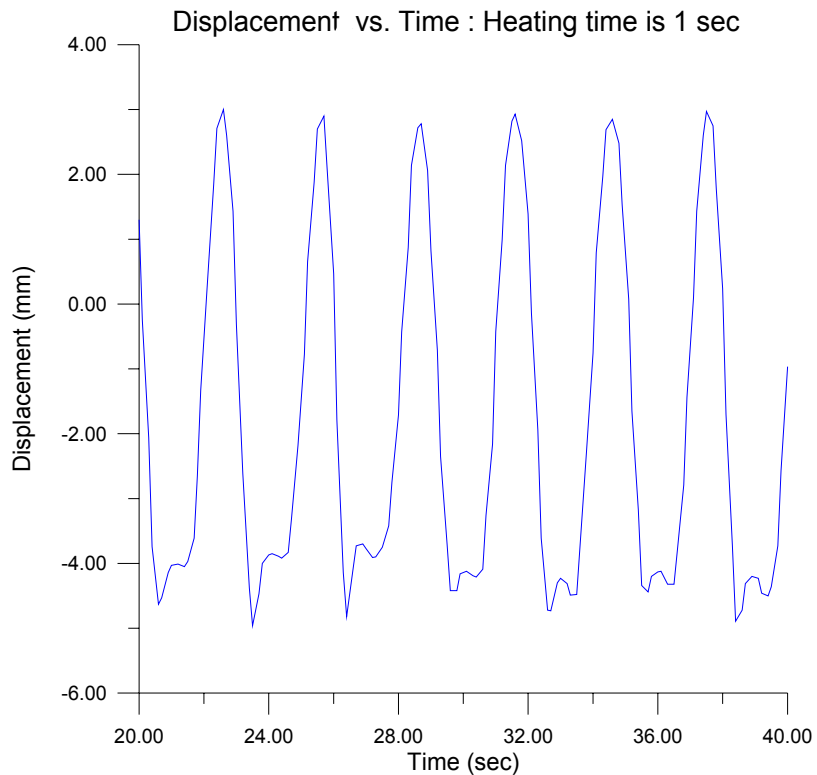
Figure 24. Displacement vs. time under 1560 N (150 MPa) for the open-loop system.

Hence, the hot fluid temperature decrease and the cold fluid temperature increases. This degrades the performance of the heating and cooling circuits. A more powerful heater and heat exchanger can overcome this mixing, but in that case the system might lose compactness and energy density. One of the methods to prevent mixing is to adjust the stroke length of the cylinder (bellows), thus making the channel volume and the volume of other sharing passages equal to the volume of the bellows. If the mixing and energy loss were prevented properly, at least 0.5 Hz actuation frequency and 3.3 % recovery strain could be obtained. As mentioned above, the 0.5 Hz actuation frequency

under 150 MPa stress with 3.3 % strain was obtained from the open loop experimental test.

3.4. Conclusions

The first-generation fuel-powered compact SMA actuator system is relatively simple and compact compared to other actuator systems. The forced convection heating and cooling can generate relatively high actuation frequency compared to resistive heating and air forced convection cooling. The electric power consumption for the pumps, valves and fan of the actuator system, which was around 70 Watts, was much smaller than that required for resistive heating and forced convection cooling of a SMA actuator like the one used to actuate a biomimetic hydrofoil [16], which used several hundreds watts. The first SMA actuator system could actuate the SMA strip (12 mm x 0.9 mm x 210 mm) at 0.5 Hz under 150 MPa stress with 3.3 % strain (displacement: 7 mm) for the open-loop test, while 2.4 % strain (displacement: 5mm) and 0.1 Hz (heating time: 5 sec, cooling time: 5 sec) actuation frequency was obtained for the closed-loop test. The main reason of this low actuation frequency of the closed-loop system was the mixing between the hot and cold water in the system.

CHAPTER IV

NUMERICAL ANALYSIS OF THE SMA ACTUATOR

4. Numerical heat transfer analysis

4.1. Numerical heat transfer analysis of SMA actuator

To determine optimal channel geometry and to estimate the period of the heating and cooling cycles (i.e., actuation frequency), a numerical heat transfer analysis of the SMA actuator was carried out with commercial software packages. The energy balance equation of the SMA strip can be expressed as:

$$\rho_s C_{ps}^* \frac{\partial}{\partial t}[T_s] = \nabla \bullet (k_s \nabla T_s) + q_{gen} \qquad (9)$$

Where T is the temperature, k is the thermal conductivity, ρ is the density, C_p^* is the specific heat of the SMA strip and t is the time. The subscript s indicates the "SMA strip". Here q_{gen} represents the energy generation rate per volume. In the phase transformation of an SMA, heat is absorbed during the reverse transformation (martensite to austenite) and it is released during the forward transformation (austenite to martensite). This heat is called the latent heat of transformation (ΔH). The area under the curve described by the specific heat is the latent heat of transformation. During phase transformation, the heating and the cooling of the SMA are slowed down due to the latent heat of the transformation. When performing a transient heat transfer analysis it is therefore important to account for this effect. An empirical relation describing the dependence of the specific heat on temperature is given in [18]. Certain transformation temperatures (such as A^f =363.83 °K=90.68 °C and A^s = 352.42 °K=79.27 °C), latent

heat and specific heat capacity at a stress level of 150 MPa stress were utilized in the followings equations.

For the forward transformation:

$$C_{ps}^{*} = C_{ps}^{o} + \Delta H \frac{\ln(100)}{\left|M^{s} - M^{f}\right|} e^{-\frac{2\ln(100)}{\left|M^{s} - M^{f}\right|}\left|T - \frac{M^{s} + M^{f}}{2}\right|} \tag{10}$$

$$M^{f} < T < M^{s}$$

For the reverse transformation:

$$C_{ps}^{*} = C_{ps}^{o} + \Delta H \frac{\ln(100)}{\left|A^{s} - A^{f}\right|} e^{-\frac{2\ln(100)}{\left|A^{s} - A^{f}\right|}\left|T - \frac{A^{s} + A^{f}}{2}\right|} \tag{11}$$

$$A^{f} < T < A^{s}$$

The original specific at value of the SMA (C_{ps}^{o}) is 550 J/Kg °K [13].

The curves obtained for the variation of the specific heat of the SMA with temperature, during the forward and reverse transformations at 150 MPa stress, are shown on Figure 25.

For this numerical heat transfer analysis, the FLUENT 5.5/6.0 and GAMBIT 1.3.0 software packages were utilized. Figure 25 shows a maximum increase of the value of the specific heat (C_{ps}^{o}) of about 8 times the original value. It was difficult to get FLUENT to run with the specific heat varying with temperature such as in Figure 25. Instead, a piecewise variation has been adopted. The approximations used are shown on Figure 25. The area under these approximations is kept the same as the original, thus preserving the value of the latent heat of transformation. However by preserving the same maximum value of specific heat during transformation, the transformation's start

and finish temperatures had to be changed. The transformation starts later and finishes earlier.

Variation of Cp with temperature
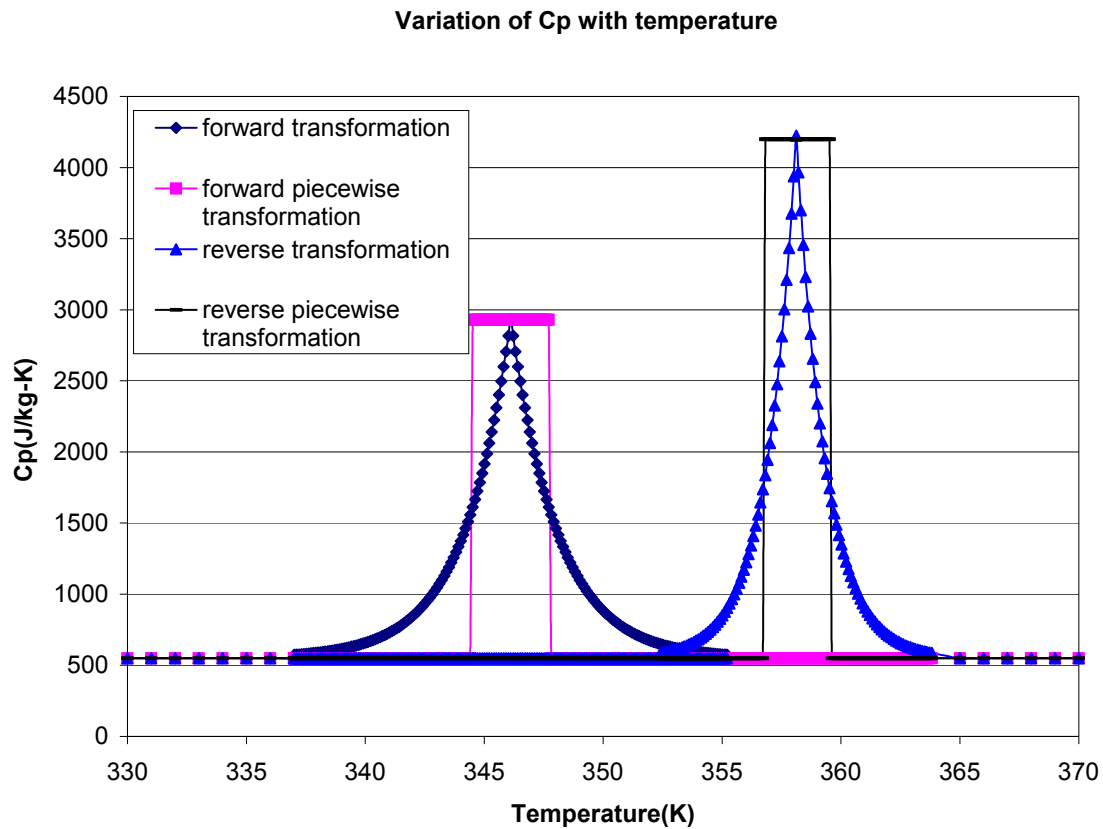
Figure 25. Variation of C_p with temperature.

The phase transformation temperatures and latent heat were first needed in order to calculate the heat transfer rate of the SMA strip. The strip is a 10%-Copper NiTi alloy. A Perkin-Elmer Pyris 1 Differential Scanning Calorimeter (DSC) was used to determine the phase transformation temperatures and latent heat. Figure 26 shows the transformation temperature and latent heats of the SMA strip. The transformation

temperatures, A^f=363.83 °K (90.68 °C) and A^s=353.42 °K (79.27 °C) at 150 MPa, were utilized in the following analysis. In the phase transformation of an SMA strip, heat is absorbed during the M→A transformation and released during the A→M transformation. This heat is called the latent heat of transformation. An empirical relation describing the dependence of the specific heat with temperature was given by equations (10) and (11), but a piecewise variation [35] was adopted instead of the empirical relation due to the difficulty of its implementation in FLUENT.
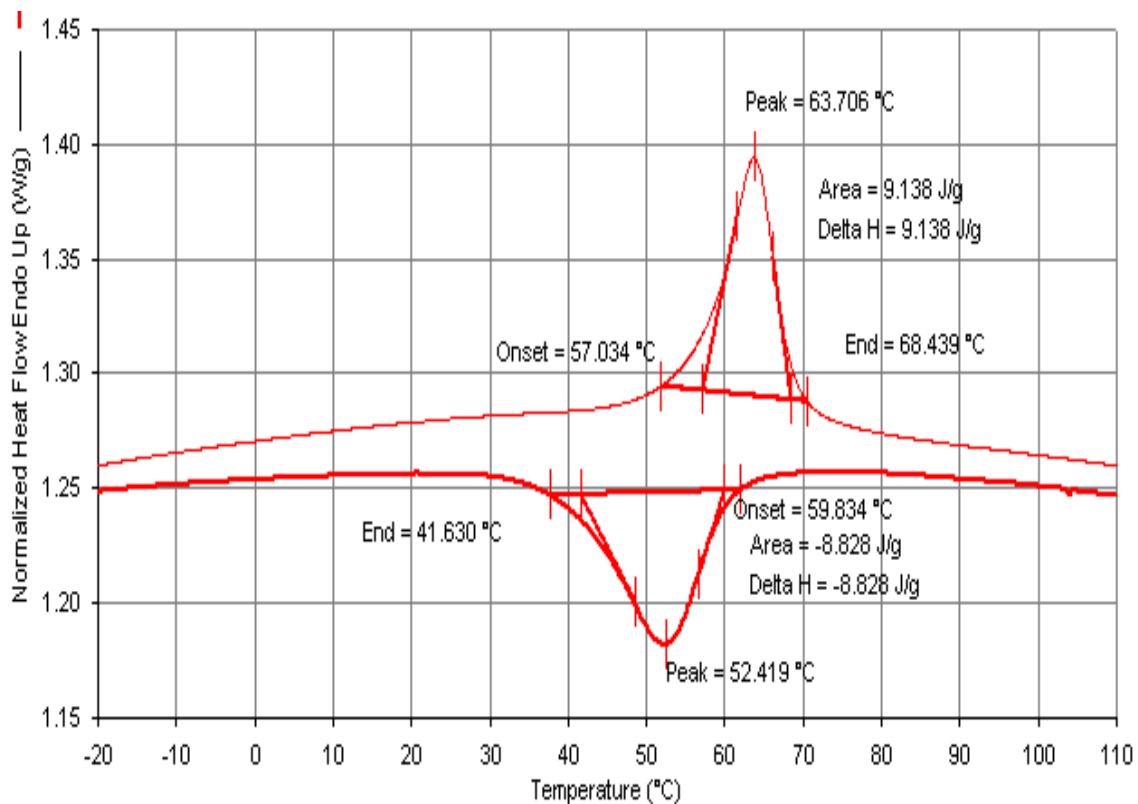
Figure 26. Transformation temperatures and latent heats for K-alloy strip (DSC test).

For the numerical calculation, the initial temperature of the SMA strip was 335 °K (61.85 °C) and the inlet velocity and temperature were 1 m/sec and 370 °K (96.85 °C), respectively. The working fluid was hot water. Energy losses through both ends of the channel and channel walls were ignored. A channel and an SMA strip embedded in it were the computational domain. The temperature distribution along the SMA strip, for three different channels, such as a circular channel (R= 5.84 mm, L=250 mm) and two rectangular channels (3.81 mm x 8.9 mm x 250 mm and 1.9 mm x 8.9 mmx 250 mm) was calculated.
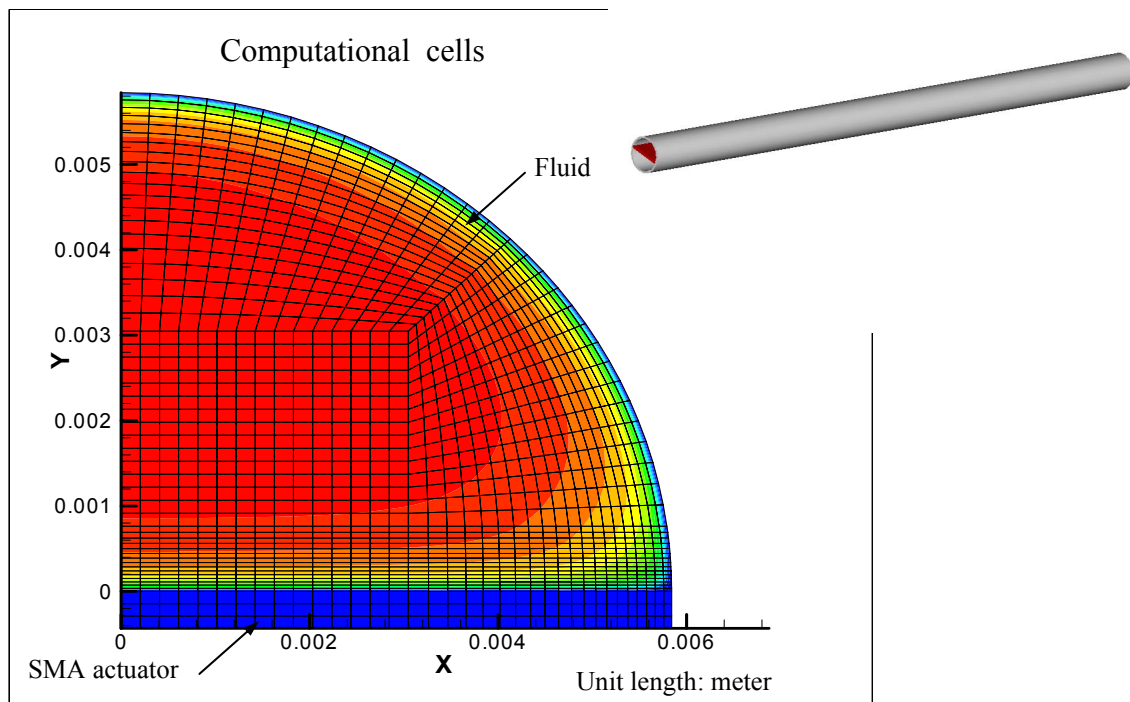
Figure 27. Computational domain of circular channel with SMA actuator.

The flow was in a turbulent state (circular channel: $Re_d=22400$, rectangular channel-I: $Re_d=20700$ and rectangular channel-II: $Re_d=10600$), thus the standard κ-ε model, in combination with a two-layer zonal method for the near-wall region was used. A quarter of the channel and the SMA strip were considered by using symmetric conditions. Figure 27 through Figure 32 show cross sections of the computational domains and velocity distributions for the three channels. The grid was generated by GAMBIT and was denser near the SMA strip and the wall in order to capture the boundary layer.
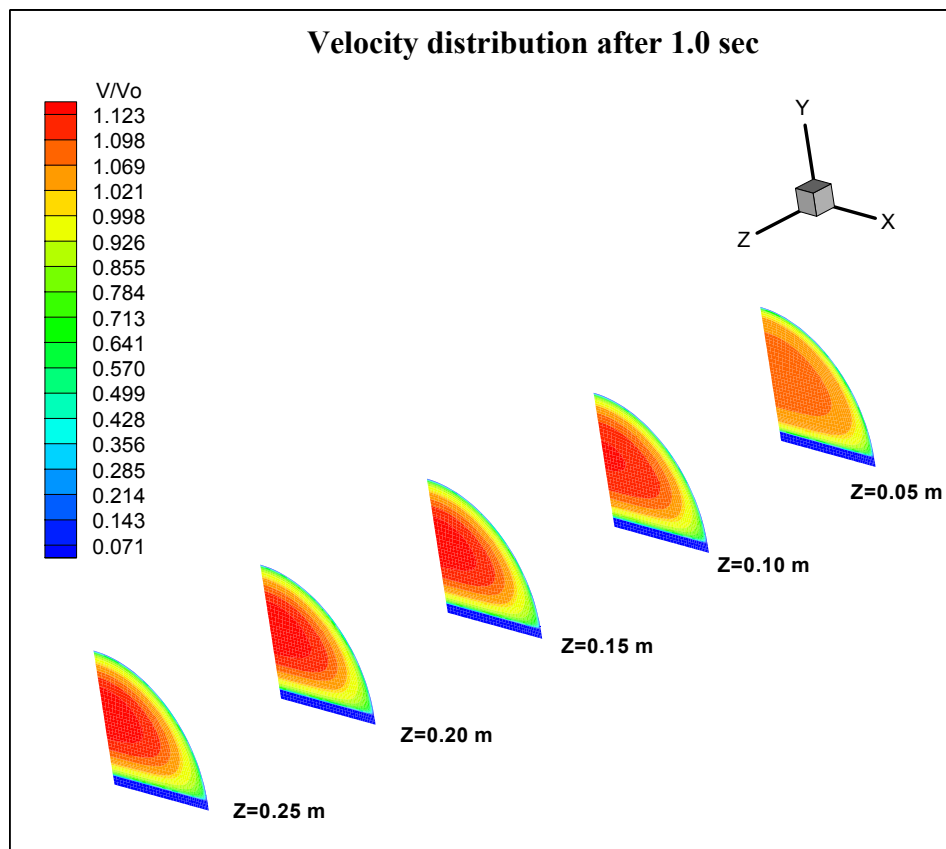
Figure 28. Velocity distribution-circular channel.
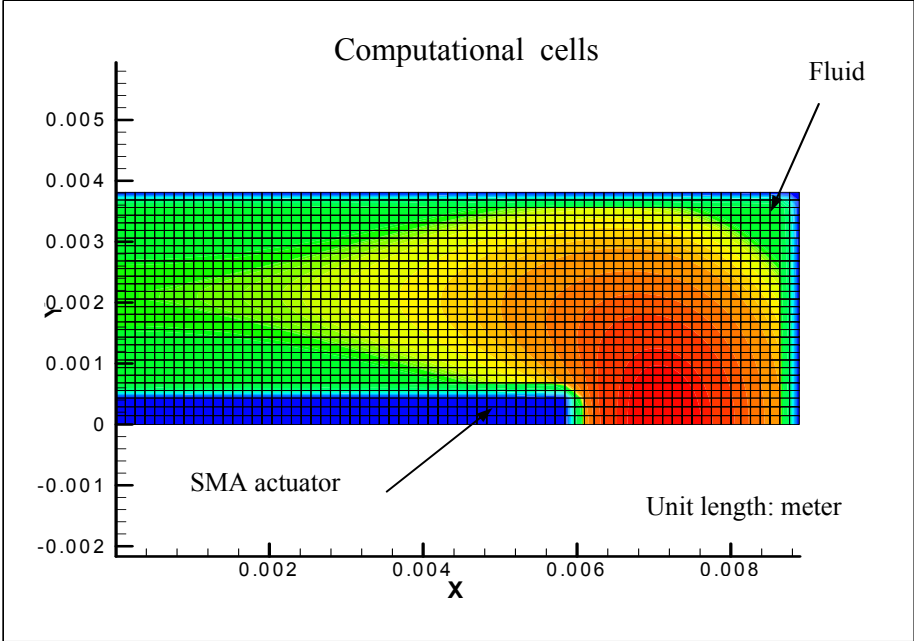
Figure 29. Computational domain-rectangular channel-I
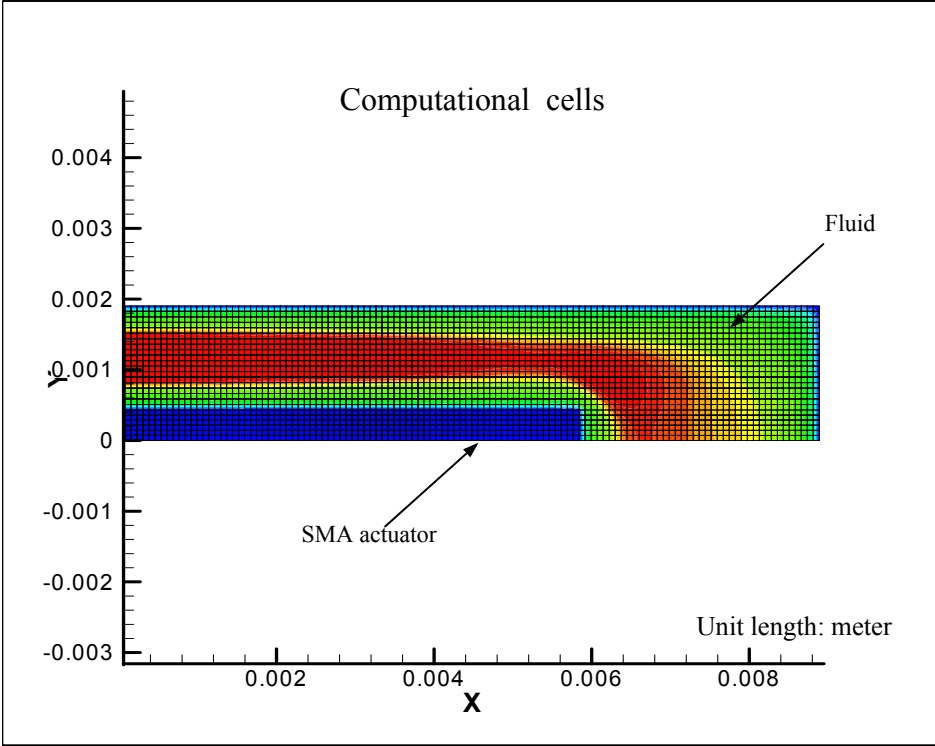
Figure 30. Computational domain-rectangular channel-II
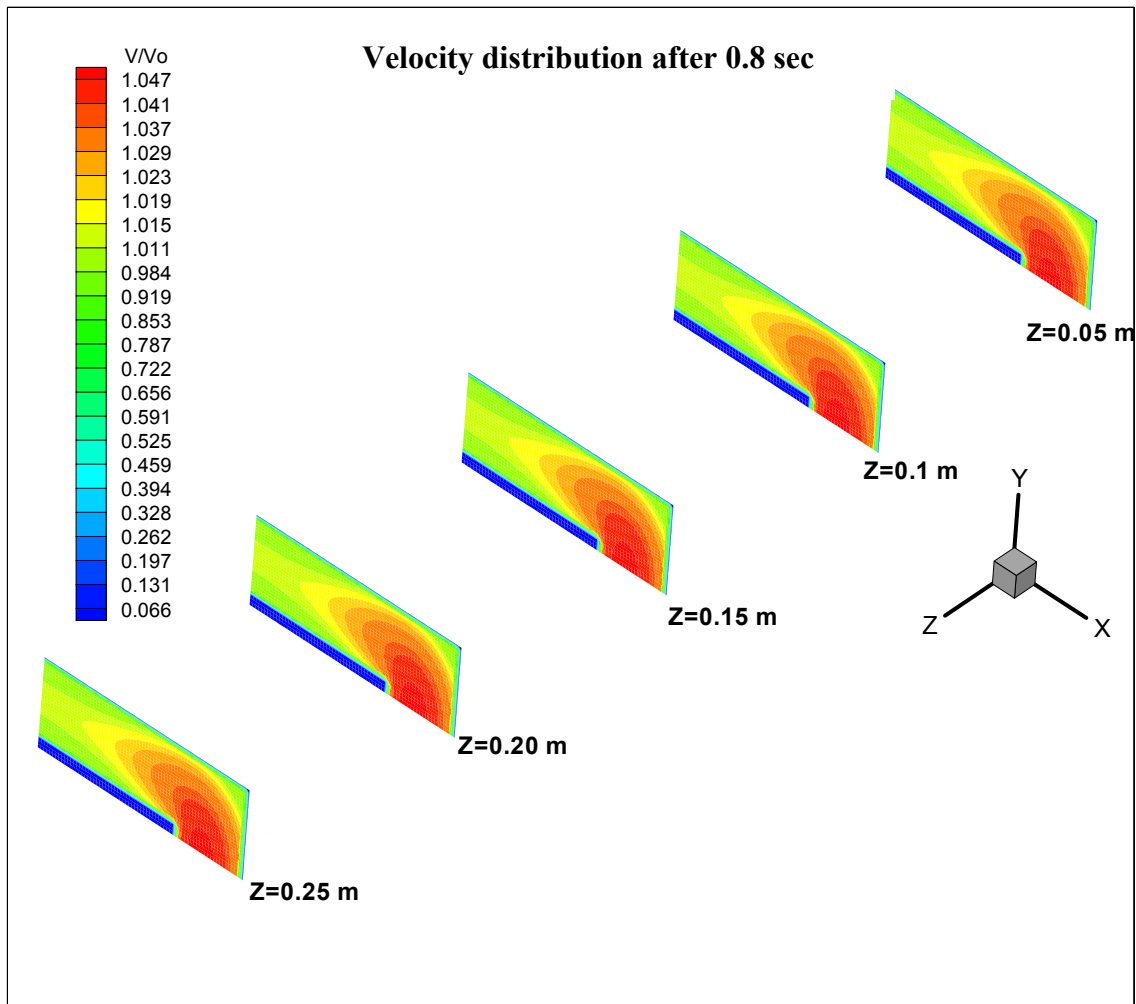
Figure 31. Velocity distribution-rectangular channel-I.
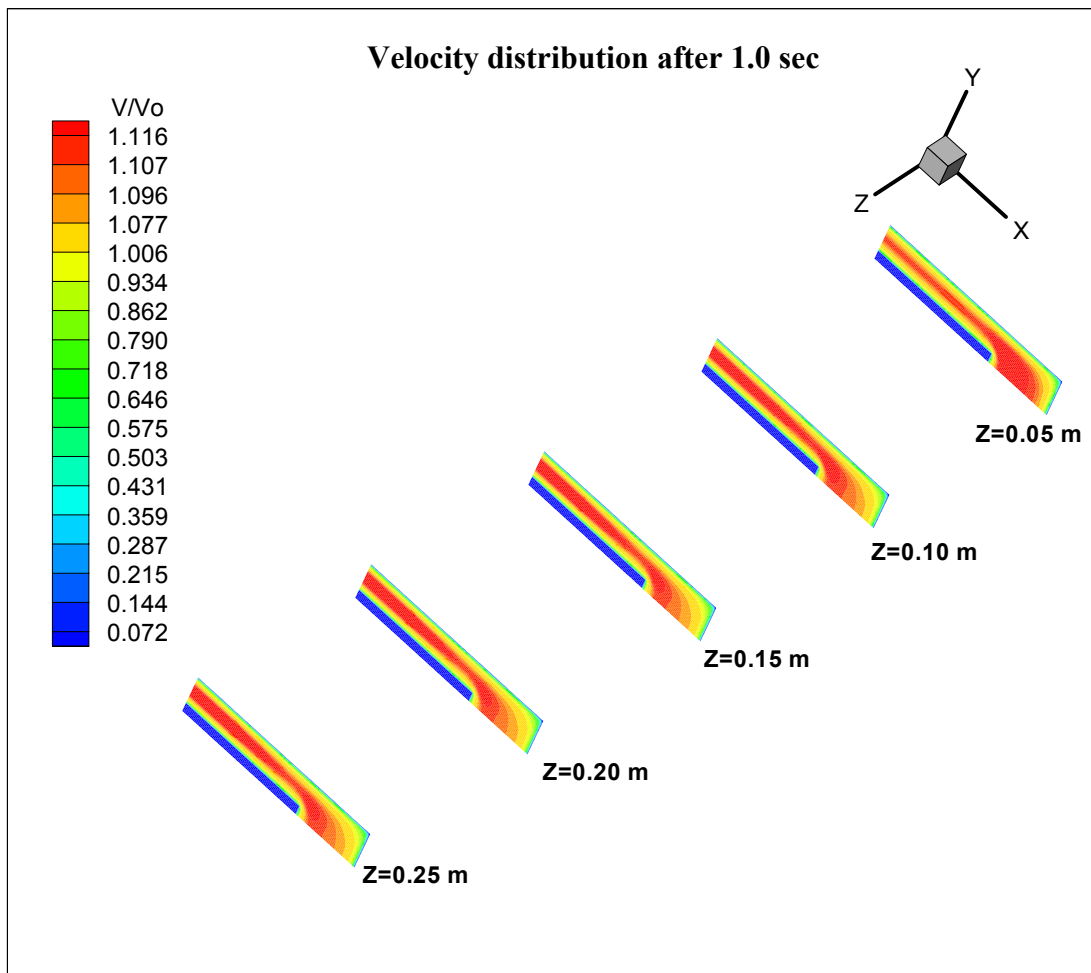
Figure 32. Velocity distribution-rectangular channel –II.

4.2. Results of numerical analysis

The experimental results for the first-generation SMA actuator system in high-stress conditions showed that the heating period was around 1.0 sec. The results of Chapter III showed good agreements with the results of the numerical analysis. The heat transfer calculation was an unsteady heat transfer problem. The latent heat of the SMA strip was

assumed to be a piecewise function, thus the austenite finish temperature was changed from 363.83 °K (90.68 °C) to 360 °K (86.85 °C) as explained above. If the temperature in the middle cross-section of the SMA strip (where the temperature is lowest) is above 360 °K (86.85 °C), the strip will be in the fully-transformed austenite state. The time step was set as 0.01 sec for unsteady calculation and the maximum iteration number at each time step was set as 40. Figure 33 through Figure 35 show temperature distributions of the middle cross-section of the SMA strip along the z direction. The flow rate of the circular channel was equal to that of the rectangular channel-I, but 2 times greater than that of the rectangular channel-II.

The heating period for the circular channel was 1.0 sec, for the rectangular channel-I was 0.8 sec and for the rectangular channel-II was 1.0 sec. The cooling was faster than heating [35], thus we can estimate available maximum actuation frequency as around 0.5 Hz under 150 MPa stress condition, for all three cases. The temperature profiles along the SMA strip in the circular channel case are completely different from those in the rectangular channel cases. Figure 33 through Figure 35 show that the maximum temperature of the strip is located at x = 0.0 m along the length (z direction) in the circular channel case compared to x = 0.006 m in the rectangular channel cases. This is mainly due to the channel geometry, which generates different velocity profiles. For the circular channel case, the high velocity region is located around x = 0.0 m and y = 0.003 m. For the rectangular channel cases, the high velocity region is located around x = 0.007 m and y = 0.0 m.

The results for the rectangular channel-II show the advantage of its geometry, especially in terms of the heat transfer rate, compared to the circular channel. Though the flow rate was half of that of the circular channel, the heat transfer rate for the rectangular channel–II had the same value as that for the circular channel or higher. Thus, using the rectangular channel-II, the size of the pumps and valves can be reduced and the energy density and power density of the system can be increased. Based on the results of the numerical analysis, we selected the rectangular channel for the second-generation actuator system over the circular channel used in the first-generation actuator system.
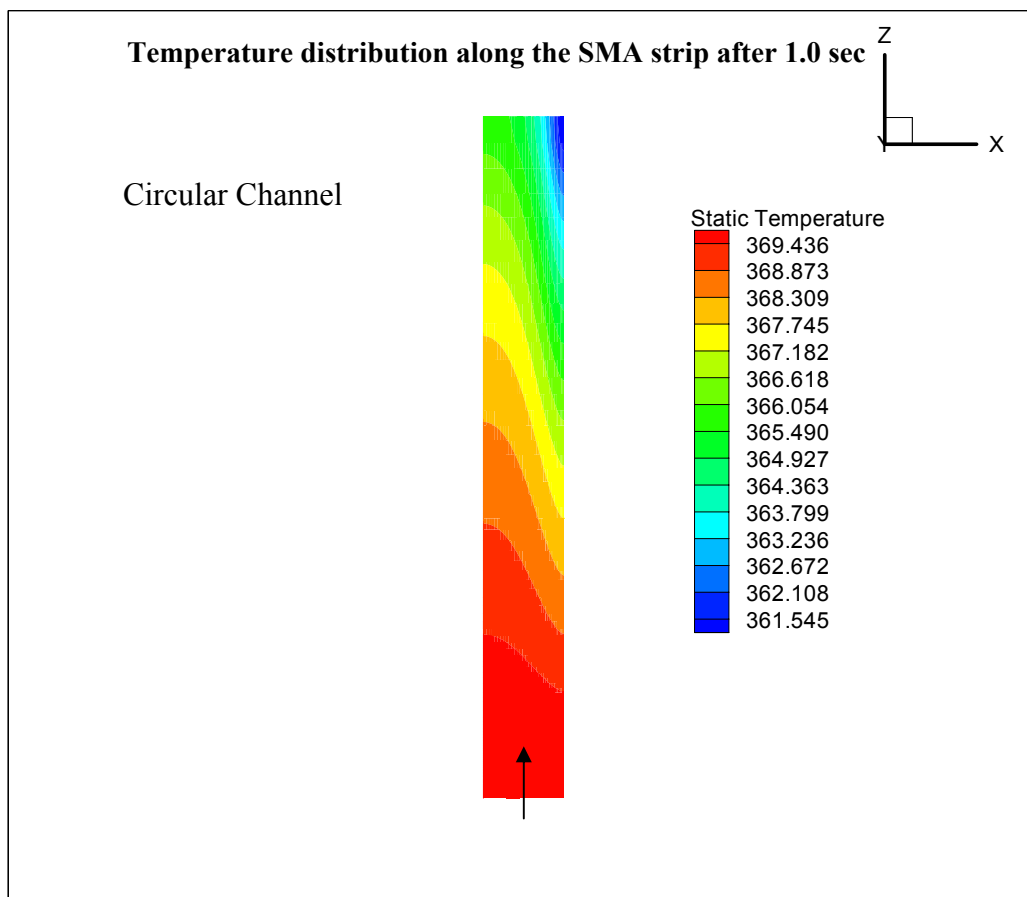
Figure 33. Temperature distribution-circular channel.
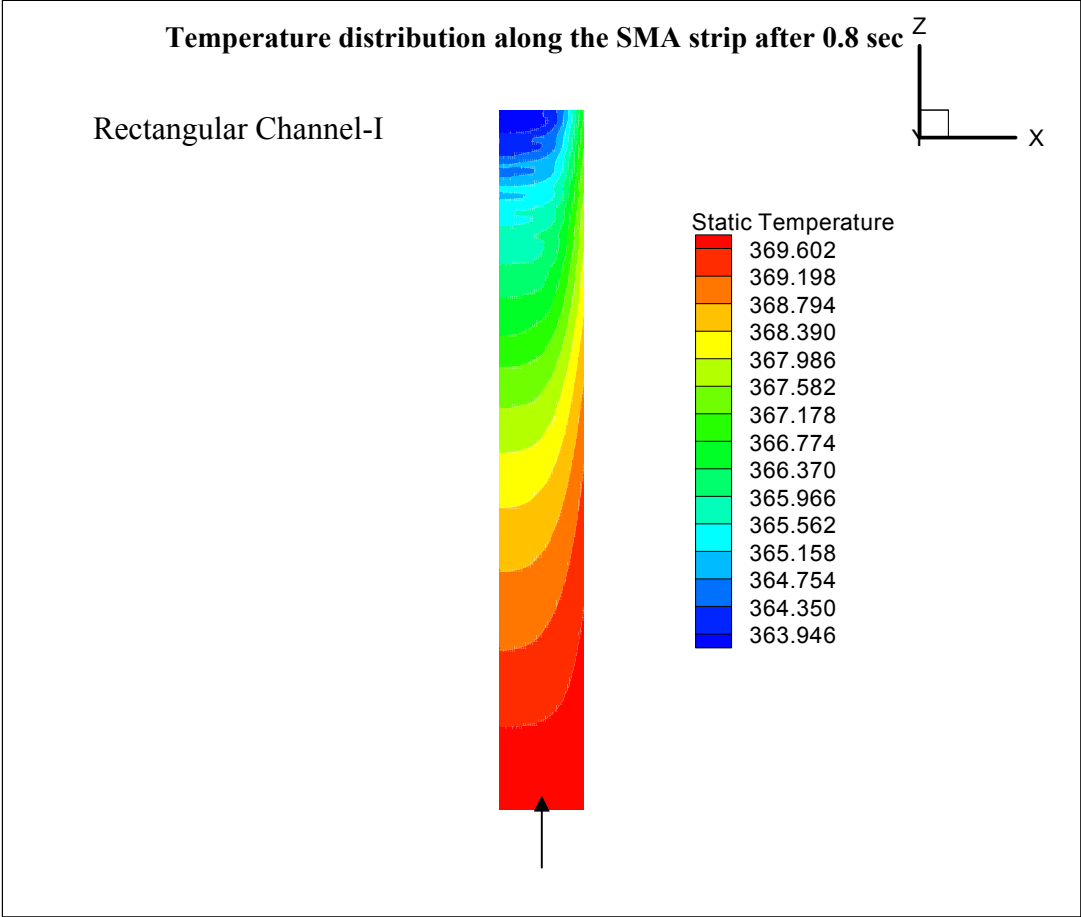
Figure 34. Temperature distribution-rectangular channel-I.
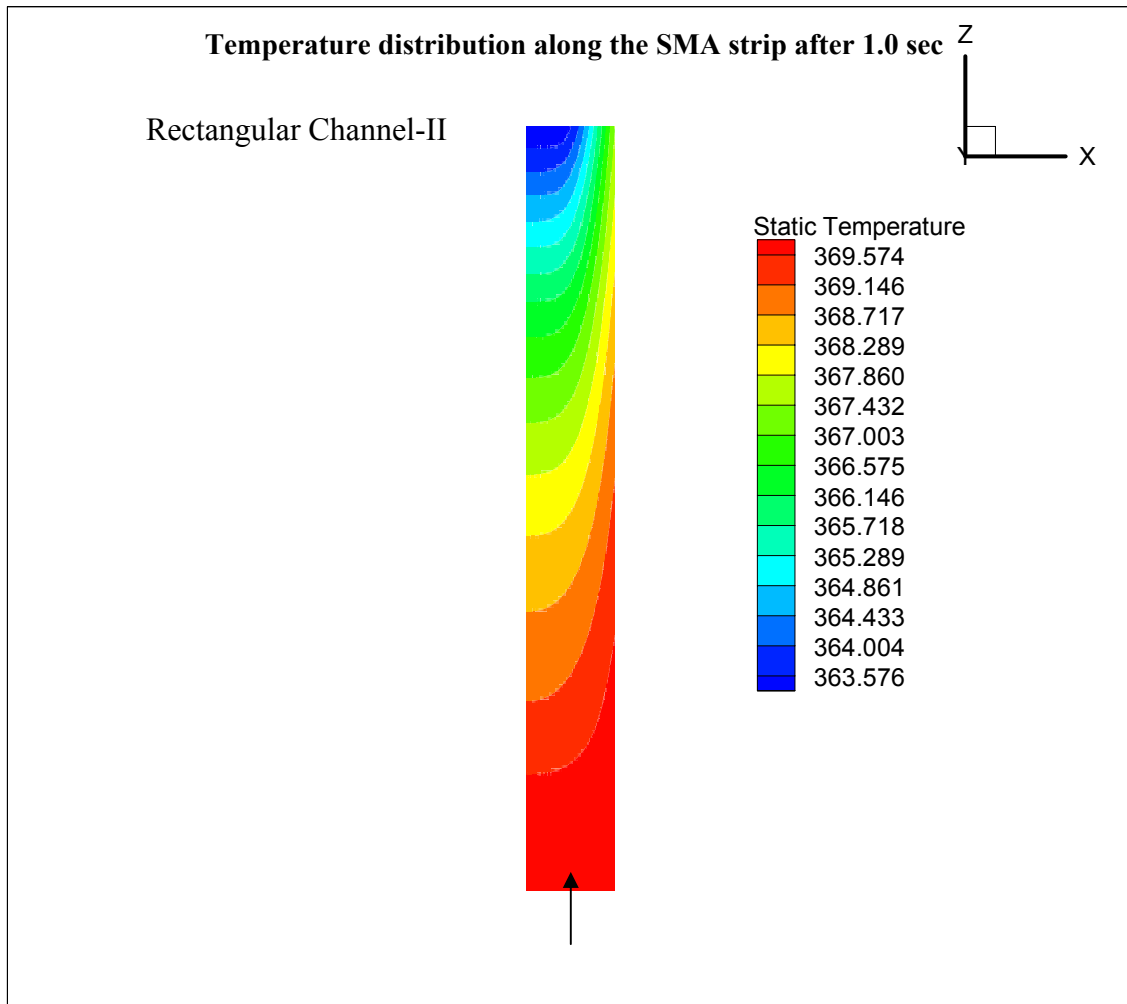
Figure 35. Temperature distribution-rectangular channel-II.

4.3 Conclusions

The numerical analysis was carried out to estimate the actuation frequency, recovery stress and strain. The circular channel case, which was the channel geometry of the first-generation SMA actuator, resulted in 0.5 Hz actuation frequency at 150 MPa of stress. The heating period of the first-generation actuator system under 150 MPa of stress was around 1.0 sec in the open-loop experimental tests. This value shows good agreement

with the numerical analysis for the circular channel case. From the results of the numerical analysis, we also selected the actuator channel for the second-generation actuator system to have rectangular geometry. However, in designing, the thermally-actuated SMA actuator, the transient heat transfer analysis with latent heat considerations must be carried out and confirmed numerically to determine the design parameters and operating conditions such as the inlet velocity and inlet temperature of the hot fluid and to estimate the actuation frequency of the SMA actuator.

CHAPTER V

THE SECOND-GENERATION FUEL-POWERED SMA ACTUATOR SYSTEM

5. The second-generation SMA actuator system

Figure shows schematics of the first and the second-generation actuator systems. The first-generation actuator system was composed of a pump, four solenoid valves, a bellows, a radiator, and a combustor/heat exchanger. The SMA element was embedded in circular silicon tubing. Heating and cooling medium alternatively circulated through the channel to achieve the M-to-A and A-to-M phase transformation of the SMA strip respectively. The heating fluid was heated through the burning of the fuel in the combustor. The cooling medium, after it removed the heat from the SMA strip, flowed through a radiator, where it disposed of the energy gained from the strip. An air cylinder was used as a bellows to prevent mixing between the hot and cold fluids caused by sharing common flow paths such as the actuator channel and the volume inside the pump. This mixing resulted in low actuator frequency of the first-generation actuator system even though the bellows was utilized to decrease the mixing.

The second-generation actuator system focuses on decreasing the mixing in order to increase the energy and power densities at the expense of simplicity of the system. The second-generation actuator system is made up of two pumps, four check valves, four solenoid valves, two bellows, a radiator, and a combustor/heat exchanger. The SMA element is embedded in a rectangular channel with a rectangular piston instead of

circular silicon tubing. The SMA element is connected to a loading frame to measure the

displacement and actuation force. Figure 37 shows the experimental setup of the second-

generation system and the newly designed loading frame.
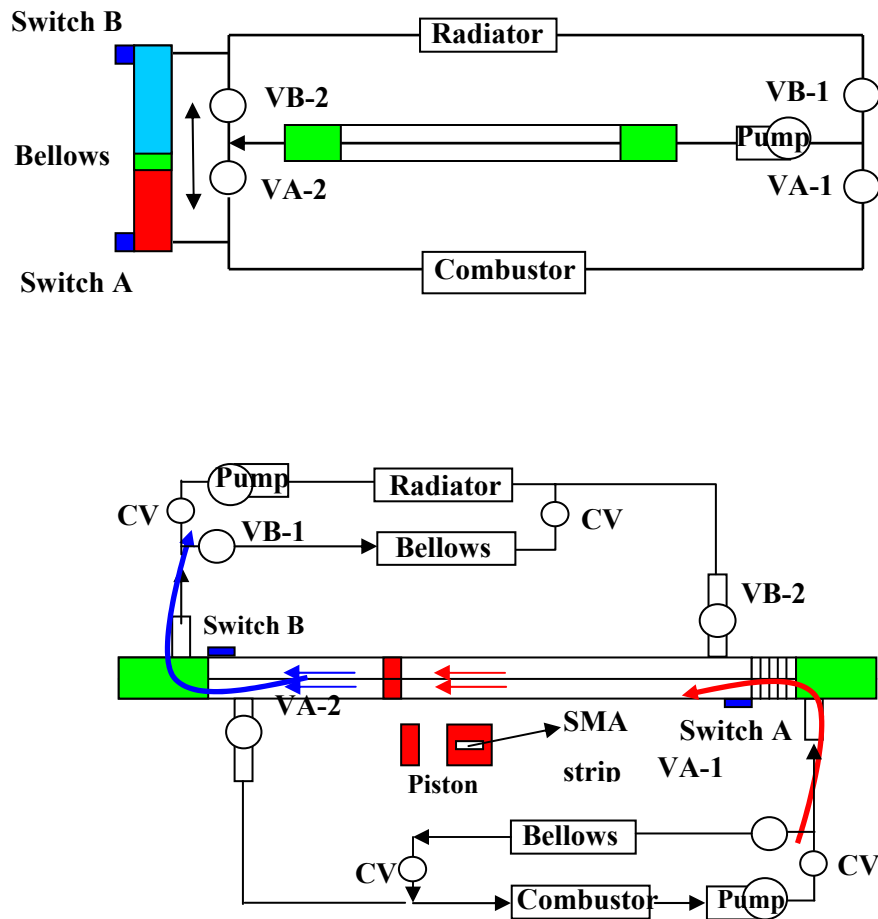
Figure 36. Schematics of the first-generation SMA actuator system (upper) and the

second-generation SMA actuator system (lower).

1. SMA Actuator
2. Radiator
3. Heater
4. Bellows
5. Pump
6. Valve
7. Linear Bearing
8. LVDT
9. Load Cell
10. Spring
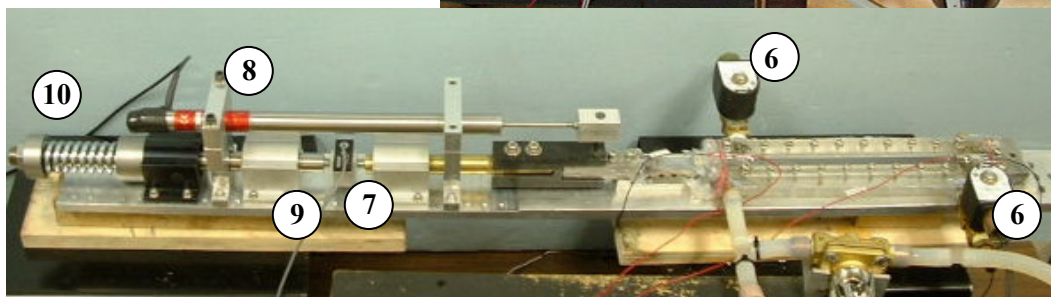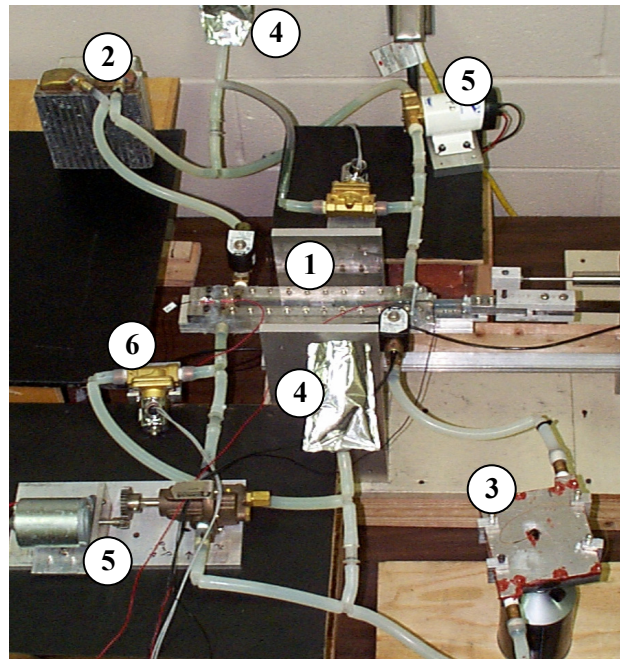
Figure 37. Experimental setup of the second-generation SMA actuator system

(upper) and the loading frame with the SMA actuator (lower).

5.1. Control and operating principles of the second-generation actuator system

The two pumps are controlled by on/off signals according to the pre-set actuation frequency of the actuator system. The on/off signals of the pumps and Hall effect switches, operated by a magnet in the rectangular piston, control the four solenoid valves. If the heating pump (pump A) is on, the hot fluid pushes the piston to the switch

B by driving hot water from the bellows. As soon as pump A is on, valve A-1 is closed

and valve B-1 is open. Thus, the cold fluid on the left side of the piston in the channel

goes into the cooling circuit. Finally this cold water goes into the bellows of the cooling

circuit. When the piston reaches the other end, the magnet on top of the rectangular

piston makes the Hall effect switch B go on. At that moment, valve B-1 is closed and

valve A-2 is opened. Thus the hot water passes through valve A-2, the combustor/heat

exchanger, pump A, valve A-1 and the channel. Finally the complete heating circuit is

built for given actuation frequency. Figure 38 shows the control logic of the SMA

actuator system. The hot water heats the SMA strip and gets energy at the

combustor/heat exchanger to compensate for its energy losses caused by the heat transfer

to the SMA strip and the mixing between the hot and cold water in the system. The

cooling circuit also works like the heating circuit as explained above.
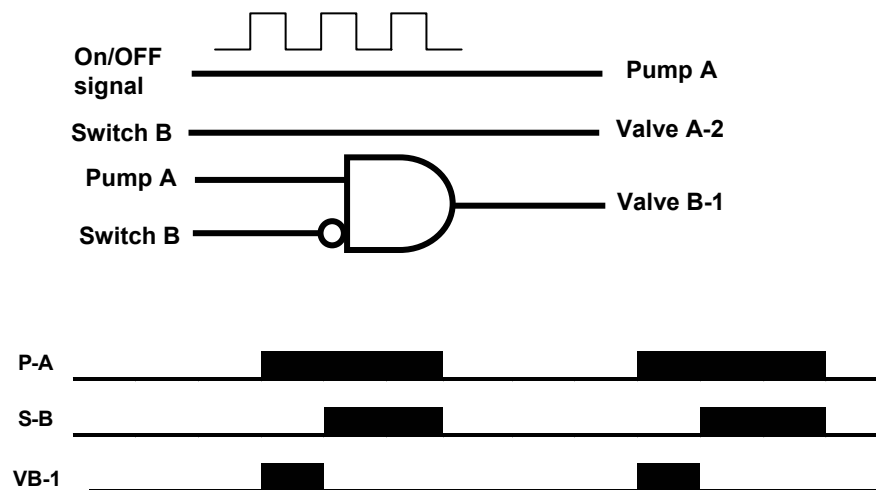
Figure 38. Control logic for the second-generation SMA actuator system.

5.2. Components of the SMA actuator system

5.2.1. SMA element and channel

A K-alloy type SMA strip, which is a Ni, Ti and Cu alloy, is used as the SMA element as in the first-generation system. Its cross section is 12 mm x 0.9 mm and its effective length is 254 mm. It was annealed at 450 °C for 20 minutes. We selected the rectangular channel-I, 7.6 mm x 17.8 mm in cross section in order to verify the newly designed channel concept (instead of the rectangular channel-II).

The channel is designed to decrease the mixing between hot and cold fluid in the system. Figure 39 shows the SMA element and the rectangular channel. It is composed of two end connectors, rectangular channel, top plate, Teflon tube, piston with magnet and a SMA strip. RTV and screws were utilized to seal the channel. The function of the rectangular piston is to separate the hot and cold fluids thus decreasing the mixing. The rectangular piston has a slot in the middle of its cross section to accommodate the SMA strip and runs along the SMA strip. The piston has a magnet on top of it in order to turn the solenoid valves on and off according to the heating and cooling cycles. One of the ends of the SMA element (left end in Figure 39) was embedded in flexible silicon tubing in order to accommodate the expansion and contraction of the SMA strip.
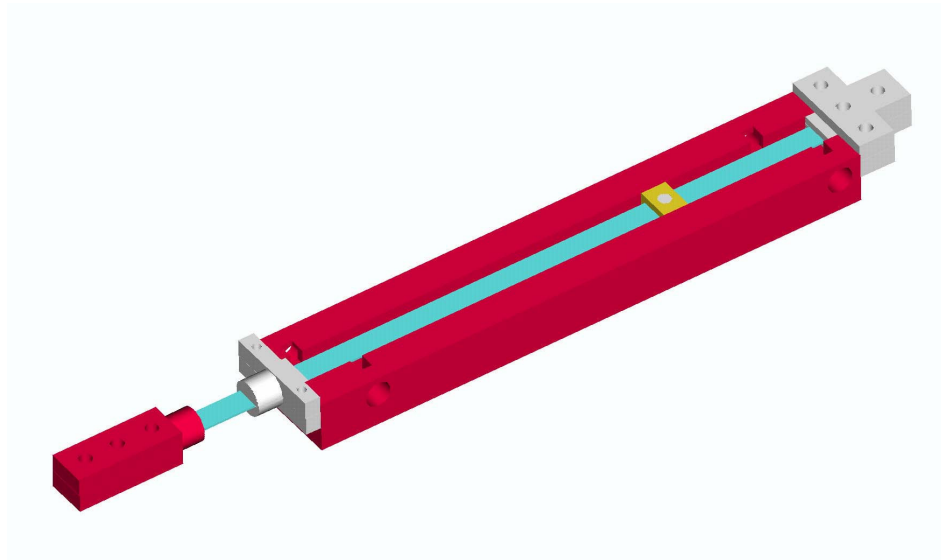
Figure 39. SMA actuator.

5.2.2. Loading frame

The loading frame is composed of 3 linear bearings, a compression spring, a load cell, a LVDT and an aluminum frame. The restoring force is generated by the compression spring. The initial stress and recovery stress of the SMA strip are adjustable by changing the spring force or spring constant. The compression spring has the following dimensions: 31.3 mm outside diameter and 89 mm overall length. Its spring coefficient is 63.6 N/mm. A 1335 N load cell (by Transducer Techniques) measures the actuation force of the SMA strip. A LVDT is used to measure the recovery strain.

5.2.3. Combustor and hot fluid tank

A compact commercial propane burner and an aluminum hot fluid tank, which were used for the first-generation SMA actuator system, were utilized as a combustor/heat

exchanger for the second-generation actuator system. Figure 20 shows this propane burner and hot fluid tank.

5.2.4. Heat exchanger (radiator)

The PC cooling heat exchanger with a fan having 59.2 l/min (125.5 CFM) flow rate was used as a heat exchanger. It measures 152 mm x 178 mm x 5.1 mm.

5.2.5. Pumps

The brass Omega FPUGR201 gear pump circulates the heating medium. Its maximum flow rate is 7.95 l/min at low-pressure loss and can withstand 0.69 MPa and 149 °C. A DC motor runs the pump. The Reverso GP-301 gear pump system circulates the cooling medium up to 11.4 l/min. The pumps run alternatively according to the heating and cooling cycles.

5.2.6. Valves

Four solenoid valves were utilized to control the heating and cooling circuits. The valves in the heating circuit are 3.3-Cv GC direct-operated-diaphragm 2-way solenoid valves. The cooling circuit valves are 0.83-Cv Parker direct-acting valves. Four check valves were used to prevent reverse flows in the system.

5.2.7. Bellows

Two flexible bags are used in the second-generation actuator system as bellows unlike the first-generation actuator system where a cylinder was used as bellows to decrease the mixing and to decrease pressure losses in the system. Each circuit has one bag/bellows as shown in Figure 36. Figure 40 shows the flexible bag working as bellows in the system.

Figure 40. Bellows for the second-generation actuator system.

5.2.8. Switches

The Hall effect magnetic sensor detects the presence of a magnetic field. A small, permanent magnet embedded on top of the rectangular piston is easily detected with this sensor. Two Hall effect switches were used to control the solenoid valves, thus alternatively turning the heating and cooling circuits on and off. Figure 41 shows the Hall effect sensor and reed switch.
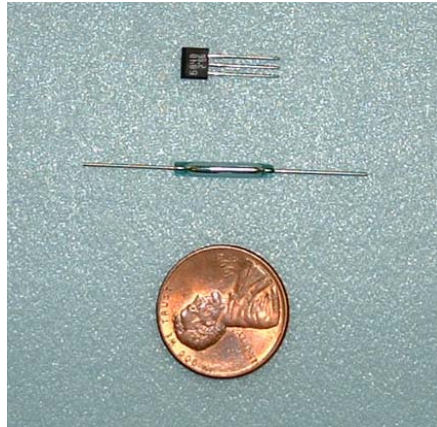
Figure 41. Reed switch and Hall effect switch.

5.2.9. Control and data acquisition

A National Instrument AT-MIO-16XE-50 board, which has 16-bit resolution and eight differential inputs, is used to acquire the temperature, displacement and force. A National Instrument PCI-6704 D/A board was utilized to control the pumps. A Lab-Windows program was put together to control the hardware and acquire data.

5.3. Test results for the second-generation actuator system

Water was used as the heating and cooling medium by considering the transformation temperatures of the SMA strip, as in the first-generation SMA actuator system. The actuator was connected to the loading frame instead of the amplification device of the first-generation system. For the actuation tests, the restoring force was initially adjusted to around 350 N (34 MPa) considering the displacement of the SMA actuator and the spring constant. After SMA transformation, the force was increased to 735 N (71 MPa). The displacement variation was 5.5 mm (2.17 % strain).

Figure 42 shows the results for the second-generation actuator system. The actuation frequency of the 2nd actuator system was 0.25 Hz, the heating period was 2 seconds and the cooling period was 2 seconds. Figure 43 shows the actuation force of the SMA element. The ranges of force and the displacement never decreased during the test. While the range of the displacement for the first-generation system reduced at later cycles, the second-generation actuator system overcame this problem by reducing the mixing at 0.25 Hz actuation frequency. But the actuation frequency was lower than that of the open-loop system, where the actuation frequency was 1.0 Hz. The main reason for this is the mixing. The fluid can pass through the small gap between the channel wall and the piston and through the slot in the middle of the piston due to the poor sealing conditions, thus causing the mixing between hot and cold fluids. The second-generation actuator system utilized two pumps and a rectangular channel with rectangular piston to decrease the mixing. The pressure losses due to the movement of the piston during the heating and cooling cycles caused slow flow in the channel compared to the open-loop system. This also resulted in low actuation frequency along with the mixing. Though the actuation frequency is lower than that of the open-loop system, the second-generation actuator system can actuate the SMA element 2.5 times faster than that of the first-generation actuator system under similar conditions. Also, the tests hinted to the possibility of increasing the actuation frequency by modifying the system, by replacing the camping stove and the aluminum block with the multi-channel combustor/heat exchanger that will be discussed in the next section and by using high boiling point fluid such as ethylene glycol.
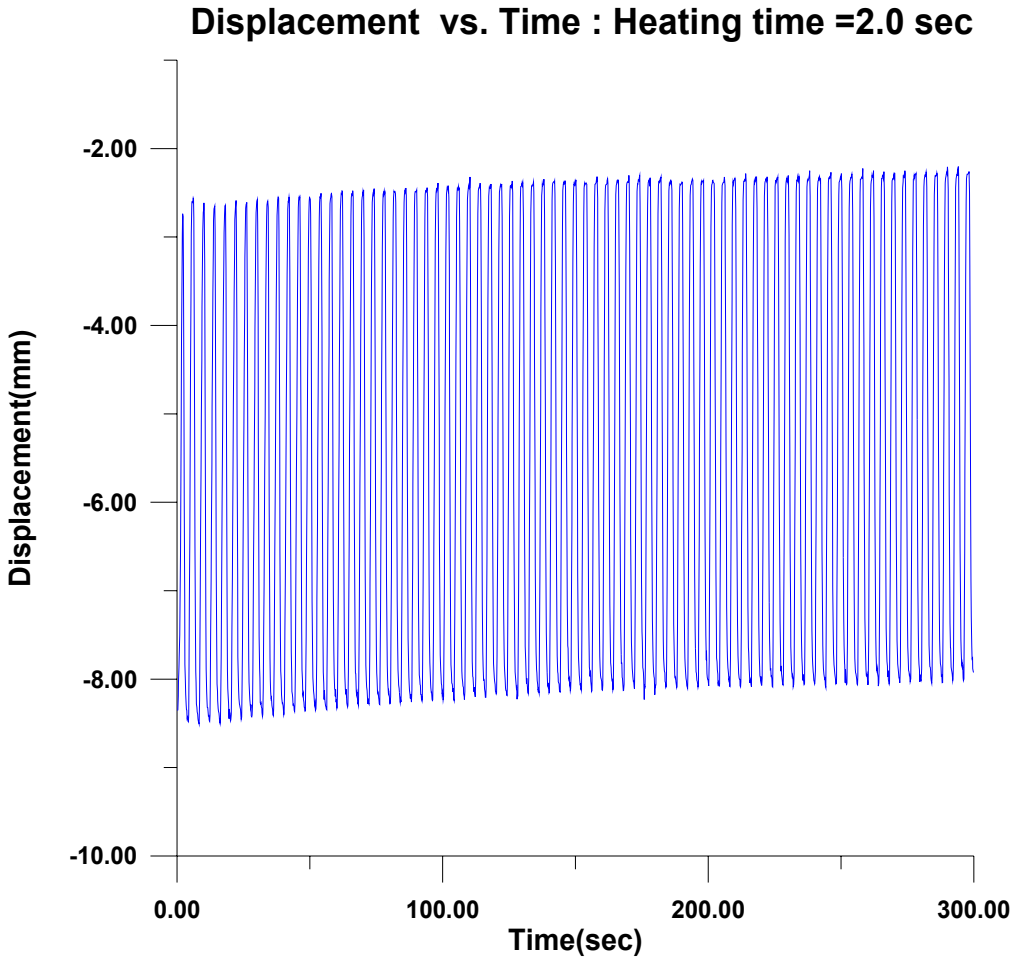
Figure 42. Displacement vs. time for the second-generation system.

Force vs. Time : Heating time =2.0 sec
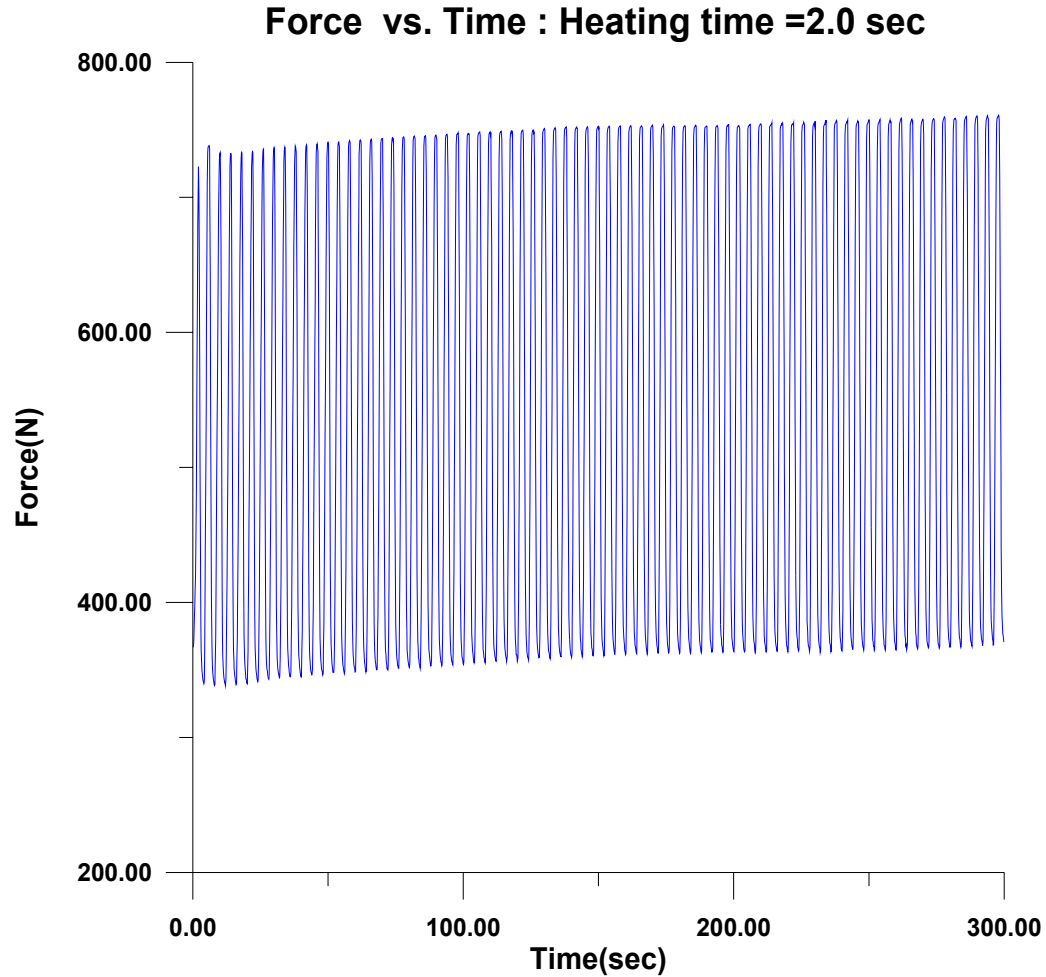
Figure 43. Force vs. time for the second-generation system.

5.4. Conclusions

The first-generation actuator system was modified and improved to increase the actuation frequency and to achieve high energy and power densities. A rectangular channel, with a rectangular piston running along it, was selected to house the SMA strip in order to decrease the mixing in the 2nd SMA actuator system. Also, two flexible bags were used as bellows instead of the cylinder utilized in the first-generation actuator

system in order to decrease the mixing and pressure losses. The on/off signals of the pumps and Hall effect switches, operated by a magnet in rectangular piston, controlled the four solenoid valves efficiently, thus operating the heating and cooling circuits alternatively, hence the mixing was decreased compared to the first-generation actuator system. The second-generation actuator system generated 735 N recovery force (71 MPa stress) and 5.5 mm displacement and had 2.5 times faster actuation frequency in the closed-loop configuration.

CHAPTER VI

MULTI-CHANNEL COMBUSTOR/HEAT EXCHANGER

6. Combustor/heat exchanger

The combustor/heat exchanger is an important unit for the supply of hot fluid in the SMA system by burning fuel and heating hot fluid. But it does not have to be used if other sources of hot fluid, such as exhaust hot fluid or steam from a power plant, are available. There are several kinds of porous medium burners, which have high energy efficiency and high turn down ratio, in other words the firing intensity of the burner can be easily modulated.

6.1. Porous material burner (surface combustion burner)

The design of the multi-channel combustion/heat exchanger is based on surface combustion resulting in a single frame. The surface combustion is one in which premixed gas and air burns on the surface of a porous medium or inside of a porous medium according to the flow rate of fuel and air. Surface combustion burners have high energy efficiency and are utilized as a source of thermal radiation or as a stable premixed burner with low-NOx emissions [36]. Surface combustion of premixed gases in porous material burners, such as metal fiber burners, can occur in two modes, according to the combustion load and the air ratio. In radiant mode with a red/orange flame, combustion occurs inside the mat (porous medium), which heats to incandescence and releases a

71

portion of the energy input as thermal radiation. As flow rate increases, the flame becomes blue and might lift off the surface of the porous medium, resulting in little radiation from the relatively cool porous medium and releasing most of the energy through convection [37]. Thus this is called as thus to "blue-flame mode". Figure 44 shows a schematic of a porous material burner.
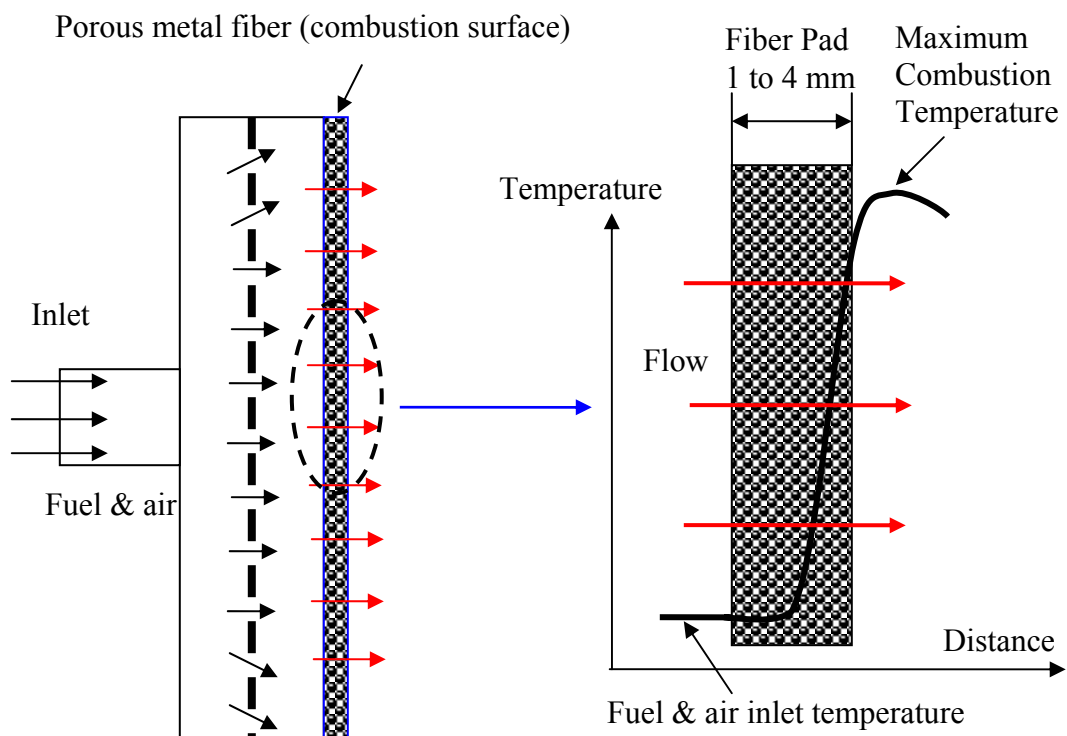
Figure 44. Schematic of porous medium burner [38].

It has been known that surface combustion performance is dependent on the properties of the porous medium, the condition of the combustor and the fuel properties [39]. The porous medium can take many forms, such as metal fibers, sintered metal plate, bonded hollow spheres, ceramic foam, etc. This kind of burner has the following

characteristics. 1) Low thermal inertia – due to the high porosity of the porous medium, the burner can be in the fully-powered state within a few seconds after firing. 2) Low CO and NOx – due to the intimate contact between the gases and the porous medium, especially in the case of metal fibers, the flame temperature is significantly reduced causing far lower NOx levels than other burners. 3) Noise—Noise free and resonance free combustion. 4) Flash back— no self-ignition will occur, even under low ignition temperature gases such as propane, butane or hydrogen containing gases. 5) Fast cool down – the cooling down of the porous medium is so fast that the burner surface can be cooled within a few seconds [37].

6.2. The first–generation design of combustor/heat exchanger

The design of the combustor/heat exchanger was based on Drost's [22] combustor/evaporator with multiple channels. We modified their design to satisfy our requirements. Especially the power was increased up to 4 KW and the flow rate was increased from 20 ml/min to 7.6 l/min or higher in order to use it as heat exchanger instead of evaporator. The compressed air and fuel, such as propane, are introduced into the mixing chamber passing through the nozzles. A porous metal sheet, a sintered metal plate, is utilized to make a blue flame burner or combustor. This metal plate generates a laminar flame and works as a flame arrestor, which prevents flash back. We use a 53.3 mm x 147.3 mm x 1.6 mm Mott's porous metal sheet. The grain size was 2 micrometer. The blue flame combustion has high output power, high efficiency and low pollutants compared to convectional combustion. There are several kinds of porous material

burners in the market such as ceramic burners [40, 41] and metal fiber burners [37]. The output power [40] of one of the ceramic burners ranges from 100 KW/m^2 to 600 KW/m^2 in radiating power mode and from 600 KW/m^2 to 2000 KW/m^2 in convection power mode. Also, the flame height can be decreased, thus the overall size of the device can be decreased. Figure 45 and Figure 46 show the structure of the combustor/heat exchanger. Figure 47 shows the 1st prototype of combustor/heat exchanger. It is composed of the heat exchanger, the combustion chamber, the mixing chamber and the porous metal sheet. The gases burn in the combustion chamber, which is 149.9 mm x 73.7 mm x 25 mm. We give enough height to the combustion chamber to prevent quenching of the flame and to decrease the generation of CO due to the cold wall. A 0.81 mm stainless wire and a tube-type ceramic insulator were used to make an ignitor which was inserted into the combustion chamber. This electric ignitor generates plasma between the ceramic insulated wire and the porous metal sheet, thus starting burning. The exhaust gas passes through the multiple channels and transfers most of its energy to the heat exchanger and finally to the fluid. Also the heat exchanger has a lot of channels in order to enhance the heat transfer between the exhaust gas and transfer it to the fluid passing through the channels. The channels on the combustor side have dimensions of 5.1 mm in height, 35.6 mm in length and 0.81 mm in spacing. The channels on the heat exchanger side have dimensions of 15.2 mm in height, 104.1 mm in length and 0.81 mm in spacing between channels. The total number of channels is 91 x 2 for each side, i.e. combustor and heat exchanger sides. The unit's overall dimensions are 22.9 mm x 114.3 mm x 162.6 mm. The combustor/heat exchanger was made of aluminum and the channels were

machined using a slitting saw in a CNC machine. Ceramic fiber paper was used as insulator and sealant between the porous metal and the combustion chamber. The ceramic fiber paper specifically can allow the thermal expansion of the porous metal sheet and can withstand high temperature. The diffusers were designed and manufactured in a Rapid Prototyping (RP) machine out of ABS plastic to equally distribute the flow rate in the heat exchanger. The diffuser has 5 passages inside of it. RTV and screws were used for the sealing of the combustor and heat exchanger.
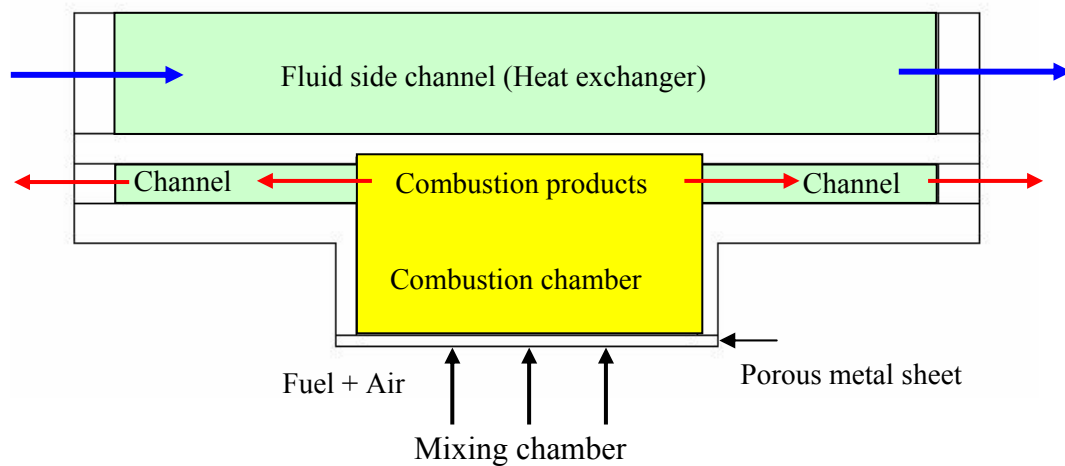
Figure 45. Structure of the combustor/heat exchanger.

To increase mixing between air and fuel in the mixing chamber, four air inlets and one fuel inlet are utilized as shown in Figure 45. The premixed gases by the nozzles in inlet the duct pass through the mixing chamber as shown in Figure 48 and finally pass through the porous metal plate and burn over it.

Diffuser

Heat Exchanger
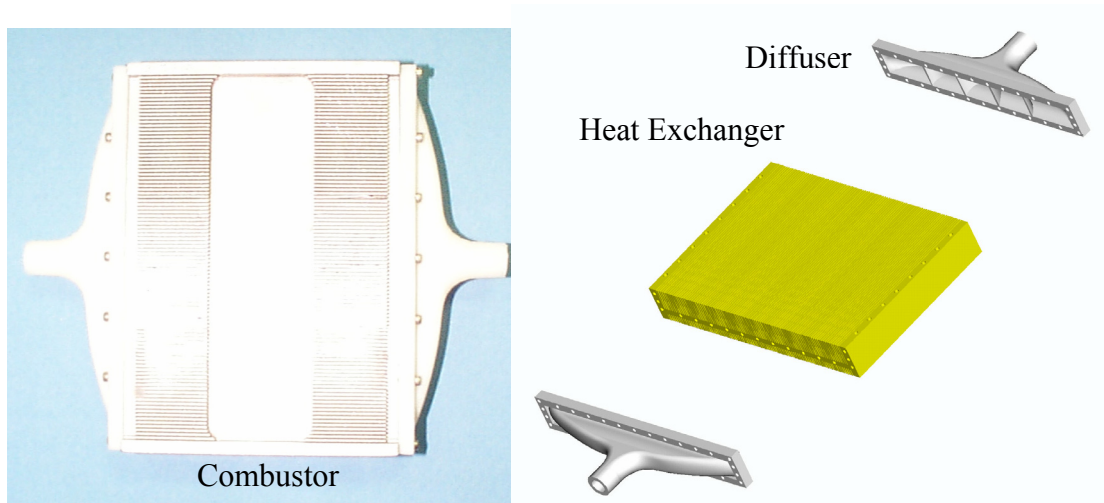
Combustor

Figure 46. Combustor /heat exchanger.
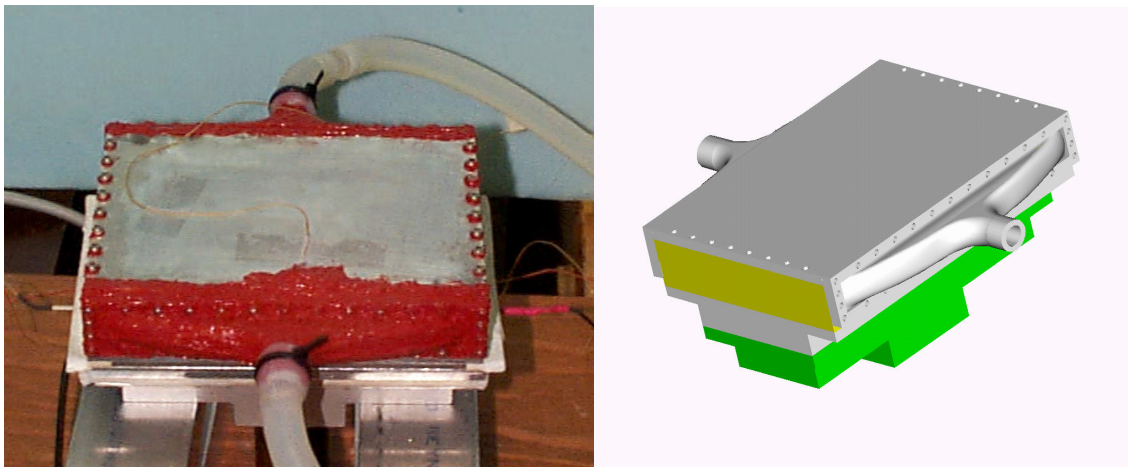
Figure 47. 1st prototype of combustor/heat exchanger.
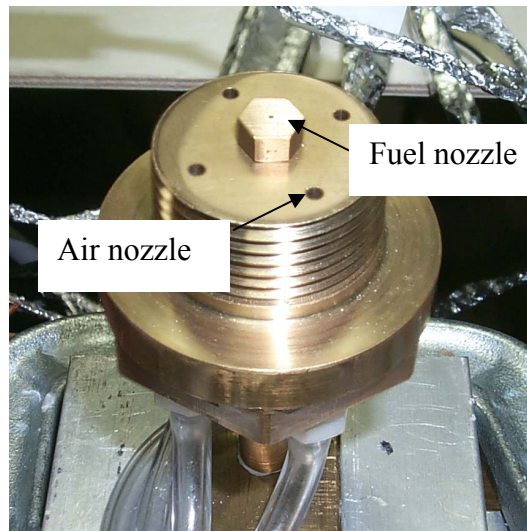
Figure 48. Air nozzles and fuel nozzle of combustor.

6.2.1. Experimental setup

Figure 49 shows the experimental setup for the performance test of the multi-channel combustor/heat exchanger. The flow rates of fuel, fluid and air were measured using rotameters. The air supplied by a compressed air system is passed through the air filter to remove moisture and oil. A 450g-propane cartridge supplies the fuel. Five thermocouples were used to measure the temperature of gases, fluid, heat exchanger and combustion chamber. Distilled water was used as the working fluid to prevent corrosion of aluminum and was circulated by the submersible pump. A rotameter controlled the flow rate of the water during the test. All data was monitored and stored by a National Instrument data acquisition board and a Lab-Windows program.
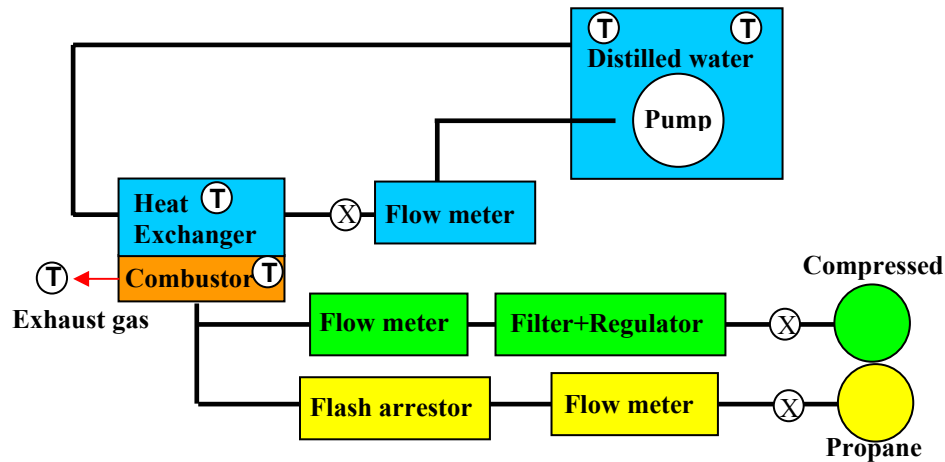
Figure 49. Test setup for combustor/heat exchanger

6.2.2. Test results

4 liters of distilled water were utilized as the working fluid for the performance test. The flow rate was set as 0.5 GPM (1.89 l/min). The fuel flow rate was also set at 1.2 l/min (around 2 KW) and the airflow rate was set at 80 SCFH. Thus the air to fuel ratio was around 1.1.

Figure 50 shows the temperature increase in the water tank with time. The obtained energy passing through the heat exchanger can be calculated from the slope of the plot. The slope is 0.084 °C /sec and the total increment of the water temperature is 25°C. The combustor/heat exchanger efficiency is defined as the ratio of the energy added to the fuel energy. The unit has approximately 70 % efficiency at given conditions.

Figure 51 shows the temperature variation in the water tank using a propane burner and an aluminum block, which were used for the first- and second-generation

systems. It is difficult to measure the efficiency of them due to the uncertainty in the fuel flow rate of the camping stove. But it shows that the temperature increment is smaller than that of the multi-channel combustor/heat exchanger under similar test conditions. The temperature slope is 0.06 °C/sec, which is lower than the value of the multi-channel combustor/heat exchanger.

Temperature in reservoir vs. time

Fluid: water
Flow rate: 0.5 GPM
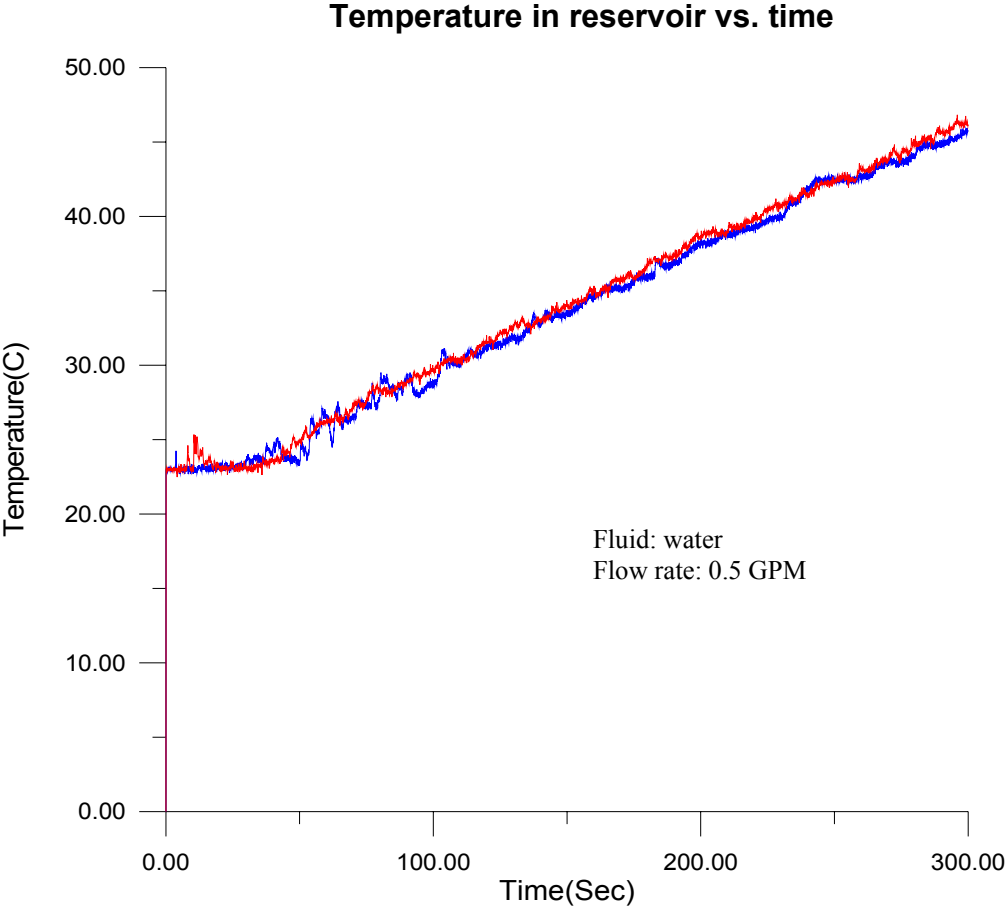
Figure 50. Water temperature increment by combustor/heat exchanger.

79
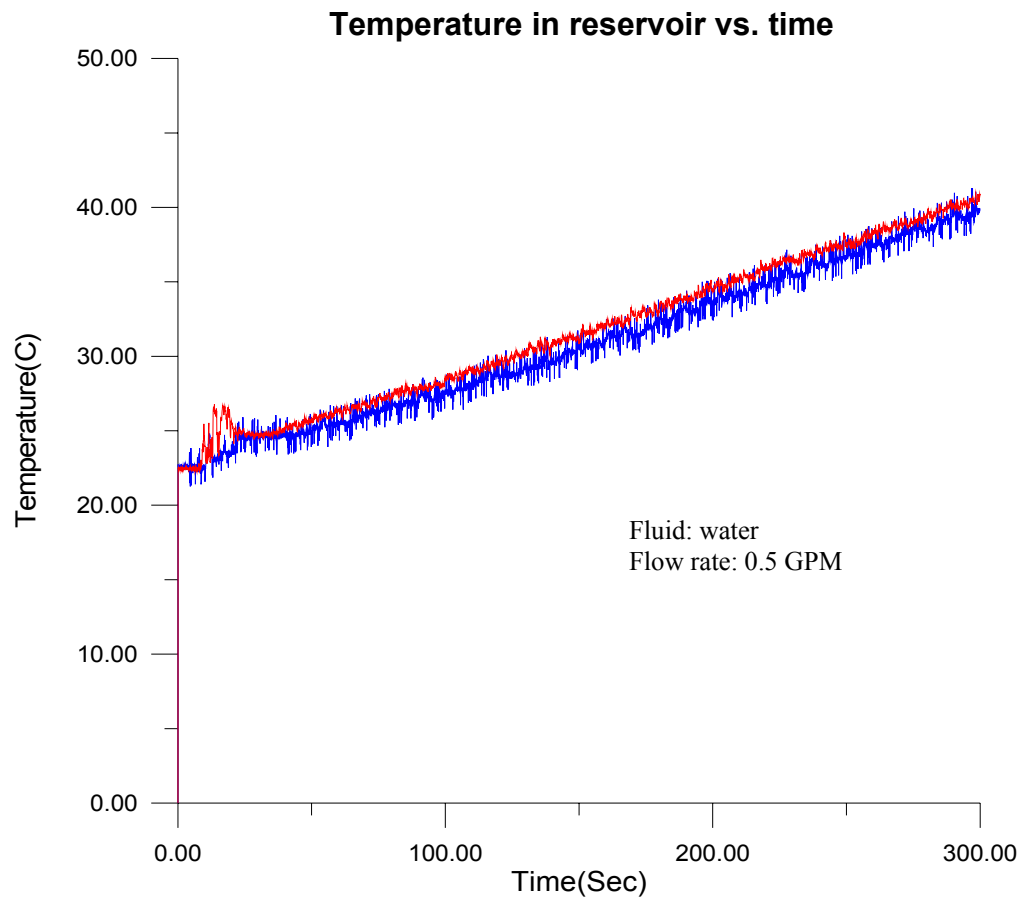
Figure 51. Water temperature increment by propane burner and aluminum block.

Thus the first-generation designed combustor/heat exchanger has better heat transfer rate and better energy efficiency compared to the propane burner and the aluminum block. This combustor/heat exchanger was designed and fabricated for the second-generation SMA actuator system.

6.3. The second-generation design of combustor/heat exchanger

For the final actuator system, for which a smaller size of SMA strip, as compared to the second-generation system, was utilized, the combustor/heat exchanger requirements are changed due to different power requirements of the new SMA strip. The first generation combustor/heat exchanger was made of aluminum material due to its high thermal conductivity, lightness and machining ability, while the soldering or welding was difficult. Thus screws and RTV (high temperature silicon) were used to seal the combustor and heat exchanger. The structure, material and machining techniques of the combustor/heat exchanger are exactly the same as in the first generation combustor/heat exchanger developed for the second-generation actuator system.

6.3.1. Numerical heat transfer analysis of combustor/heat exchanger

The heat transfer rate through the channels can be estimated by using the thermal resistance method for a fin system. Figure 52 shows the schematic of the unit cell of te combustor/heat exchanger, in which the fluid passes through the channel and gets the energy from hot hot exhaust gases.
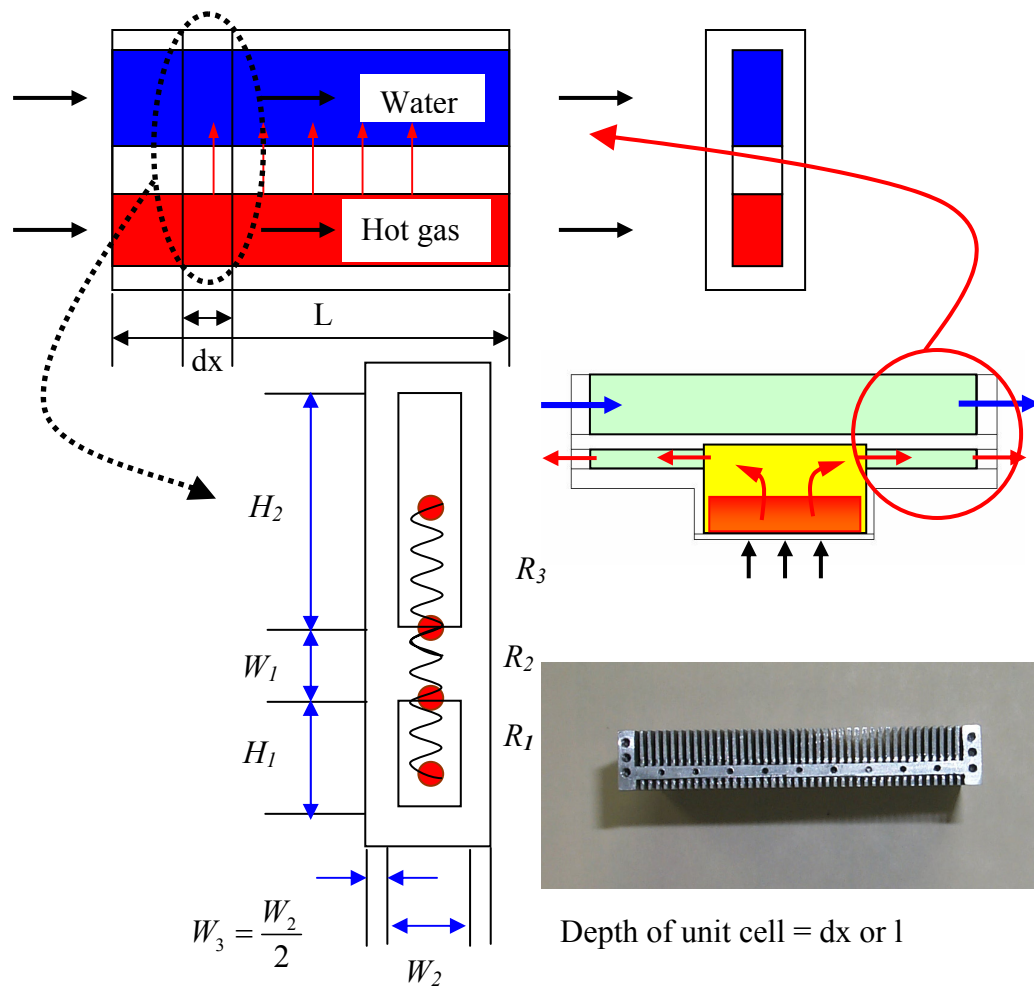
Figure 52. Unit cell and thermal resistance network between channels.

The heat transfer in the combustor/heat exchanger is treated as a steady state problem and the flow in the channel is also assumed as fully developed and laminar. The control volume is one fluid and hot gas channel, which is one of right side channels of the combustor/heat exchanger as shown in Figure 52, and most of the energy is assumed to be transferred through the channel by forced convection heat transfer.

6.3.1.1. Heat transfer

By using heat transfer theory of fins, per unit length (l= dx), the resistances, R_1, R_2 and R_3 [23] can be defined such as,

$$R_1 = \frac{1}{h_1 \cdot (2 \cdot H_1 \cdot \eta_1 + W_2) \cdot l} \tag{12}$$

$$R_2 = \frac{W_1}{K_2 \cdot (2 \cdot W_3 + W_2) \cdot l} \tag{13}$$

$$R_3 = \frac{1}{h_2 \cdot (2 \cdot H_2 \cdot \eta_2 + W_2) \cdot l} \tag{14}$$

$$R_{tot} = R_1 + R_2 + R_3 \tag{15}$$

R_1 is the convective resistance between the hot exhaust gases and the wall. R_2 is the conductive resistance through the wall of separating the hot gases and the fluid. R_3 is the convective resistance between the fluid and the wall. R_{tot}, the sum of R_1, R_2 and R_3, is the resistance from the combustor channel to the fluid channel.

If the Re number is less than 2300, the flow is laminar and expressions of Nu, the heat transfer coefficient and the friction coefficient are given by [42]:

$$Nu = -1.047 + 9.326 \cdot G_i \tag{16}$$

$$f = 4 \cdot \left[\frac{4.7 + 19.64 \cdot G_i}{\text{Re}} \right] \tag{17}$$

Where $G_i = \dfrac{\left(\dfrac{W_2}{D_{hi}}\right)^2 + 1}{\left(\dfrac{W_2}{D_{hi}} + 1\right)}$ and $h_i = \dfrac{k_i \cdot Nu_i}{D_{hi}}$.

The pressure drop across the channel is given by [43]:

$$\Delta p = \frac{f \cdot \rho \cdot V^2 \cdot L}{2 \cdot D_h} + K \cdot \frac{\rho \cdot V_2}{2} \tag{18}$$

The fin efficiency η is defined as,

$$m_i = \sqrt{\frac{h_i \cdot P_c}{k_i \cdot A_c}} = \sqrt{\frac{h_i \cdot 2 \cdot (W_2 + l)}{k_i \cdot W_2 \cdot l}} \tag{19}$$

$$\eta_i = \frac{\tanh(m_i \cdot H_i)}{m_i \cdot H_i} \tag{20}$$

For the parallel-flow heat exchanger [44],

$$\ln\left[\frac{T_{g,oulet} - T_{w,outlet}}{T_{g,inlet} - T_{w,inlet}}\right] = -\frac{U \cdot A}{C_{min}}\left(1 + \frac{C_{min}}{C_{max}}\right) \tag{21}$$

Where $C_{min} = \left(\dot{m} \cdot C_p\right)_{min}$

If C_{min} is very small compared to C_{max}, the equation becomes

$$\ln\left[\frac{T_{g,oulet} - T_{w,outlet}}{T_{g,inlet} - T_{w,inlet}}\right] = -\frac{U \cdot A}{C_{min}}, U = \frac{1}{R_{tot}} \tag{22}$$

Finally we get the following equation for the fluid and the hot gas.

$$\left[\frac{T_{g,oulet} - T_{w,outlet}}{T_{g,inlet} - T_{w,inlet}}\right] = \exp\left(-\frac{U \cdot A}{C_{min}}\right) = \exp\left(-\frac{1}{\dot{m}_g \cdot C_{pg} \cdot R_{tot}}\right) \tag{23}$$

$$q_{channel} = \dot{m}_g \cdot C_{pg} \cdot \left(T_{g,inlet} - T_{g,outlet}\right) \tag{24}$$

$$q = \dot{m}_w \cdot C_{pw} \cdot \left(T_{w,outlet} - T_{w,inlet}\right) \tag{25}$$

There are three unknown variables, $T_{w,oulet}, T_{g,outlet}$ and $q = q_{channel}$, and three equations.

Thus, we can get the outlet temperatures of the fluid and the gas.

6.3.1.2. Exhaust gas properties

We considered methane and propane as possible fuels for the SMA actuator system. The gas properties must be considered as functions of temperature because of the high temperature variation passing through the channel. By using the property functions of EES (Engineering Equation Solver), methane and propane gas properties are obtained easily. If there is 20 % excess air (x= 20) in the combustion of propane, the reaction equation is given by [45];

$$C_3H_8 + 5 \cdot (1 + x/100) \cdot (O_2 + 3.76 \cdot N_2) \Leftrightarrow 3CO_2 + 4 \cdot H_2O + 3.76 \cdot 5(1 + 1 \cdot x/100) \cdot N_2 + 5 \cdot x/100 \cdot O_2$$

$$C_3H_8 + 5 \cdot 1.2 \cdot (O_2 + 3.76 \cdot N_2) \Leftrightarrow 3CO_2 + 4 \cdot H_2O + 3.76 \cdot 5 \cdot 1.2 \cdot N_2 + 5 \cdot 0.2 \cdot O_2 \quad (26)$$
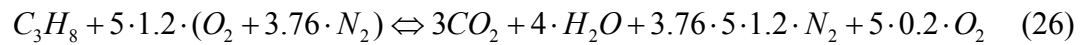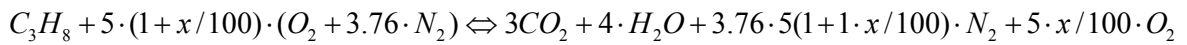
Especially specific heat, thermal conductivity and density are functions of temperature. The mixed gas properties are obtained by using the following relations.

Mole ratios of the gases;

$$Y_{CO_2} = 3/N_{tot}$$

$$Y_{H_2O} = 4/N_{tot}$$

$$Y_{O_2} = 5 \cdot (x/100)/N_{tot}$$

$$Y_{N_2} = 3.76 \cdot 5 \cdot (1 + x/100)/N_{tot}$$

Where N_{tot} is the total number of moles.

The molecular weight of gases is also important to get the gas properties;

$$M_{CO_2} = Y_{CO_2} \cdot 44$$

$$M_{H_2O} = Y_{H_2O} \cdot 18$$

$$M_{O_2} = Y_{O_2} \cdot 32$$

$$M_{N_2} = Y_{N_2} \cdot 28$$

The total mass (kg/kmol) of the gas mixture is $M_{gas} = M_{CO_2} + M_{H_2O} + M_{O_2} + M_{N_2}$.

The ratio of gases, on a mass basis is;

$$M1 = M_{CO_2} / M_{gas}, \quad M2 = M_{H_2O} / M_{gas}, \quad M3 = M_{O_2} / M_{gas}, \quad M4 = M_{N_2} / M_{gas}$$

The specific heat of the gas mixture is given by;

$$C_{pg} = Y_{CO_2} \cdot C_{pCO_2} + Y_{H_2O} \cdot C_{pH_2O} + Y_{O_2} \cdot C_{pO_2} + Y_{N_2} \cdot C_{pN_2} \tag{27}$$

Where $C_{pCO_2}, C_{pH_2O}, C_{pO_2}$ and C_{pN_2} can be obtained from the EES as functions of temperature. The thermal conductivity and specific heat of the gas mixture are obtained as function of temperature. Figure 53 shows the thermal conductivity and specific heat of the exhaust gases as functions of temperature.
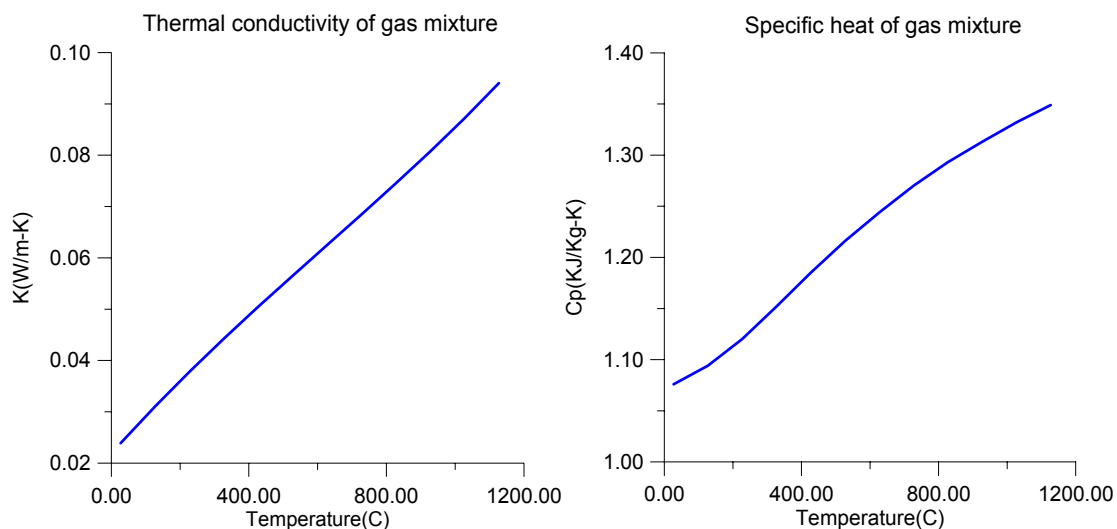
Figure 53. Specific heat and thermal conductivity of exhaust gas.

6.3.1.3. The result of heat transfer at given channel geometry

Figure 54 and Figure 55 show temperature distributions along the channels of the combustor and heat exchanger. The fuel is propane and the excess air ratio x is 20%. The dimensions of the multi-channel section used for the calculations are 0.81 mm x 2.5 mm x 25.4 mm (0.032 inch x 0.1 inch x 1.0 inch) for the hot gas side channels (combustor channel) and 0.81 mm x 7.6 mm x 2.5 mm (0.032 inch x 0.3 inch x 1.0 inch) for the fluid side channels (heat exchanger channel). The inlet temperature of the hot gas is assumed as 1750 ºK (1477 ºC) based on energy balance and efficiency of the first-generation combustor and the inlet temperature of the fluid/water is 300 ºK (27 ºC). Also, energy losses through the combustor/heat exchanger wall to the surroundings are ignored.
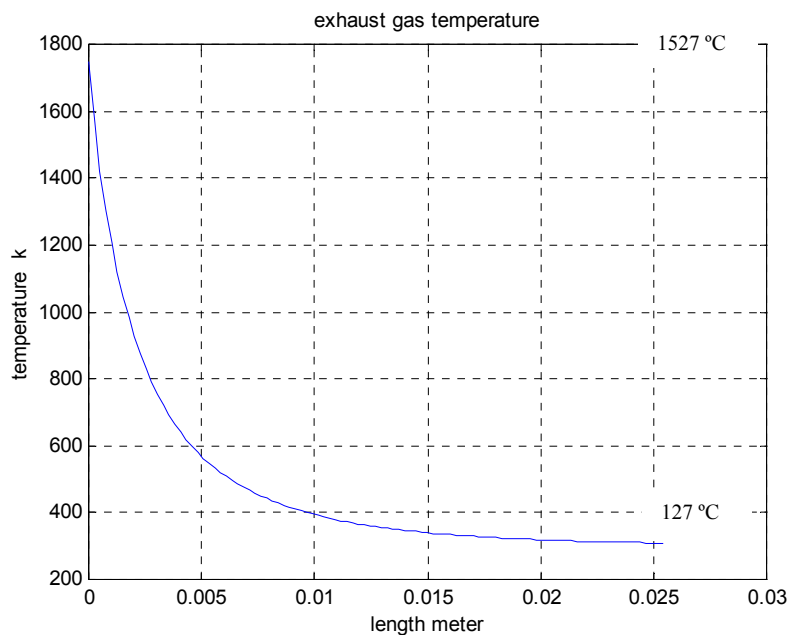
Figure 54. Exhaust gas temperature along the combustor channel.
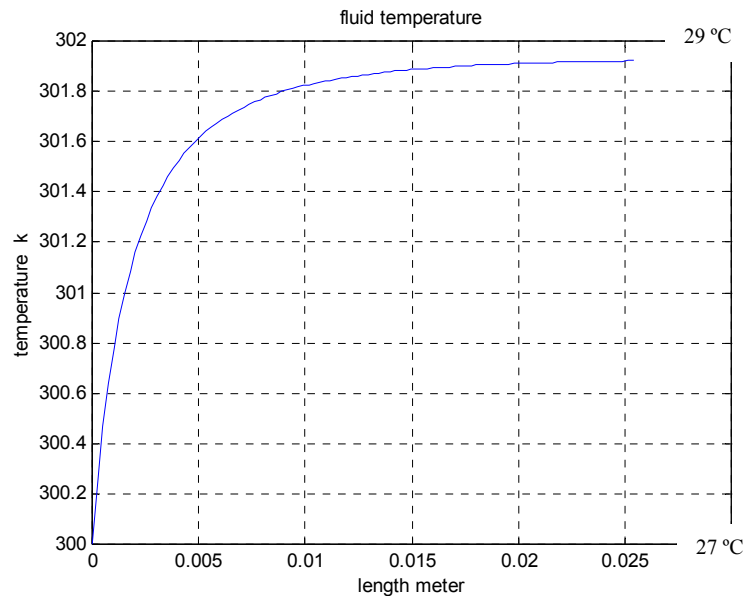
Figure 55. Fluid temperature along the heat exchanger channel.

The cooling of the gas is rapid with a significant temperature drop within 1.5 cm. The energy from the hot gas can be transferred efficiently to the cold fluid through the wall. The temperature increment of the fluid in Figure 55 is due to only right side of channel of the combustor/heat exchanger, thus the total temperature change is around 3.9 ºC.

The following plots show the main design parameter variations with channel widths (W_2 in Figure 52). The Reynolds number, friction factor and pressure loss of the exhaust gas are based on air properties at 500 ºK (227 ºC), which is the average temperature along the combustor channel. The density and viscosity of the exhaust gas are almost similar to those of air. The fuel was propane and there was 20% excess air. The heat transfer coefficient of the exhaust gas was taken as the mean value along the channel length.

Figure 56 shows friction factor and pressure loss with width (spacing) of channel. The pressure loss increased as channel width decreased.
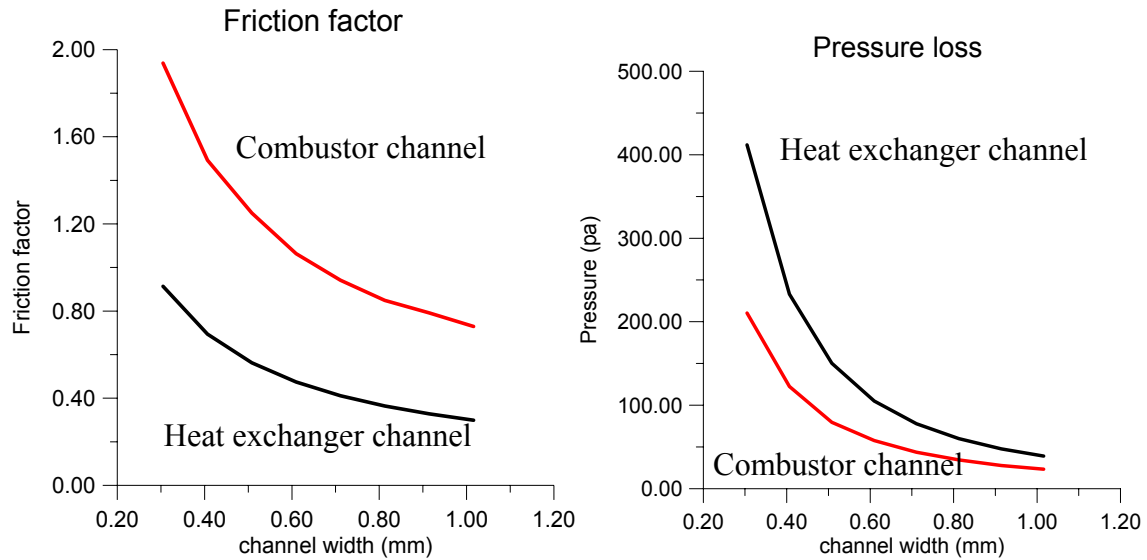
Figure 56. Friction factor and pressure losses.

The heat transfer coefficients for the combustor-side channels and heat exchanger-side channels, as shown in Figure 57, varied from 130 W/m^2 °K to 310 W/m^2 °K and from 8000 W/m^2 °K to 2300 W/m^2 °K, depending on the channel width. The heat transfer coefficient also decreased as the channel width increased, as in the pressure loss plot.
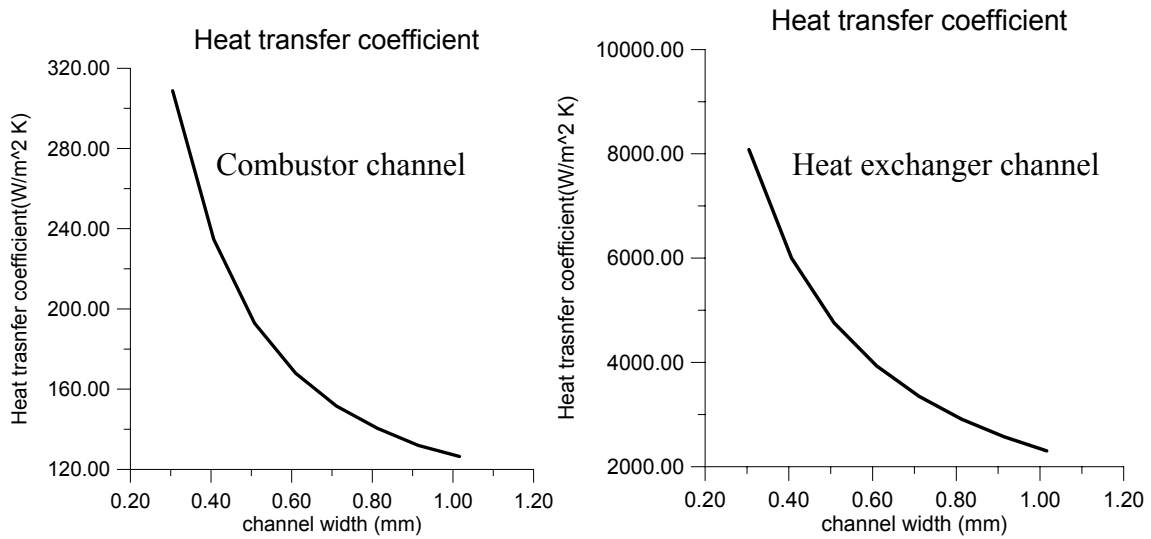
Figure 57. Heat transfer coefficients.

The Reynolds number of fluid and gas ranged from 200 to 30, which is within laminar flow conditions. The Reynolds number is proportional to the channel width as shown in Figure 58.
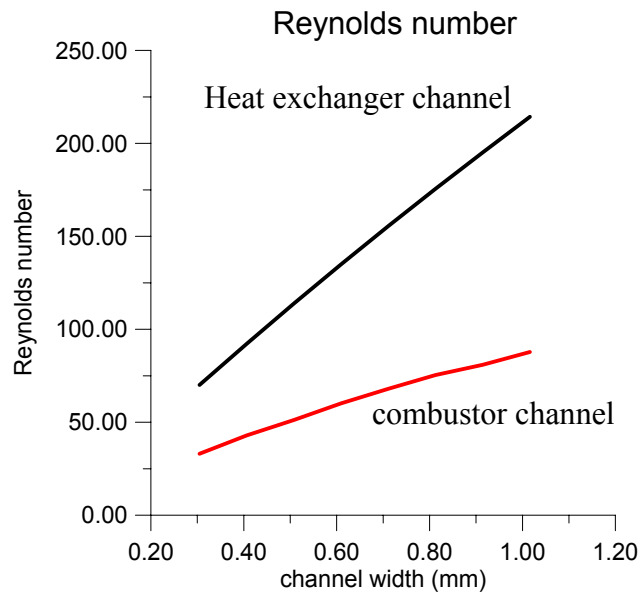
Figure 58. Reynolds number.

The exhaust gas temperature profile, as shown in Figure 59, drops more sharply as the width of the channel decreases.
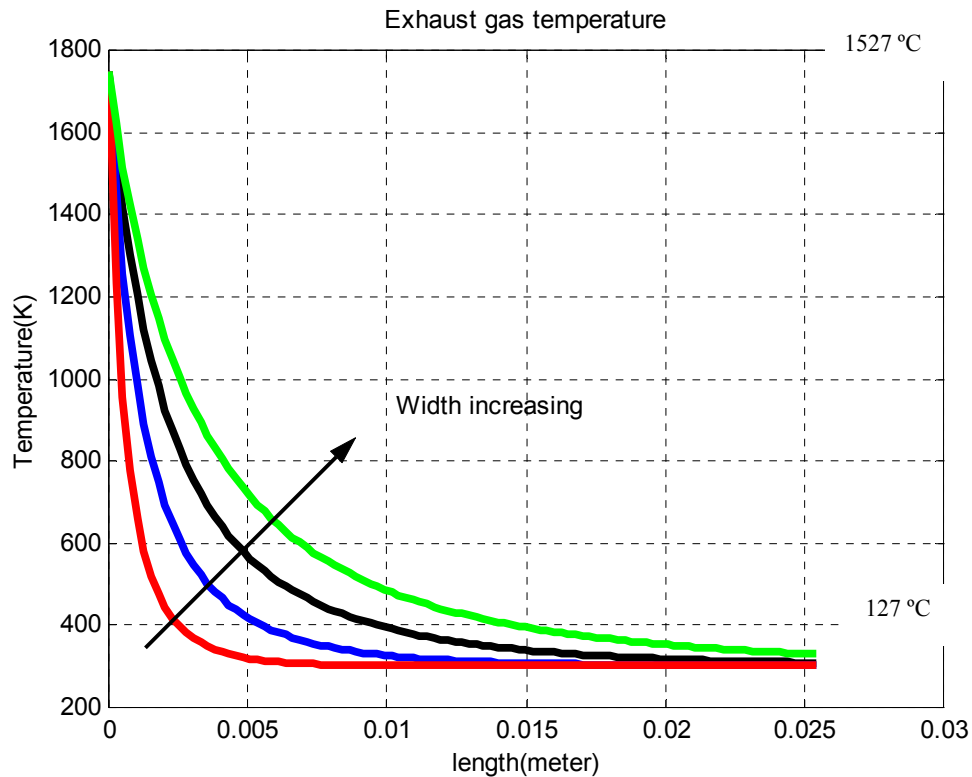
Figure 59. Temperature profiles with channel widths.

6.3.2. The second-generation multi-channel combustor/heat exchanger

The size of the second-generation combustor/heat exchanger is 81.3 mm x 76.2 mm (3.2 inch x 3.0 inch), which is about ¼ of the first combustor/heat exchanger. The channel size of the heat exchanger is 7.6 mm x 0.81 mm (spacing: 0.81 mm=0.032 inch). The size of the heat exchanger was determined so that it would hold the amount of hot fluid corresponding to one cycle of actuation, which is 1 m/sec x half size of the heat

exchanger (81.3 mm x 76.2 mm x ½). To meet this requirement, the height of the heat exchanger channel was set at 7.6 mm (0.3 inch). Also, we can decrease the channel spacing and thickness; this would increase the heat transfer coefficient at the expense of the pressure loss and cost of machining. For a given length of the combustor channel, the advantage of this high heat transfer rate is most important at the initial part of the channel. This is the case since heat transfer occurs mostly at the initial part of the channel, as shown in Figure 54, while in other regions, there is no heat transfer from the hot gas to the fluid [22].

From the simple steady-state heat transfer analysis, the length of the channels on the combustor side can be determined. Most of the heat transfer occurs to less than 1.5 cm area along the length. The channel size on the combustor side is 2.5 mm x 0.81 mm x 25 mm. The total number of channels is 39.

Figure 60 shows the structure of the multi-channel combustor/heat exchanger, which is composed of top plate, inlet and outlet of fluid, multiple channels of combustor/heat exchanger, bottom plate, sintered porous metal sheet (2 micrometer grade size) and mixing chamber for premixed gases. The ceramic fiber, as shown Figure 61 is utilized to achieve sealing between the mixing chamber and the bottom plate and to allow the thermal expansion of the porous metal plate. There is a thermocouple and an igintor inside the combustion chamber in order to ignite the flame and to monitor the temperature of the combustion chamber, which is the rectangular slot of the bottom plate.
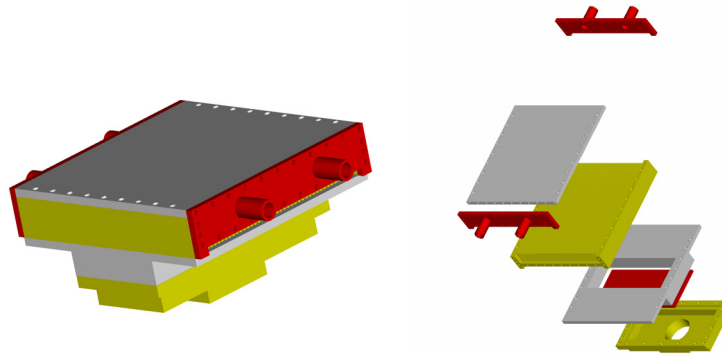
Figure 60. 3D drawing of combustor/heat exchanger (Pro/Engineer).

81.3 mm
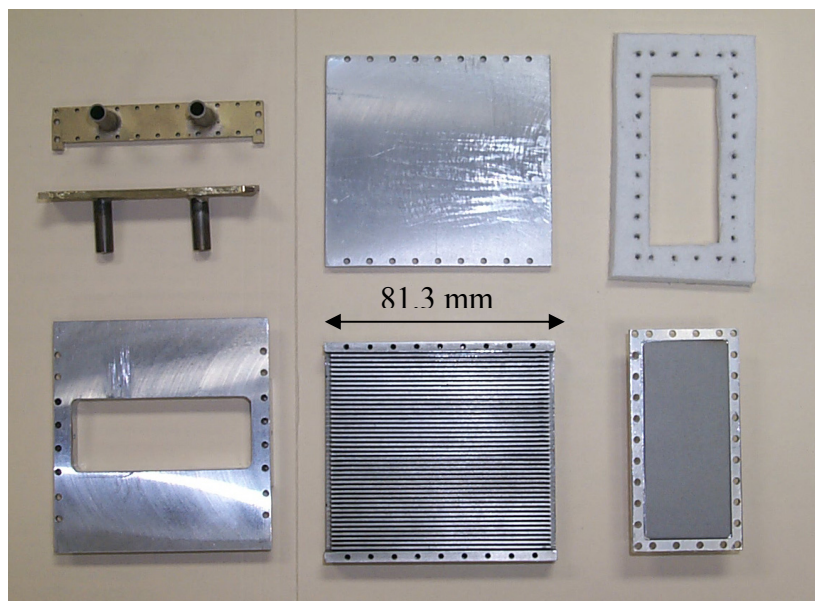
Figure 61. Components of combustor/heat exchanger (second-generation prototype).
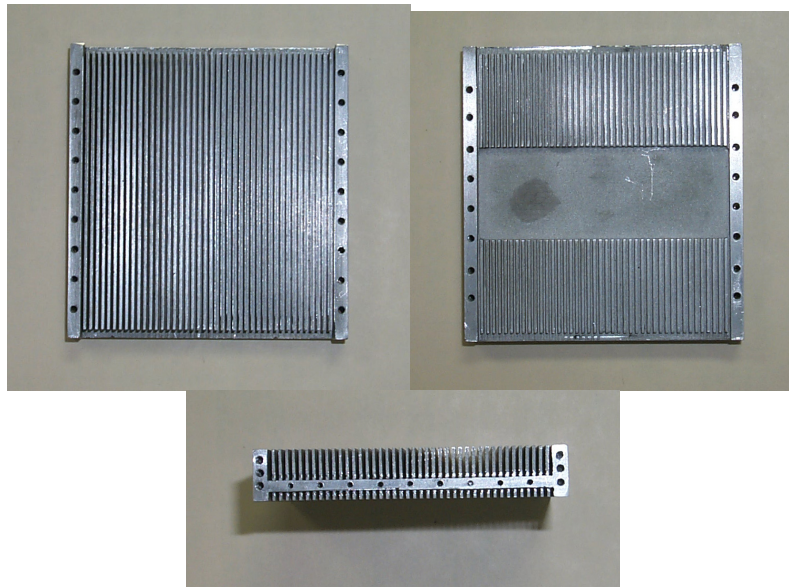
Figure 62. Multi-channel section of combustor/heat exchanger.

Figure 61 and Figure 62 show the actual components of the combustor/heat exchanger. Figure 62 shows the multi-channel sections of the combustor/heat exchanger machined by CNC using a slitting saw. Figure 63 and Figure 64 show the assembled combustor/heat exchanger, which is sealed by screws and high temperature RTV.
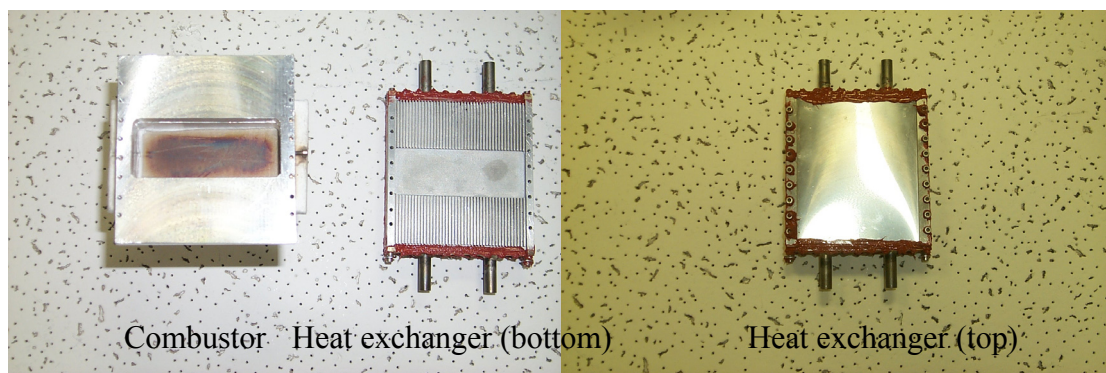
Figure 63. Combustion chamber and heat exchanger.
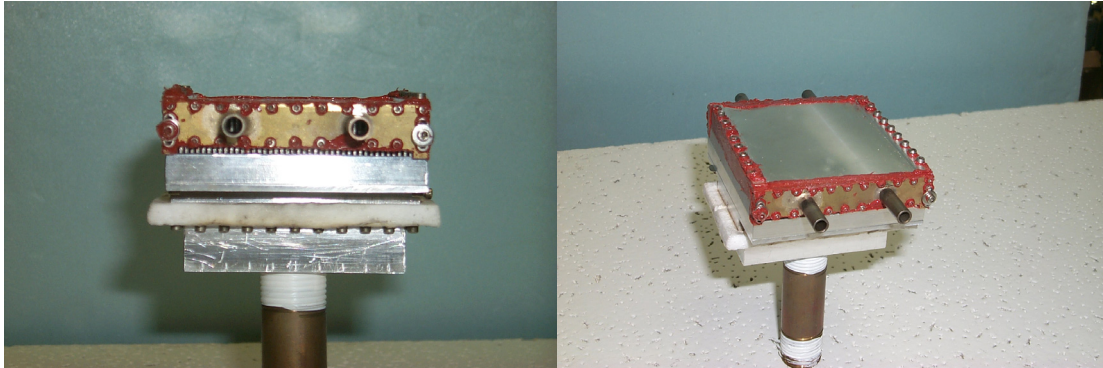
Figure 64. Assembled combustor/heat exchanger.

6.3.2.1 Experimental setup

The experimental setup, as shown in Figure 65 is the same as that of the first-generation combustor/heat exchanger. The flow rate of the air, fuel and water are measured by rotameters. The volume flow rate of the second-generation combustor/heat exchanger is smaller than that of the first-generation one, thus a small gear pump was used to control the flow rate easily.

Figure 65 shows the actuator test setup for the second-generation combustor/heat exchanger. Figure 66 shows the main nozzles used to supply fuel and air into the combustion chamber through ducts. Also the thermocouple and spark generator/ignitor were inserted into the combustion chamber.
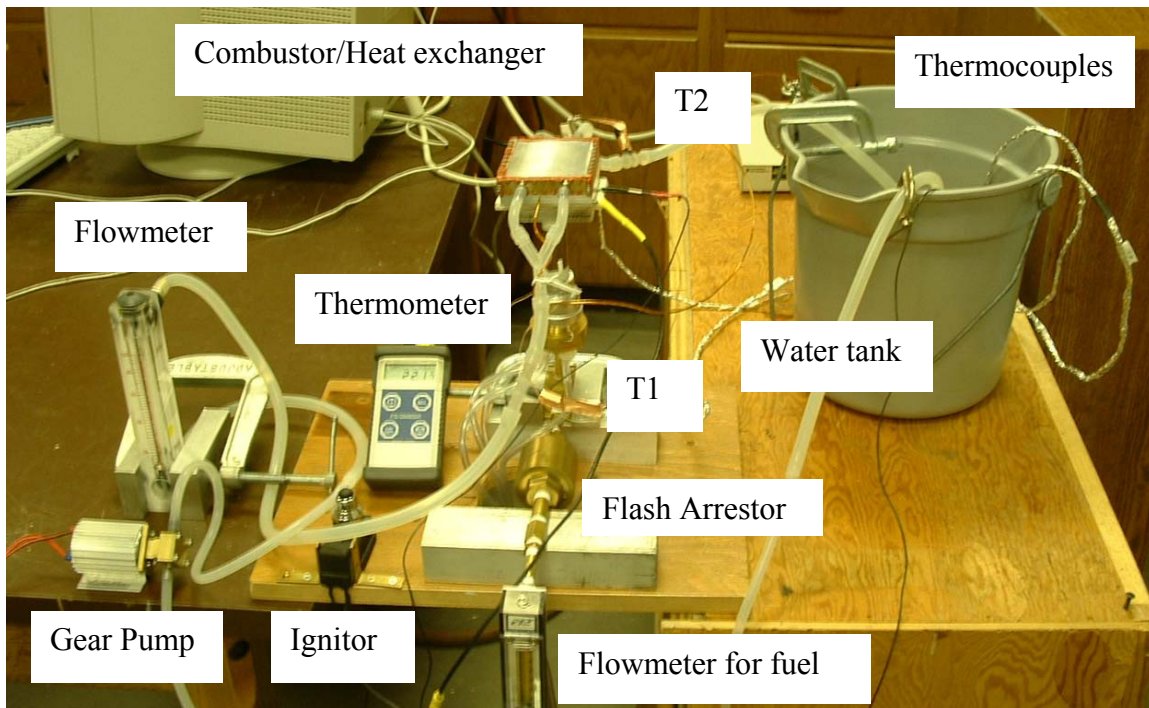
Figure 65. Experimental setup.
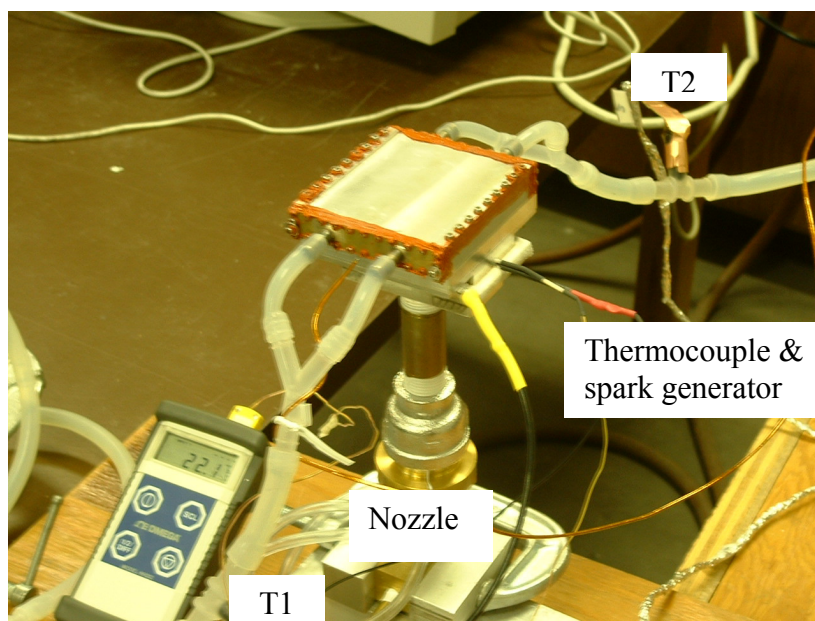
Figure 66. Nozzles, thermocouple and spark generator/ignitor.

6.3.2.2. Performance test of the second-generation combustor/heat exchanger

4 liters of distilled water was utilized as the working fluid for the performance test, as in the tests of the first-generation combustor/heat exchanger. The performance tests were conducted under the following conditions. The water flow rate was set at 0.5 GPM (1.89 l/min). The fuel flow rate was also set at 0.45 l/min (around 0.7 KW) and the airflow rate was set at 12.7 l/min.
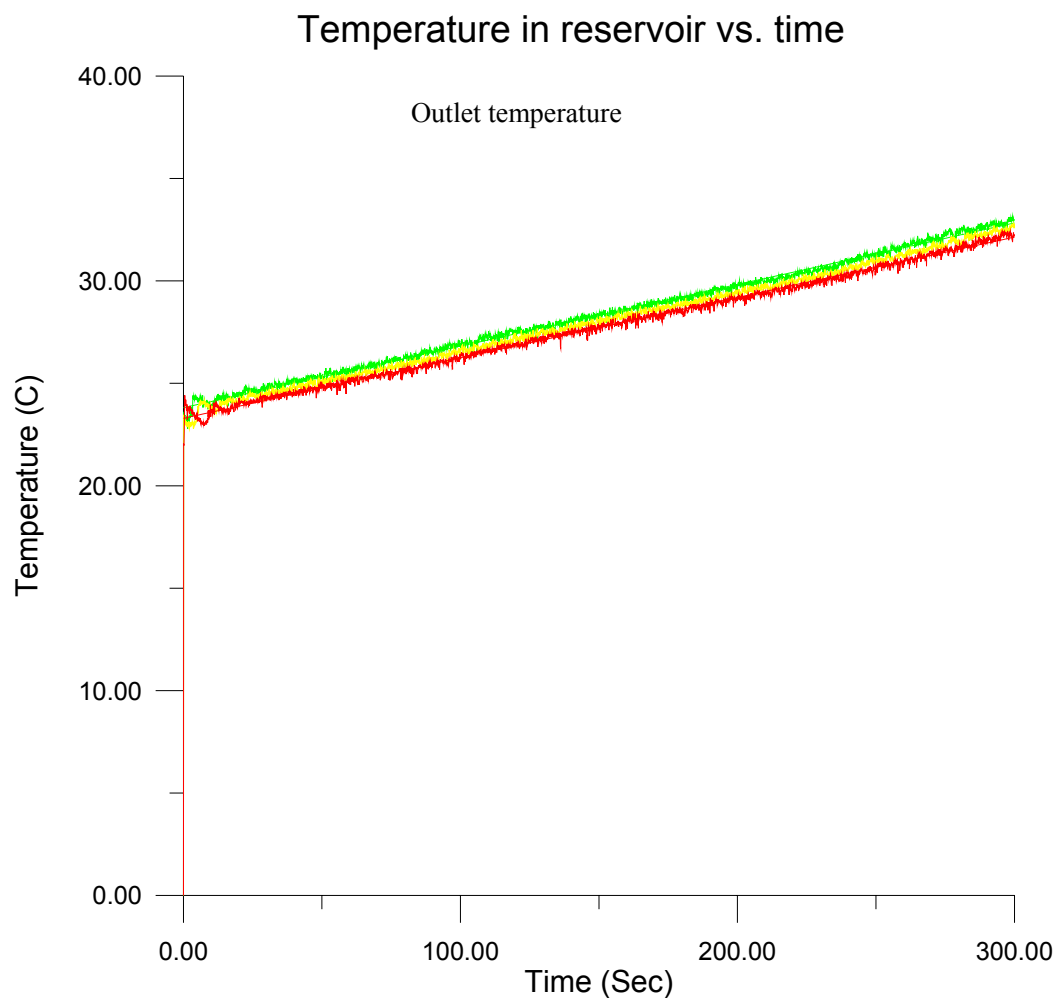
Figure 67. Water temperature increment by combustor/heat exchanger (1.89 l/min)

The equation of the curve in Figure 67 is Temp = 0.029916 x time + 23.5025 °C. The total temperature increment during 300 sec was 8.975 °C (0.029916 x 300 sec). The obtained power of the working fluid was around 500 Watts, thus the efficiency of the combustor/heat exchanger was around 70 %, which is the same as the value of the first-generation combustor/heat exchanger.

The output of the combustor/heat exchanger is very consistent at the same conditions. Figure 68 shows two test results under the same conditions. They correspond to flow rates under 21 ml/sec.
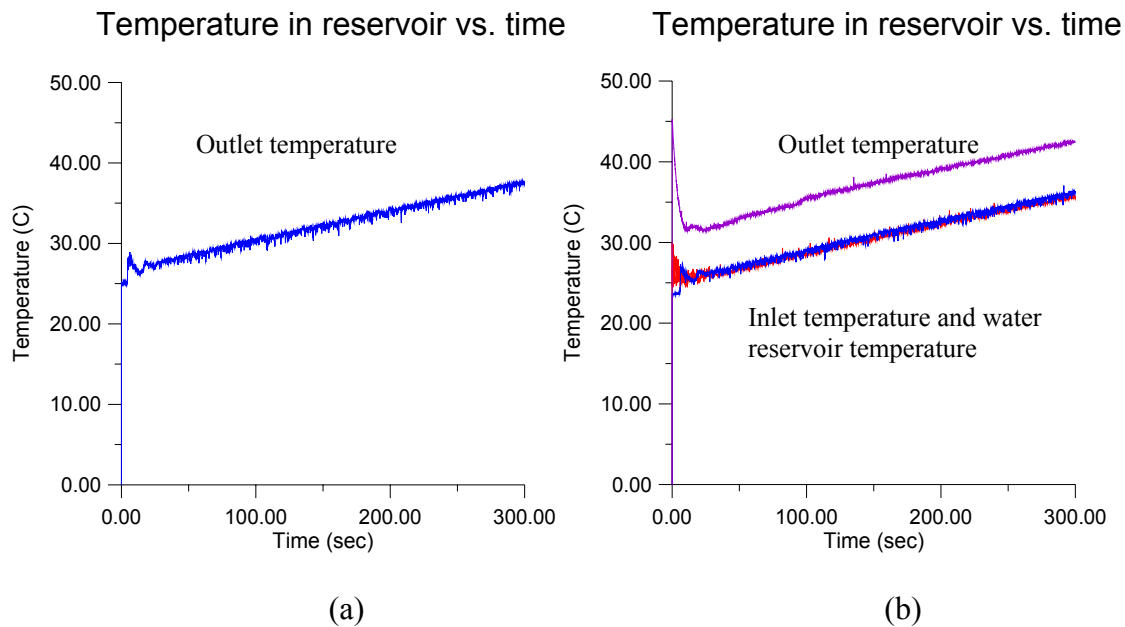
Figure 68. Water temperature increment by combustor/heat exchanger.

The obtained energy/power passing through the heat exchanger was 611 Watts as shown in Figure 68-(a) and 622 Watts as shown in Figure 68-(b). Figure 69 shows the highest power which was obtained from the tests. This power was 807 Watts. The slope was 0.0483 °K/sec and the total temperature increment was 14.5 °C/sec at 30 GPH flow rate.
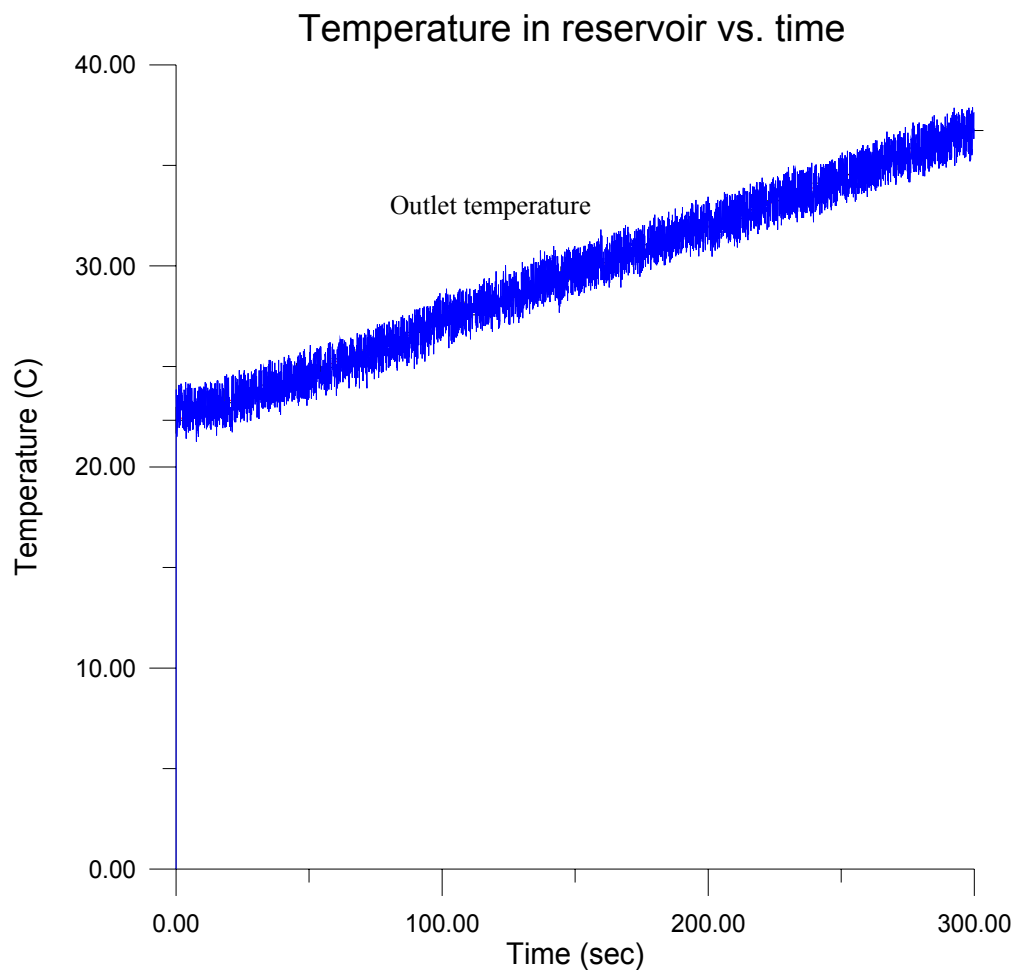
Figure 69. Water temperature increment by combustor/heat exchanger (807 Watts).

Figure 70 shows inlet and outlet temperature of the fluid during 360 seconds. The numerical analysis predicted 3.9 º C increment, which is similar value to the result of the test shown in Figure 70. The test was conducted under similar conditions for the numerical analysis, i.e. 700 Watts of input energy and 0.5 GPM (1.89 l/min) flow rate. From the comparison between test result and the numerical calculations, the simple thermal resistance model shows good agreement with the tests conducted.
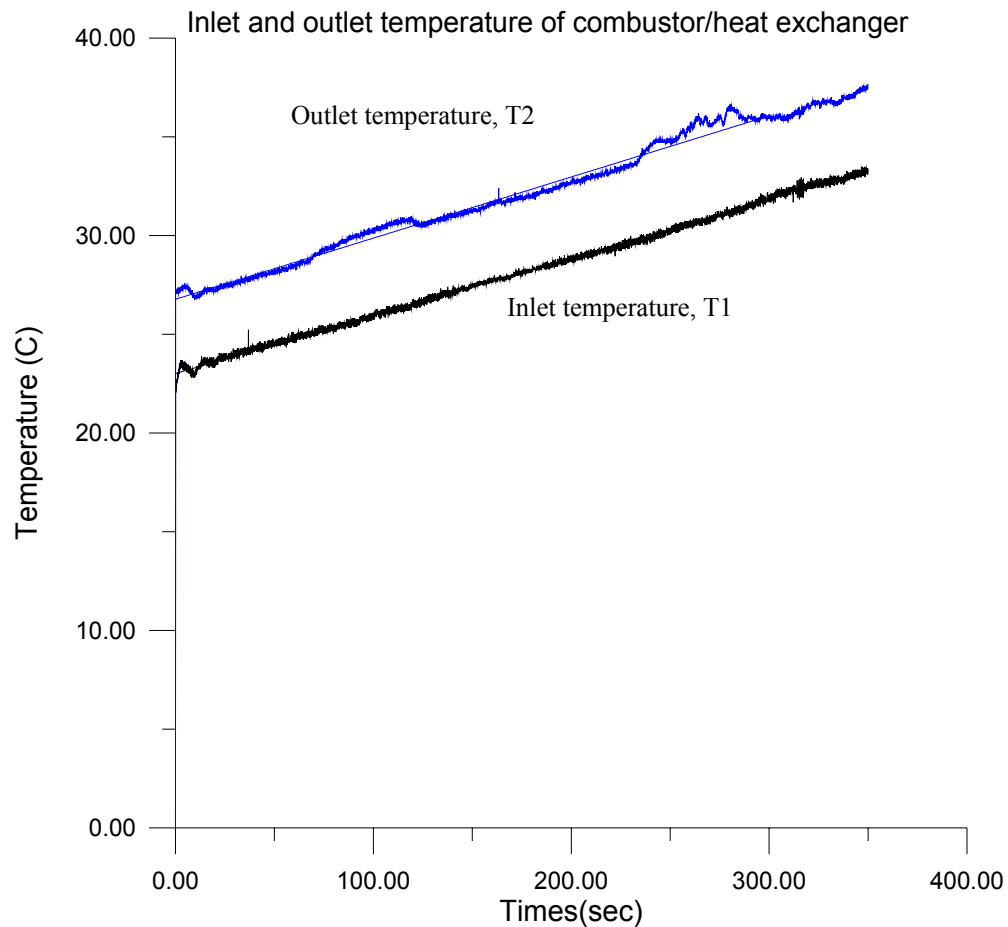
Figure 70. Inlet and outlet water temperature of the combustor/heat exchanger.

6.4. Conclusions

The size of the second-generation combustor/heat exchanger is 81.3 mm x 76.2 mm x 17.8 mm, which is about ¼ of the first-generation combustor/heat exchanger. The channel size of the heat exchanger is 7.6 mm x 0.81 mm (spacing: 0.81 mm), while the channel size of the combustor is 2.5 mm x 0.81 mm. The total number of channels is 39. The actuator power output ranged up to 800 Watts. The efficiency of the multi-channel combustor/heat exchanger was around 70 %, which is much higher than that of the propane burner. The multi-channel combustor/heat exchanger achieved high compactness, lightness and high efficiency, which can make the SMA actuator system more compact. The flame was contained in the combustion chamber and the temperature of the exit gas from the channels of the combustor was around 340 ºK (67 ºC), which much lower than the flame temperature (more than 1750 ºK=1477 ºC), thus it will be possible to make a portable actuator system regardless of the high temperature of the flame. The numerical analysis was useful in the design stage of the multi-channel combustor/heat exchanger.

CHAPTER VII

MICRO-TUBE HEAT EXCHANGER

7. Introduction of micro-tube heat exchanger

A heat exchanger is needed in the actuator system to dissipate the energy from the water used to cool the SMA strip. Available commercial products would not support system requirements, which required the heat exchanger to be small and compact and have relatively high heat transfer rate. Generally, the performance of a heat exchanger has been improved by employing extended heat transfer surfaces, such as louvered fins and offset-fins in order to increase the heat transfer rate [46]. But the commercial heat exchanger performance seems to be saturated due to limitation on the extended surface area and due to manufacturing costs [46, 47]. To overcome the limitation of the extended surface area, the micro-channel approach (micro-channel sizes ranging from 100 μm to 1 mm) has been utilized, even though it induces steep pressure gradient across the channel. Micro technology has been applied to improve the heat transfer rate of cross flow heat exchangers [23, 46], which have light weight and compactness. Micro-channel cross flow heat exchangers [23] operating under laminar flow conditions were developed by a manufacturing process that combines LIGA (an acronym from German words for lithography, electroplating and molding) micromachining, traditional precision machining, and bonding. The heat transfer per volume of the micro-channel cross flow heat exchanger is better than that of innovative car radiators [23]. Also heat exchangers

based on micro tubes have been developed and manufactured that operate under laminar flow conditions, even up to high levels of power and flow [46, 47].

The heat transfer of micro-channel or micro-tube exchangers can be increased by reducing the length scale L(D$_h$), for a given Nusselt number $\left(Nu = h \cdot L / k \right)$. Thus the performance of a laminar operating heat exchanger is increased by reducing the hydraulic diameter of its flow passage even though the Nusselt number is small compared to that of turbulent flow. By using bare micro copper tubes, the performance can be increased and the core volume of the heat exchanger can be decreased. Reference [46] presents optimal design method of heat exchangers and their performances, by using bare micro copper tubes. Due to the ease in machining and fabrication and due to its high heat transfer rate and high operating pressure capabilities, the micro-copper tube heat exchanger was selected for the SMA actuator system. The heat exchanger was composed of 561 copper tubes (inner diameter = 0.7 mm, outer diameter =0.95 mm, length=140 mm), headers, inlet and outlet fittings and a fan, which induces forced air flow around the copper tube array.

7.1. Design procedure

The core volume, tube dimensions, temperatures of working fluids and heat exchange rate were determined first by heat transfer analysis.

7.1.1. Heat transfer inside the tube

The flow inside the tube is assumed to be hydrodynamically and thermally fully developed flow due to tube's small diameter compared to its over all length [46]. Since the Reynolds number of flow is less than 2300, the duct flow is assumed to be laminar flow having isothermal wall boundary conditions. Thus the Nusselt number of the duct flow can be defined as,

$$Nu_i = \frac{h_i \cdot d_i}{k_i} = 3.66 \tag{28}$$

Where h_i, d_i and k_i are the heat transfer coefficient of the analytical solution, the copper-tube inner diameter and the fluid(water) thermal conductivity.

7.1.2. Heat transfer across tube bank

An aligned-tube-bank configuration, as shown in Figure 71, was selected due to its higher heat transfer rate at same pumping power compared to the staggered-tube-bank configuration. The Nusselt number of the tube bank is estimated by the following correlation equations given by Mills [48]:

The velocity u_{max} [48] is the maximum velocity in the aligned tube bank. For an aligned bank, the maximum velocity occurs between adjacent tubes of a transverse row.

$$\frac{u_{max}}{u_o} = \frac{S_T}{S_T - d_o} \tag{29}$$

Where $S_T = P_T \cdot d_o$ and $S_L = P_L \cdot d_o$.
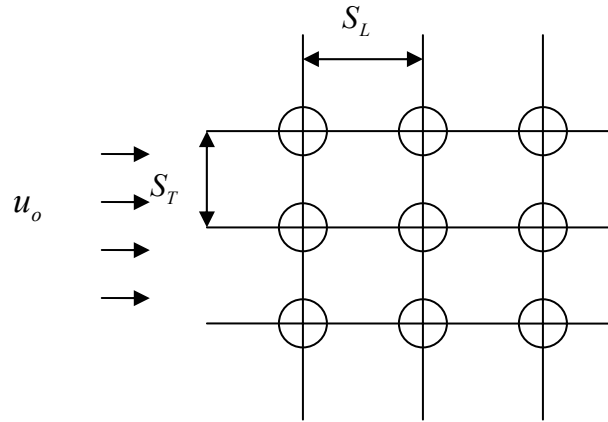
Figure 71. Tube bank.

The average velocity u_{avg} [48] in the space between two adjacent tubes is defined by the relation s;

$$\frac{u_{avg}}{u_o} = \frac{S_T}{S_T - (\pi/4) \cdot d_o}$$

(30)

Where u_o is the velocity of the fluid in the empty cross section of tube bank configuration as shown in Figure 71.

The Nusselt number for a tube bank having 10 or more rows is defined by [48];

$$Nu_o = \frac{h_o d_o}{k_o} = \Phi \cdot \left(0.3 + \frac{0.62 \cdot Re_D^{1/2} \cdot Pr^{1/3}}{\left[1 + (0.4/Pr)^{2/3} \right]^{1/4}} \right)$$

(31)

Where $\Phi_{aligned} = 1 + \frac{0.7}{\psi^{1.5}} \cdot \frac{S_L/S_T - 0.3}{(S_L/S_T + 0.7)^2}$ and $\psi = 1 - \frac{\pi}{4 \cdot P_T}$, and h_o, d_o, k_o are the heat transfer coefficient, tube outer diameter and fluid (air) thermal conductivity respectively.

The overall heat transfer coefficient U can be calculated by the following equations;

$$\frac{1}{U} = \frac{d_o}{d_i} \cdot \frac{1}{h_i} + \frac{1}{h_o} + \frac{r_o}{k} \cdot \ln\left(\frac{d_o}{d_i}\right)$$ (32)

Where k is the thermal conductivity of pure copper (k=401.0 W/m K).

The total exchange energy (Q) can be obtained by using the effectiveness-Ntu method [44]. For a cross flow heat exchanger with two fluid streams unmixed, then Q is obtained by using Q_{max}, effectiveness(ε), $C_{min} = \dot{m}_a \cdot C_{p,a}$, and ΔT_{inlet}.

$$Q_{max} = C_{min} \cdot (T_{w,inlet} - T_{a,inlet}) = C_{min} \cdot \Delta T_{inlet}$$ (33)

Effectiveness, i.e. the ratio of the actual heat transfer rate to the maximum possible heat transfer rate, is defined [44] as,

$$\varepsilon = 1 - e^{\left[\frac{1}{Cr} \cdot Ntu^{0.22} \cdot \left[e^{(-Cr \cdot Ntu^{0.78})} - 1\right]\right]}$$ (34)

Thus Q is;

$$Q = \varepsilon \cdot C_{min} \cdot \Delta T_{inlet} = \left[1 - e^{\left[\frac{1}{Cr} \cdot Ntu^{0.22} \cdot \left[e^{(-Cr \cdot Ntu^{0.78})} - 1\right]\right]}\right] \cdot C_{min} \cdot \Delta T_{inlet}$$ (35)

Where ΔT_{inlet} is the inlet temperature difference of the two working fluids. The quantity Cr is the heat capacity ratio defined as $Cr=C_{min}/C_{max}$, where C_{min} and C_{max} are the large and small capacity values of two working fluids. Ntu (number of transfer unit) is defined as $Ntu=U \cdot A/C_{min}$, where U is the overall heat transfer coefficient defined above and A is the heat exchange area.

7.1.3. Pressure loss and pump power

7.1.3.1. Inside tubes

The core pressure drop of the flow inside the copper tube can be calculated such as [46];

$$\Delta P_{core} = \frac{\rho u_m^2}{2} \cdot \left(K_{inlet} + K_{exit} + f_w \cdot \frac{1}{di} \right) \tag{36}$$

Where f_w is the friction factor ($f_w=64/Re$ for fully developed laminar flow) and K_{inlet} (0.5) and K_{exit} (1.0) are the core inlet and exit pressure loss coefficients. The total pressure droop across the heat exchanger is assumed to be three times the core pressure drop ($\Delta P_i = 3 \cdot \Delta P_{core}$) [46];

The pump power for the fluid can be obtained from the pressure loss of the inside tubes.

$$W_p = \frac{\dot{m}_w \cdot \Delta P_i}{\rho_w} \tag{37}$$

Where $\dot{m}_w$, ρ_w are the mass flow rate and water density, respectively

7.1.3.2. Across tube bank

Zhukauskus [49] recommends that the pressure drop in a tube bank be calculated as;

$$\Delta P_o = N_L \cdot \chi \cdot \left[\frac{\rho \cdot u_{max}^2}{2} \right] \cdot f_a \tag{38}$$

Where $\chi = 1$ for a square aligned configuration and for an equilateral-triangle staggered configuration [49]. The friction factor f_a and the correction factor χ are given [49].

The pump power driving the external air flow can be obtained as

$$W_p = \frac{\dot{m}_a \cdot \Delta P_o}{\rho_a} \tag{39}$$

Where $\dot{m}_a$ and ρ_a, are the air mass flow rate and air density, respectively.

7.2. Numerical calculation

The Q was set around 350 Watt or higher, which would be enough to prevent the water temperature of the cooling circuit from increasing more than the martensite finish temperature at given actuation conditions. The width, thickness, pressure losses and pumping power were calculated based on the following main parameters as shown at Table 4. These parameters are defined by tube geometry, power requirements, and available tube bank heat transfer data.

Table 5 shows the results of the numerical calculations. The total heat exchange rate was 356.9 Watts and 561 tubes (11 x 51) were used to construct the tube bank array. The core size of heat exchanger was 140 mm x 100 mm x 20 mm.

Table 4. Main parameters of heat exchanger.

Q	$\dot{m}_w$	u_o	d_o	d_i	S_T	S_L	l	$T_{a,inlet}$	$T_{w,inlet}$
Watts	l/sec	m/sec	mm	mm	mm	mm	mm	°C	°C
356.9	0.0253	1	0.95	0.7	2	2	140	21	45

Table 5. The results of the numerical calculations.

ΔP_i	ΔP_o	Nu_o	h_i	h_o	f_a	f_w	w	t	u_{max}
Pa	Pa		$W/m^2 {}^\circ K$	$W/m^2 {}^\circ K$			mm	mm	m/sec
656	15.6	7.56	3332	190.5	0.6	0.465	100	20	2.0

Figure 72 shows the performance of the heat exchanger as function of the inlet velocity (u_o) of the air and the inlet temperature of water.
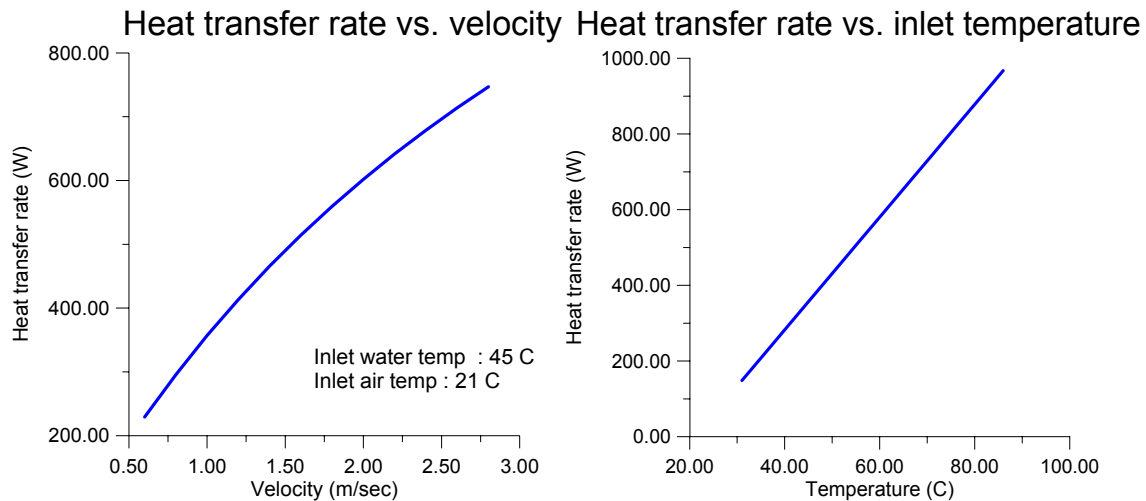
Figure 72. Q vs. u_o (left) and Q vs. inlet temperature of water (right).

7.3. Micro-tube heat exchanger

The micro-tube heat exchanger is composed of inlet and outlet caps, inlet and outlet fittings, multi-hole tube headers and copper micro-tubes. The holes of the brass header are machined by CNC drilling. Super bonder is applied to hold together tubes and headers. A 120 mm x 120 mm fan is attached to the heat exchanger in order to induce air

flow between the tubes of the bank in order to increase the heat transfer rate. RTV (high temperature silicon) and screws are utilized to seal the caps and headers of the heat exchanger. Figure 73 shows the assembled the micro-tube heat exchanger and Figure 74 shows the micro tubes with a header. Figure 75 and Figure 76 show the components of the micro-tube heat exchanger.
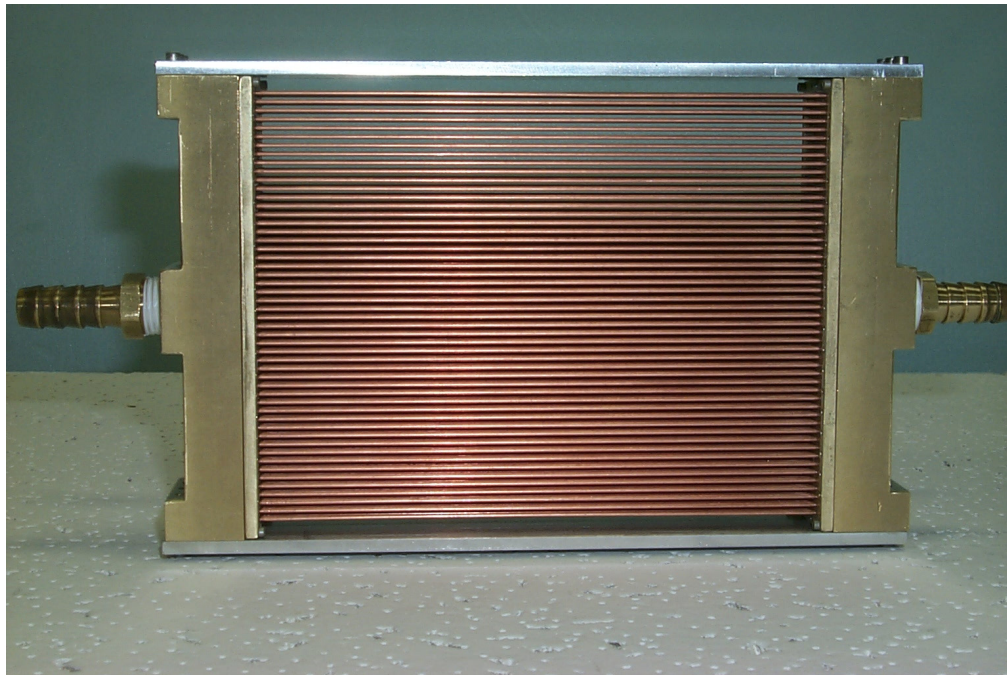
Figure 73. Assembled micro-tube heat exchanger.
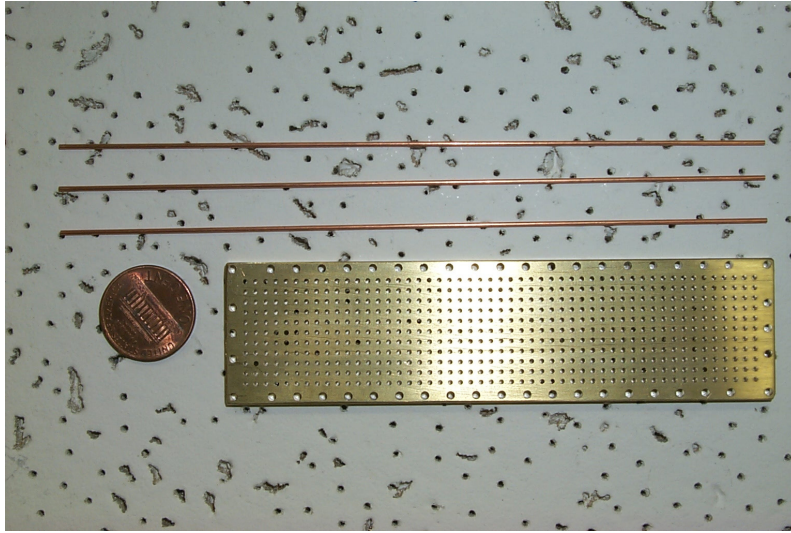
Figure 74. Micro tubes (outside diameter = 0.95 mm, inner diameter = 0.7 mm) and

header.
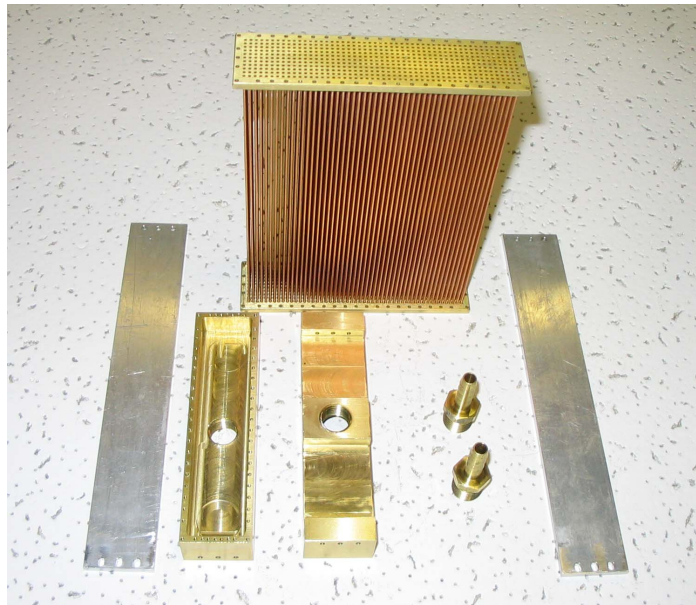
Figure 75. Disassembled heat exchanger.
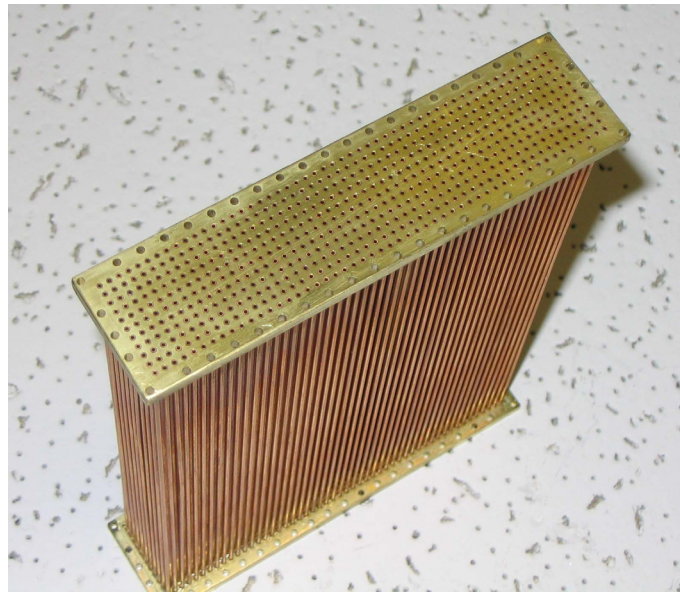
Figure 76. Tubes (number of tubes: 561) and headers.

7.3.1. Experimental setup
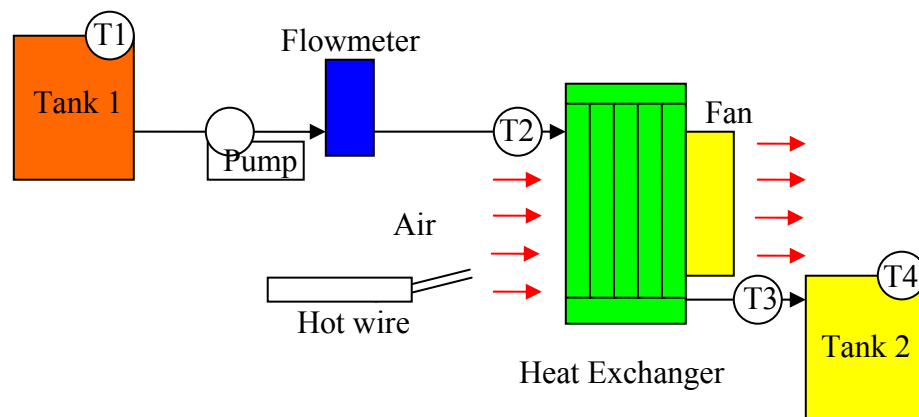
Figure 77. Performance test setup.

Figure 77 shows the experimental setup for the micro-tube heat exchanger. It is composed of water tanks, flowmeter, pump, heat exchanger with fan, and

thermocouples. Tank1 contains 10 liters of distilled water maintained at 45 °C, which is

24°C higher than the surroundings. The water of tank 1 is drained by a gear pump at

around 25.2 ml/sec (0.4 GPM). The flow rate of the water is set by a flowmeter and a

control valve. K-type thermocouples are used to monitor and record the temperatures of

the water at each location. After 1 or 2 minutes, the inlet and outlet temperature of the

heat exchanger reach equilibrium, or steady state. Thus the heat transfer rate to the

surroundings can be obtained from temperatures T2 and T3. The temperature difference

between T2 and T3 value represents the performance of the micro tube heat exchanger.

A hot wire is utilized to measure the velocity of air entering the tube bank. Figure 78

presents the calibration curve of the hot wire. The temperature data is obtained and

recorded by a Lab-Windows program and a NI (National Instrument, AT-MIO-16XE-

50) board.
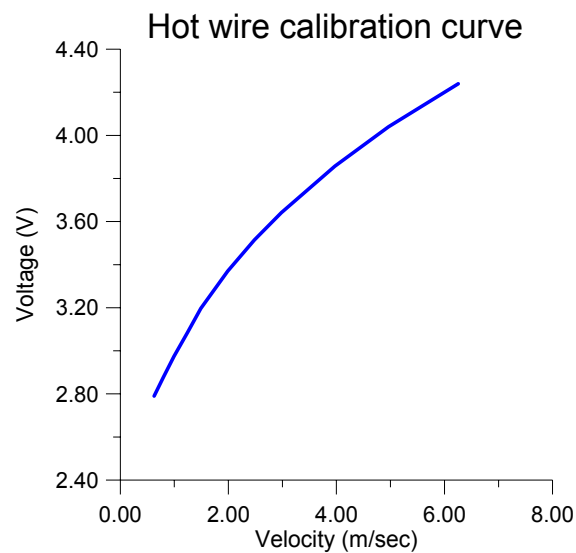
Figure 78. Hot wire calibration curve (voltage vs. velocity).

7.3.2. Test result of micro tube heat exchanger

The test was conducted for 5 minutes (300 seconds) after reaching steady state by pre-operating the heat exchanger. The inlet air velocity(u_o) to the heat exchanger was around 1 m/sec. Figure 79 shows the inlet and the outlet temperatures of the heat exchanger with time. The temperatures of the water tanks were not constant during the test due to the energy losses to the surrounding through the tank wall. There was no leakage at all, even under high operating pressure during the test.
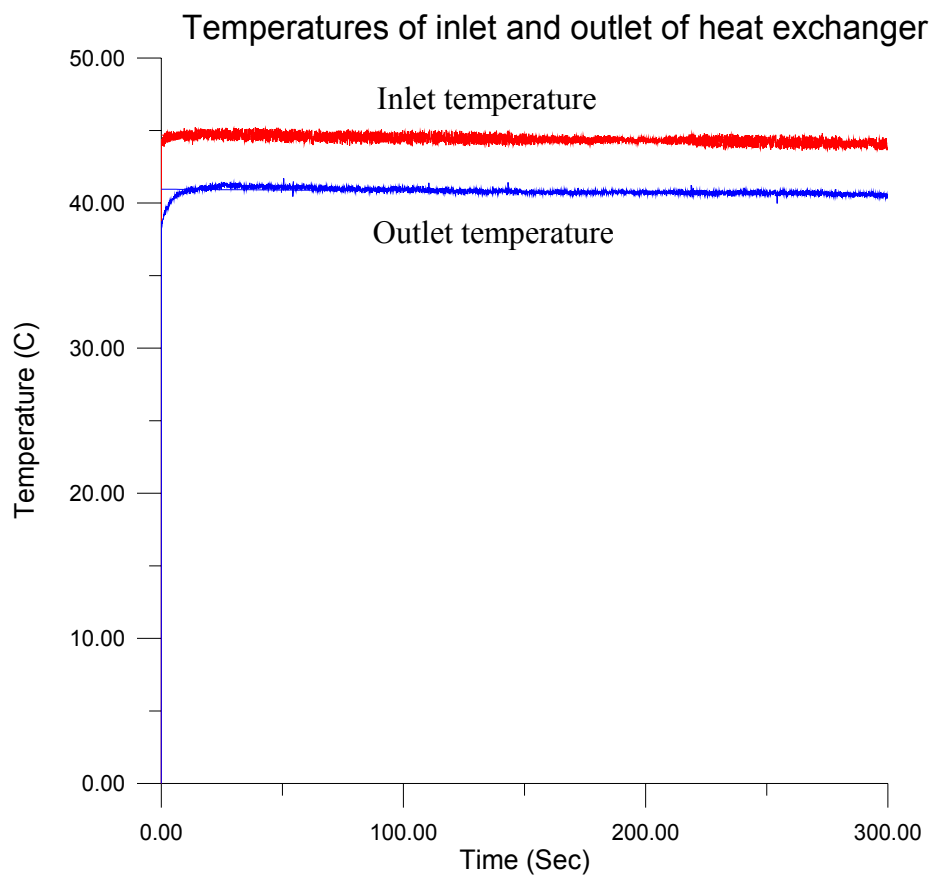
Figure 79. Inlet and outlet temperature variation (24GPH).

From the temperature curves in Figure 79, the total heat transfer rate can be obtained. The temperature drop across the heat exchanger was around 3.5655 °C, from which the performance of the heat exchanger is obtained. The output power of the heat exchanger to the surroundings by forced convection heat transfer is;

$$Q_1 = 3.5655(°C) \cdot 4182(J/kg°K) \cdot 0.02498(kg/s) = 372.5 Watts$$

Other test results also showed similar heat transfer rates.

$$Q_2 = 3.6334(°C) \cdot 4182(J/kg°K) \cdot 0.02498(kg/\sec) = 379.6 Watts$$

$$Q_3 = 3.569(°C) \cdot 4182(J/kg°K) \cdot 0.02498(kg/s) = 372.8 Watts$$

The experimental results show that the heat transfer rates of the heat exchanger were around 370-380 Watts, which are similar value compared to the numerical result, i.e. 356.9 Watts.

7.3.3. Comparison with the commercial heat exchanger

A comparison is carried out by using a commercial heat exchanger for a desktop computer water-cooling system. A PC cooling radiator with a 59.2 l/min (125.5 CFM) fan is used as the heat exchanger for the comparison. It measures 152 mm x 178 mm x 5.1 mm (6 inch x 7 inch x 2 inch).
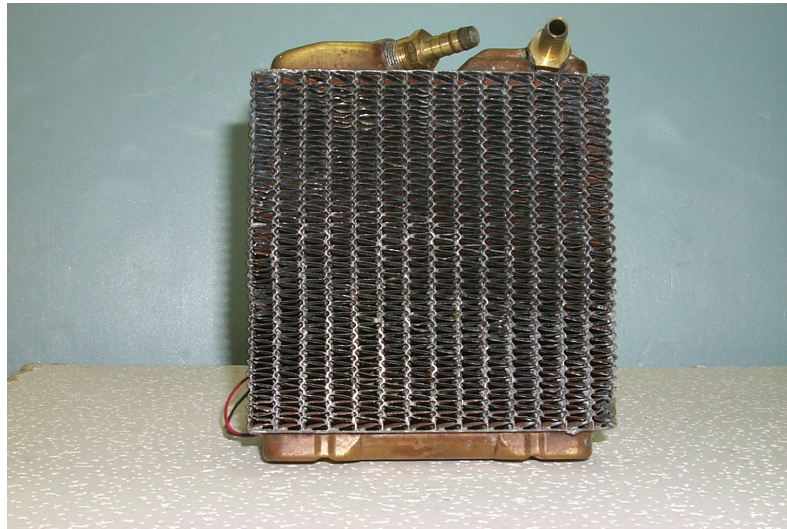
Figure 80. Commercial computer-water cooling radiator.

7.3.3.1. Test results

The commercial radiator as shown in Figure 80 and the micro-tube heat exchanger were tested under same experimental setup and same test conditions to compare the heat-transfer- rate per volume. Figure 81 shows the inlet and the outlet temperatures of the heat exchanger. The flow rate was 25.2 ml/sec (0.4 GPM) and the test lasted for 300 seconds. The heat transfer rate of this heat exchanger could be obtained from curves of the inlet and the outlet temperatures. The temperature drop across the heat exchanger was 4.25 °C, which is higher value than that of the micro-tube heat exchanger. Thus the Q is obtained by

$$Q_1 = 4.25(°C) \cdot 4182(J/kg°K) \cdot 0.02498(kg/s) = 444 Watts$$
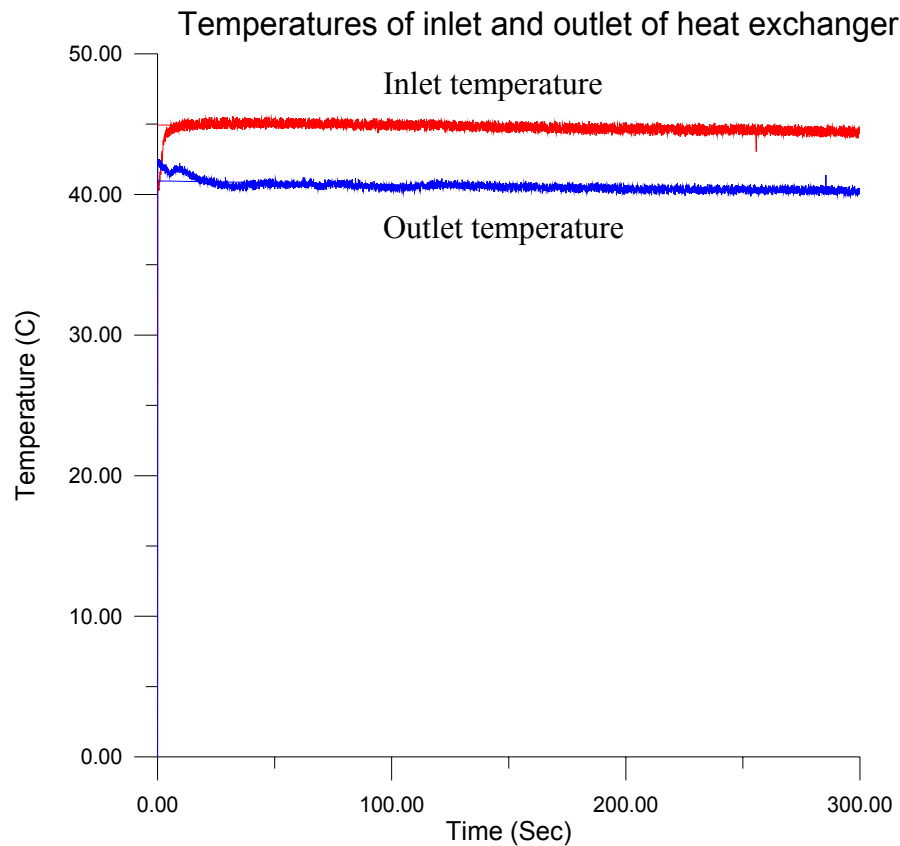
Figure 81. Performance of the commercial radiator.

The size of the commercial radiator is 152 mm x 178 mm x 5.1 mm, which is 2.4 times bigger than that of the micro-tube heat exchanger, the performance is just 1.2 times better.

7.4. Conclusions

The size of the micro-tube heat exchanger was 114.3 mm x 178 mm x 28 mm (Core size=100 mm x 140 mm x 20 mm). It dissipates around 380 Watts under a 24 °C inlet temperature difference between the two working fluids (air and water). The numerical calculations have shown good agreements with the results of the experimental testing.

The numerical calculations seem to underestimate the actual performance, hence more tests will be needed to correct the heat transfer coefficient of tube bank flow. The numerical analysis was useful in designing the heat exchanger, for example, in determining the volume and geometric parameters of the heat exchanger. Optimal designing [46] the tube array configuration and tube diameter is useful in increasing the compactness. Though the size of the commercial radiator, as shown in Figure 80, is 2.4 times bigger than that of the micro-tube heat exchanger, the performance is just 1.2 times better. Thus using the micro-tube heat exchanger has resulted in high compactness and high heat-transfer-rate per volume compared to commercial heat exchangers. The smaller diameter copper tubes produce higher heat-transfer-rate per volume ratio and higher compactness even though the pumping power increases. Also the inlet velocity has strong effects on the performance of the heat exchanger as shown by the numerical results presented in Figure 72.

CHAPTER VIII

THE FINAL FUEL-POWERED COMPACT SMA ACTUATOR SYSTEM

8. The final SMA actuator system

Figure 82 and Figure 83 show schematic and experimental setup of the final actuator system, which is based on the second-generation actuator system focusing on decreasing the mixing between the hot and cold water streams in order to increase the energy and power densities at the expense of simplicity of the system, as compared to the first-generation actuator system. A small size of SMA strip (2.5 mm x 0.9 mm in cross section) was used as the SMA element in order to increase the heat transfer rate compared to an SMA wire having the same cross section area. The SMA element is embedded in a rectangular channel with a rectangular piston, such as the second-generation actuator system.

The final actuator system is focused on miniaturization, compactness and lightness, thus the strip size is decreased compared to the second-generation actuator system. Micro/miniature technology was adopted in designing and fabricating its components such as the combustor and the heat exchanger in order to increase efficiency and compactness. The final actuator systems was made up of two gear pumps, four check valves, four solenoid valves, two bellows, a micro-tube heat exchanger (radiator) explained in Chapter VII, and a multi-channel combustor/heat exchanger explained in Chapter VI. A loading frame simulates the actuation load and measures the force and

displacement of the SMA actuator. This loading frame was composed of a load cell, a LVDT, a compression spring and linear bearings.
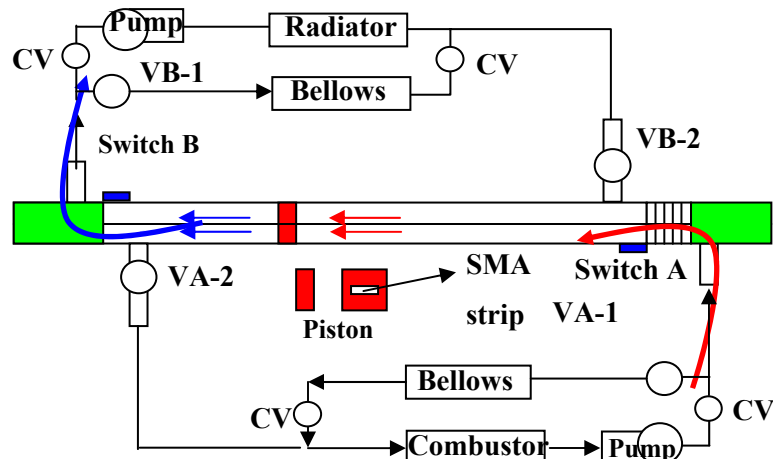
Figure 82. Schematic of the final SMA actuator system.
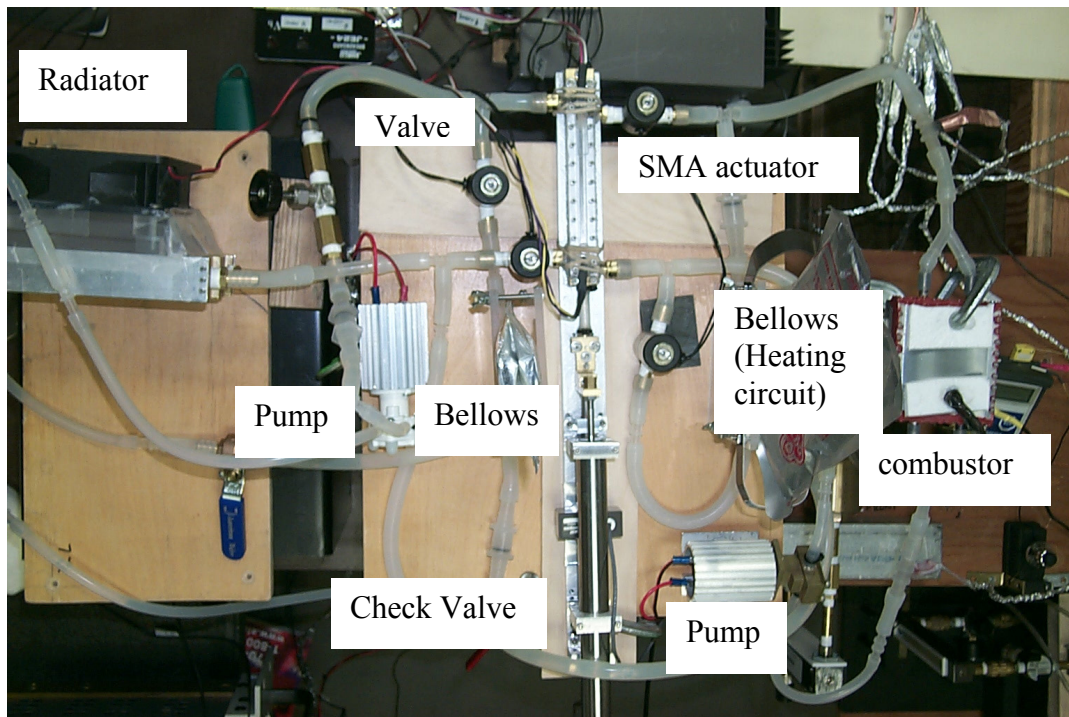
Figure 83. Experimental setup of the final SMA actuator system.

8.1. Numerical analysis of the final SMA actuator

A numerical heat transfer analysis was carried out, using commercial packages such as FLUENT 6.0 and GAMBIT 1.3.0, in order to estimate the period of the heating and cooling cycles and thus the actuation frequency. The SMA transformation temperatures used were: A^f=363.83 °K (90.68 ºC) and A^s=353.42 °K (80.27 ºC) at 150 MPa. For the numerical calculations, the initial temperature of the SMA strip was 335 °K (61.85 ºC) and the inlet velocity and temperature were 1 m/sec and 370 °K (96.85), respectively. The working fluid was hot water. Energy losses through both ends of the SMA channel and the channel walls were ignored. The latent heat of the SMA strip was also considered in this calculation.

The dimensions of the SMA strip embedded in the rectangular channel, as well as the dimension of the rectangular channel were 0.9 mm x 2.5 mm x 114.3 mm and 3 mm x 6.4 mm x 114.3 mm, respectively. The rectangular channel and the strip were the computational domain. The flow was in turbulent state (Re_d=8425), thus the standard κ-ε model, with standard wall functions for the near-wall region was used. A quarter of the channel and the SMA strip were considered as the computational domain by using symmetric conditions, as in chapter IV. Figure 84 shows cross sections of the computational domain and velocity distributions along the channel. The maximum velocity was occurred above the center of strip, with the velocity around the strip being at 1 m/sec.

Figure 85 shows the temperature distribution along the length of the SMA strip at the middle cross section after 0.39 sec, when the strip was fully transformed to austenite.

The corner temperatures of the strip were higher than those of the center, jus like the

results for the rectangular channels I and II, presented in chapter IV. Thus from the

numerical analysis we can estimate the available actuation frequency of the SMA

actuator at around 1.25 Hz at 150 MPa stress.
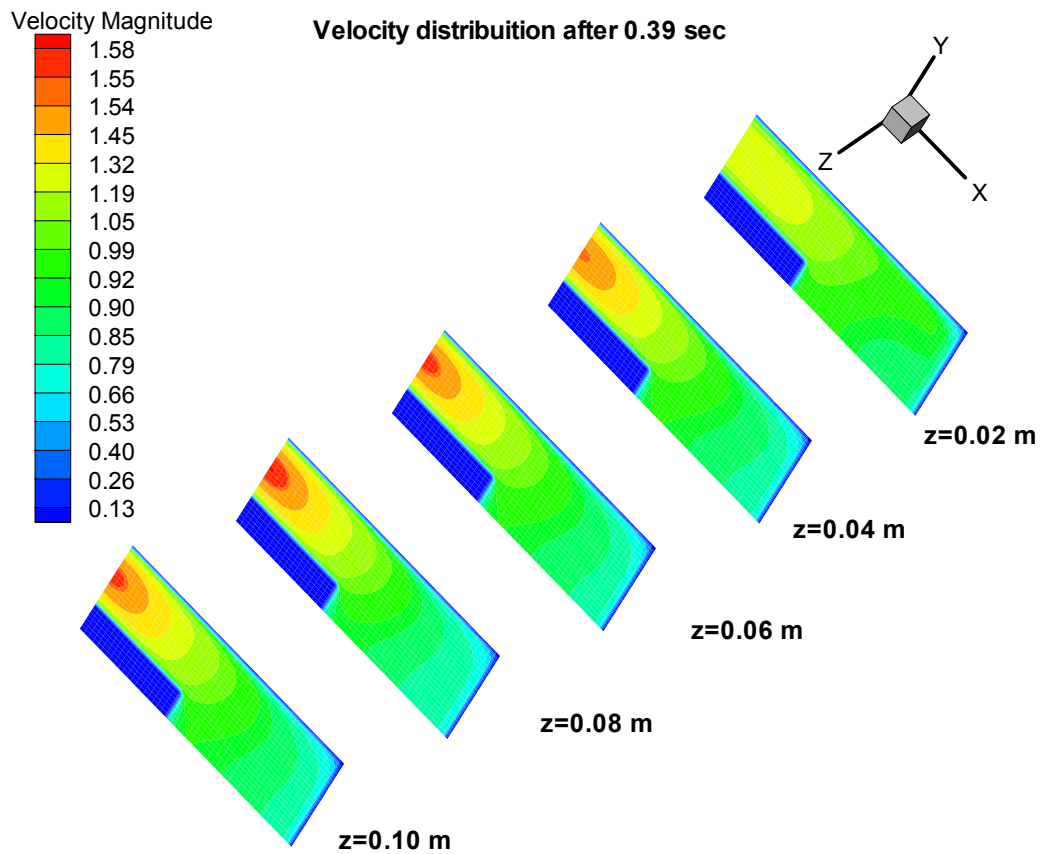
Figure 84. Velocity distribution after 0.39 sec.
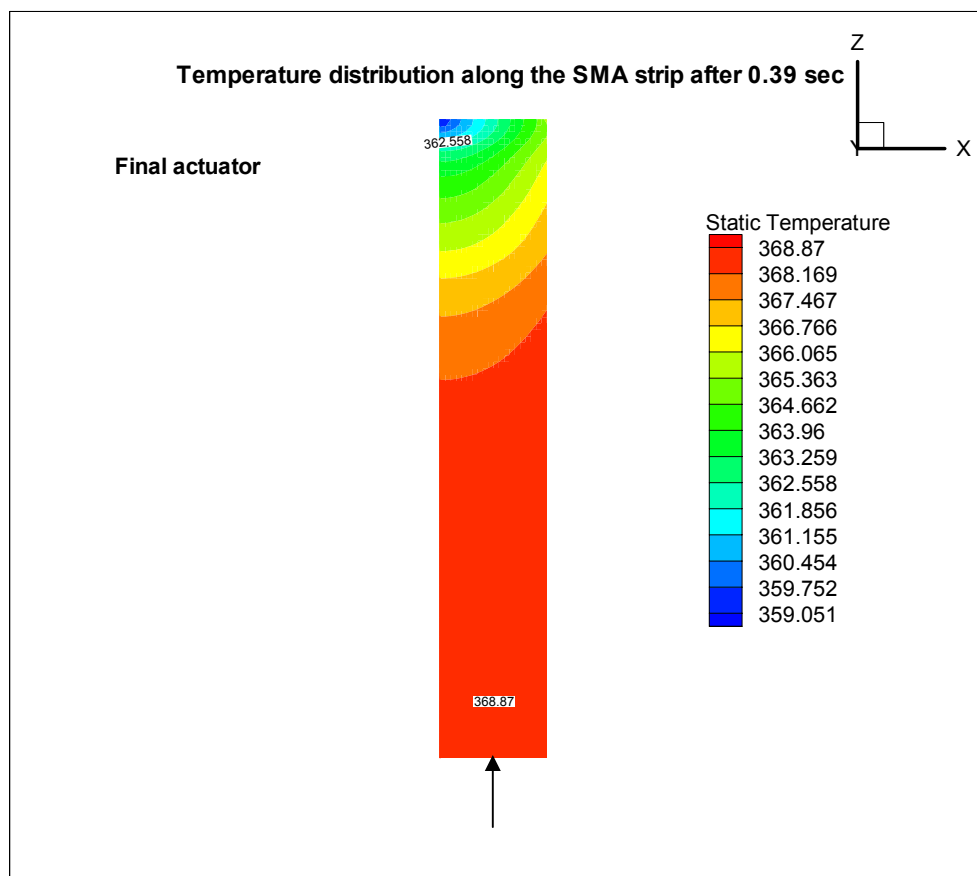
Figure 85. Temperature distribution along the strip after 0.39 sec (heating case).

8.2. Control and operating principles of the final SMA actuator system

Two gear pumps are controlled by on/off signals from a Lab-Windows program according to the pre-set frequencies of actuation (0.5 Hz, 0.75 Hz, and 1.0 Hz). The on/off signals for the pumps and the signals from Hall effect switches operated by a magnet in the rectangular piston, control the four solenoid valves. Figure 38 explains the control logic for the final and the second-generation SMA actuator system. If the heating pump (pump A), as shown in Figure 82, is on, the hot fluid pushes the rectangular piston in the channel to the switch B shown in Figure 82, by driving hot water from the

bellows. As soon as pump A is on, valve A-1 is closed and valve B-1 is open. Thus, the cold fluid on the left side of the piston in the channel goes into the cooling circuit. Finally this cold fluid, which is on the left side of the piston in the channel, goes into the bellows of the cooling circuit. When the piston reaches the other end, the magnet on top of the rectangular piston makes the Hall effect switch B go on. At that moment, the valve B-1 is closed and valve A-2 is opened. Thus the hot water passes through the valve A-2, combustor/heat exchanger, pump A, valve A-1 and the rectangular channel. Finally the complete heating circuit including the rectangular channel is built during the heating of the SMA strip. The hot fluid heats the SMA strip and gets reheated at the combustor/heat exchanger to compensate for its energy losses caused by heat transfer to the SMA strip and mixing between the hot and the cold fluid in the system. The cooling circuit also works like the heating circuit, as explained above.

8.3. Components of the final SMA actuator system

8.3.1. SMA element and channel

A K-alloy type SMA strip, which is a Ni, Ti and Cu alloy, is used as the SMA element, as in the first- and second-generation SMA actuator systems. Its cross section is 2.5 mm x 0. 9 mm (0.1 inch x 0.034 inch) and it is cut by EDM (Electrical Discharge Machining) to a dog-bone shape, after being annealed to prevent stress concentration at the two ends of the SMA strip (Figure 86).
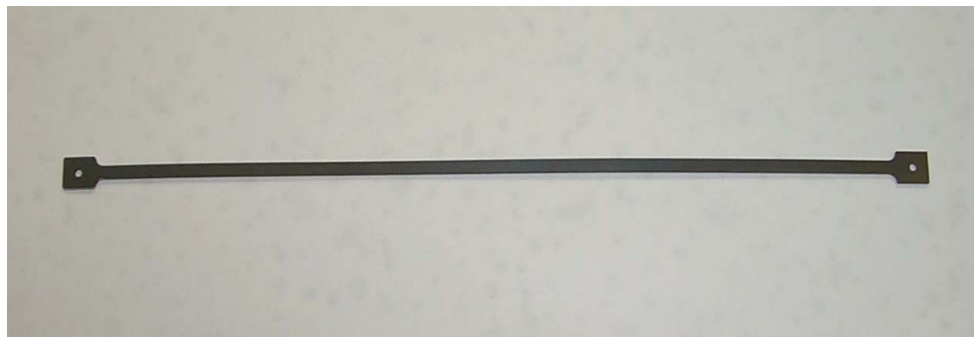
(a) SMA strip (cut by EDM)

Magnet (D=3.1 mm)
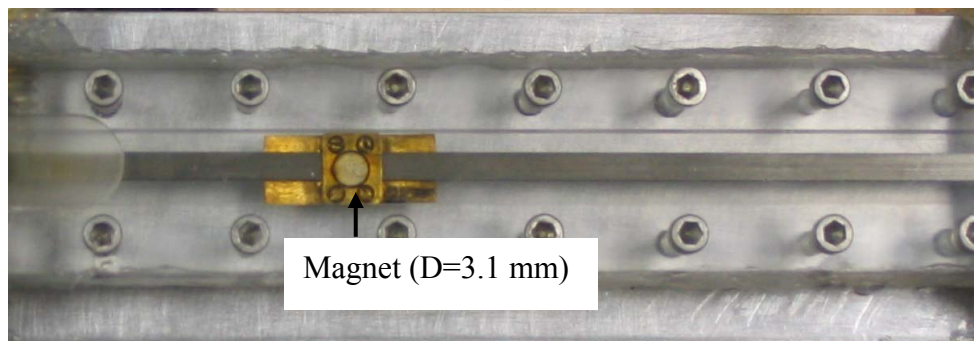
(b) SMA strip and piston in channel

Figure 86. SMA strip and piston in channel.

We selected the rectangular channel dimension as 3 mm x 6.4 mm (0.12 inch x 0.25 inch) dictated by the need to have enough room to accommodate a magnet (for Hall effect switches) and screws on the piston. The piston size is 3 mm x 6.4 mm x 15.2 mm with a 3.1 mm diameter magnet on top of it to control the Hall effect switches. The piston was made of three components; the magnet, bottom part and top part. Top and bottom parts were put together by screws to be easily assembled and disassembled. Figure 87 shows the rectangular piston with the magnet.

The channel design of the final SMA actuator is based on the second-generation SMA actuator, which was designed to decrease the mixing between the hot and cold

fluid in the system. Figure 88 shows the SMA element and the rectangular channel. The SMA actuator, which is similar to that of the second-generation SMA actuator, is composed of two end connectors, rectangular channel, top plate, silicon tubing to accommodate expansion and contraction of the SMA element, piston with magnet and a SMA strip. The rectangular channel and the top plate were made of transparent plastic material in order to check the movement of the piston as shown in Figure 86. RTV (high temperature silicon) and screws were utilized to seal the channel. The main function of the rectangular piston is to separate the hot and cold fluids in the channel during the actuation thus decreasing the mixing in the system. The piston has a magnet on top of it in order to turn the solenoid valves on and off according to the heating and cooling cycles. The rectangular piston has a slot in the middle of its cross section to accommodate the SMA strip and runs along the SMA strip. One of the ends of the SMA element (left end in Figure 88) was embedded in flexible silicon tubing in order to accommodate the expansion and contraction of the SMA strip.
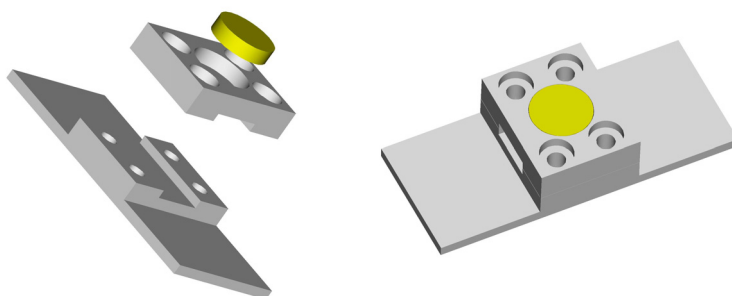
Figure 87. Rectangular piston with magnet.
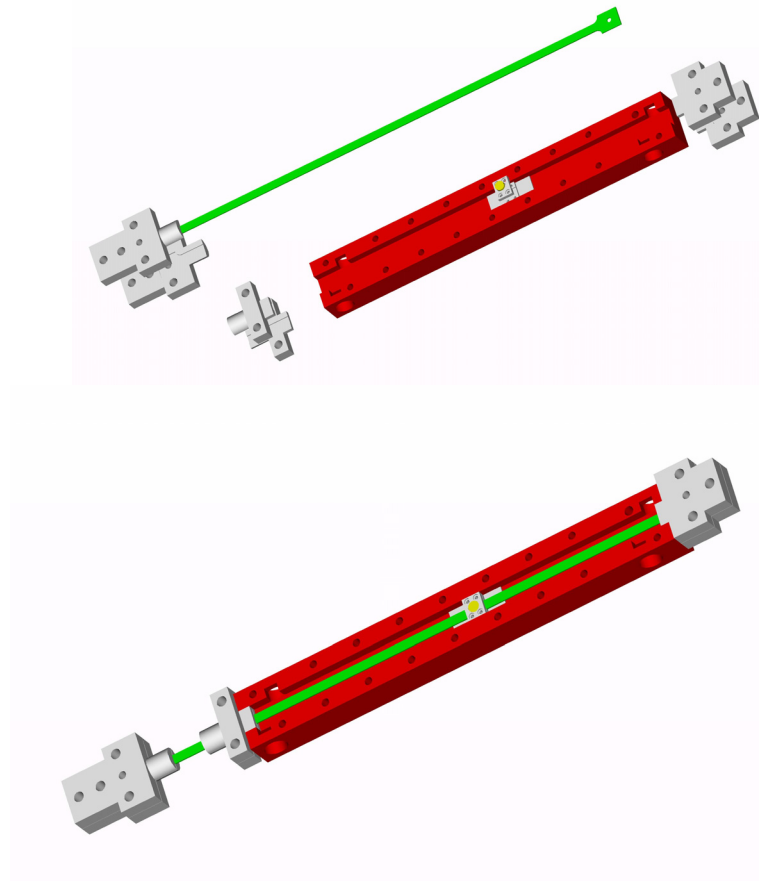
Figure 88. Final SMA actuator (Pro/Engineer drawings).

8.3.2. Loading frame

The loading frame is designed and fabricated to simulate the actuation load and measure the force and displacement of the actuation. Figure 89 shows this loading frame, which is composed of 2 linear bearings, a compression spring, a load cell, a LVDT and an aluminum frame. The compression spring generates the restoring force, as well as helps the movement of the piston along the strip by pulling the SMA strip straight. The initial stress and recovery stress of the SMA strip are adjustable by changing the spring force or spring constant. The dimensions of the compression spring are 15.5 mm in outside

diameter and 41.4 mm in length. Its spring coefficient is 56.6 N/mm (323 lb/in). A 1335 N load cell (by Transducer Techniques) measures the actuation force of the SMA strip and a LVDT measures the recovery strain.
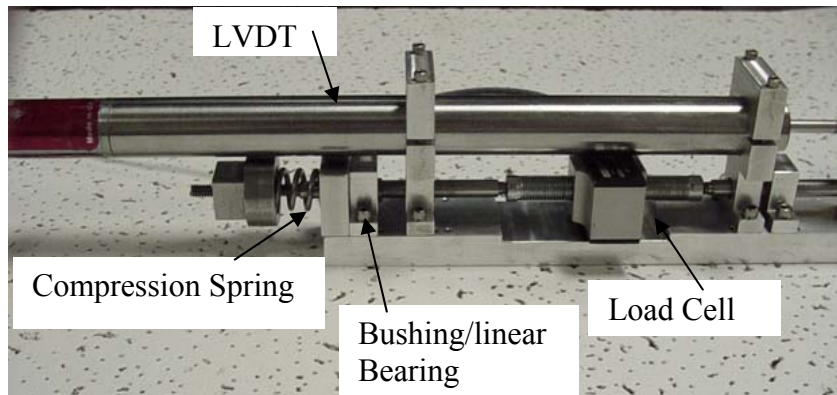
Figure 89. Loading frame for the final actuator system.

8.3.3. Combustor/ heat exchanger

A newly designed multi-channel combustor/heat exchanger, discussed in Chapter VII, was utilized as the combustor, which supplied the main energy to the actuator system. Its flame was adjustable up to 800 Watts and ran on a valved butane and propane mixed cartridge, which contained 450g of fuel. The size of the combustor/heat exchanger was 76.2 mm x 71.1 mm (3.0 inch x 2.8 inch), which was about ¼ of the first-generation combustor/heat exchanger. The channel size of the heat exchanger side was 76.2 mm x 0.81 mm (spacing: 0.032 inch=0.81 mm). The channel size of the combustor side was 2.5 mm x 0.81 mm (spacing: 0.032 inch=0.81 mm) and was fabricated by aluminum. The total number of channels of each side is 39. Screws and RTV sealed the

combustor/heat exchanger. The efficiency of the combustor/heat exchanger was estimated at around 70%. Figure 90 shows the multi-channel combustor/heat exchanger utilized in the final SMA actuator system.
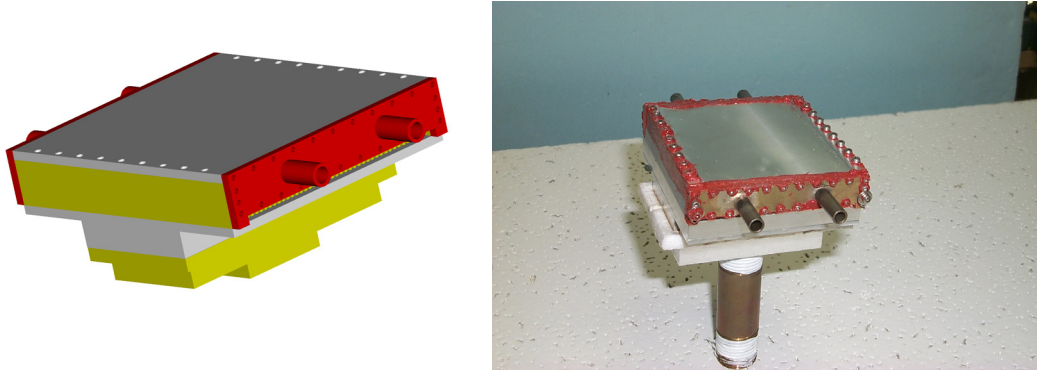
Figure 90. Multi-channel combustor/heat exchanger.

8.3.4. Micro-tube heat exchanger

The micro-tube heat exchanger disposes of the energy obtained from the SMA strip to the surroundings, by forced air convection cooling. The micro-tube heat exchanger operated under laminar flow conditions. A 59.2 l/min (125.5 CFM) fan was used to generate the force air convection as shown in Figure 83. 561 copper micro tubes (having 0.95 mm outside diameter, 0.7 mm inside diameter and 140 mm length) were used to increase the heat transfer rate and decrease the volume size of the heat exchanger. The micro-tube heat exchanger, as shown in Figure 91, measures 114.3 mm x 177.8 mm x 28 mm (core size=100 mm x 130 mm x 20 mm) and has high heat transfer rate.
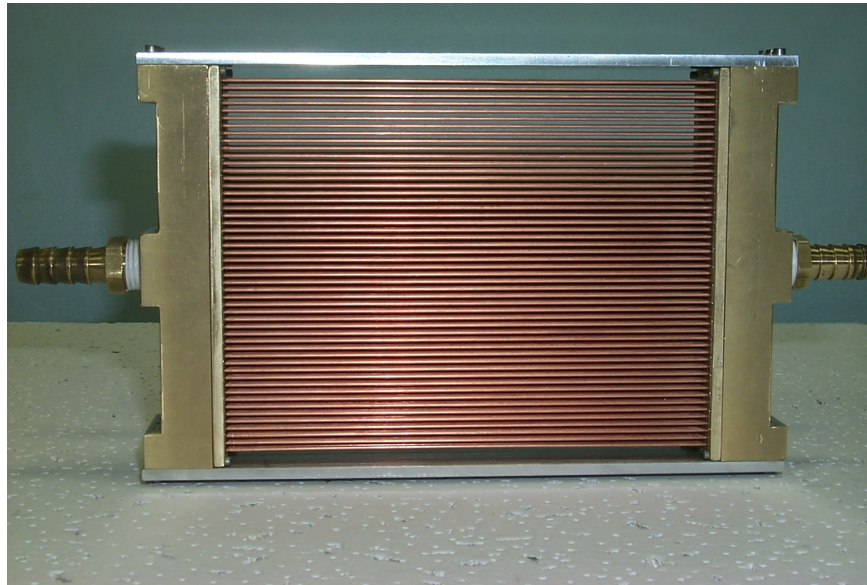
Figure 91. Micro-tube heat exchanger.

8.3.5. Pumps

The Greylor PQ-12 gear pump, weighting 283 g, circulates the cooling medium. Its maximum flow rate is 2.22 l/min at low-pressure loss and can withstand 20 psi and 80 °C. The components that come into contact with the fluid being pumped are molded Delrin gears in Delrin pump body. A brass gear pump was designed and fabricated in our CNC machine, in order to run at high operating temperatures. The pump operation was based on two brass gears with following parameters: 24 pitch, 9 teeth, pitch diameter = 9.5 mm (0.375 inch), outside diameter = 11.6 mm (0.458 inch) and height = 9.5 mm (0.375 inch). The pump circulates the hot medium and is run by a DC motor. These pumps run alternatively according to the heating and cooling cycles. O-rings and screws were used to seal the brass gear pump. Table 6 shows the performance of PQ-12 gear pump.

Table 6. PQ-12VDC performance data at 12 volt DC [50].

Pa	PSI	Ml/min	Volt	amp
0	0	2200	12	1.5
34.5 KPa	5	2100	12	1.6
68.9 KPa	10	1750	12	1.8
103.4 KPa	15	1250	12	2.0
137.9 KPa	20	350	12	2.2

The brass gear pump has the following dimensions; 26.7 mm x 38.1 mm x 35.6 mm (1.05 inch x 1.5 inch x 1.4 inch). Figure 92 shows the designed brass gear pump with two brass gears.
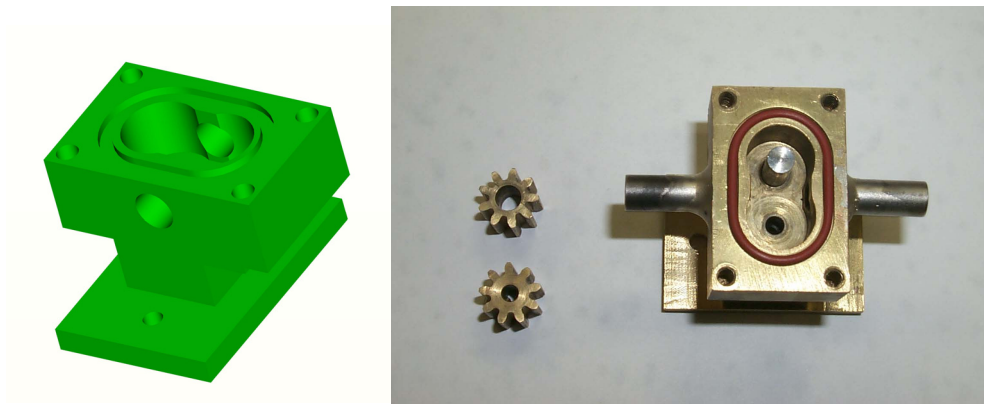
Figure 92. Brass gear pump.

Table 7 shows the measured performance of the brass gear pump. The flow range is from 694 ml/min at 10 psi (68.9 KPa) to 1893 ml/min at 3.5 psi (24.1 KPa). The speed of the motor shaft was 6000-6500 rpm, which was measured by an optical tachometer.

Table 7. Brass gear pump performance data at 12 volt DC.

Pa	PSI	ml/min	Volt	Amp
24.1 KPa	3.5	1893	12	1.6
41.4 KPa	6	1432	12	1.65
55.2 KPa	8	1117	12	1.75
62.1 KPa	9	864	12	1.9
68.9 KPa	10	694	12	1.9

8.3.6. Valves

Four Precision Dynamics solenoid valves were utilized to control the heating and cooling circuits. The valves have a 0.4-Cv and are 2-way solenoid valves with a weight of 132 g. They have a class-H (180 °C) rated tape-wrapped coil, and the seal and o-ring are out of Ethylene propylene rubber. These valves can be operated at 120 °C. Four check valves were used to prevent reverse flows in the system. The check valves are made from Polypropylene and can be operated at 120 °C and 20 psi (137.9 KPa).

8.3.7. Bellows

Two flexible plastic bags, which were used for the second-generation actuator system, are used in the final actuator system as bellows. Each circuit has one bag/bellows.

8.3.8. Switches

The Hall effect magnetic sensor (DN6840) detects the presence of a magnetic field. A small, permanent magnet (3.1 mm in diameter and 0.66 mm in height) housed on top of the rectangular piston is easily detected with this sensor. Two Hall effect switches were

used to control the solenoid valves, thus alternatively turning the heating and cooling circuits on and off. Figure 93 shows the magnet and the Hall effect magnetic sensor.
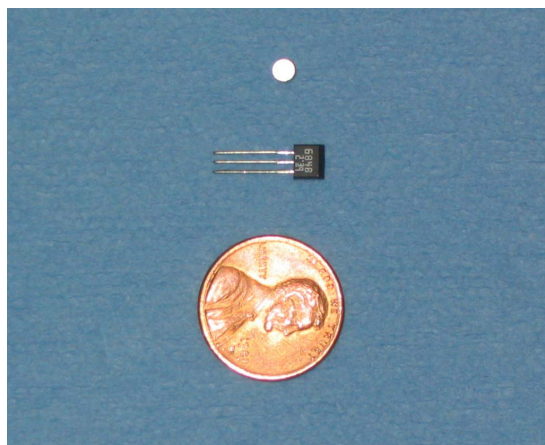
Figure 93. Hall effect magnetic sensor and magnet.

8.3.9. Control and data acquisition

SN7406s (hex inverter buffer), SN7408s (quad 2-input AND gate), Hall effect sensor and solid-state relays such as DO061 and MODC5, were used to make the control circuit to control the pumps and the solenoid valves. Figure 94 shows the control circuit board. The data acquisition system is the same as in the second-generation actuator system. A National Instrument AT-MIO-16XE-50 board is used to acquire the temperatures, displacement and force measurements. A National Instrument PCI-6704 D/A board was utilized to control the pumps. A Lab-Windows program was put together to control the hardware and acquire data.
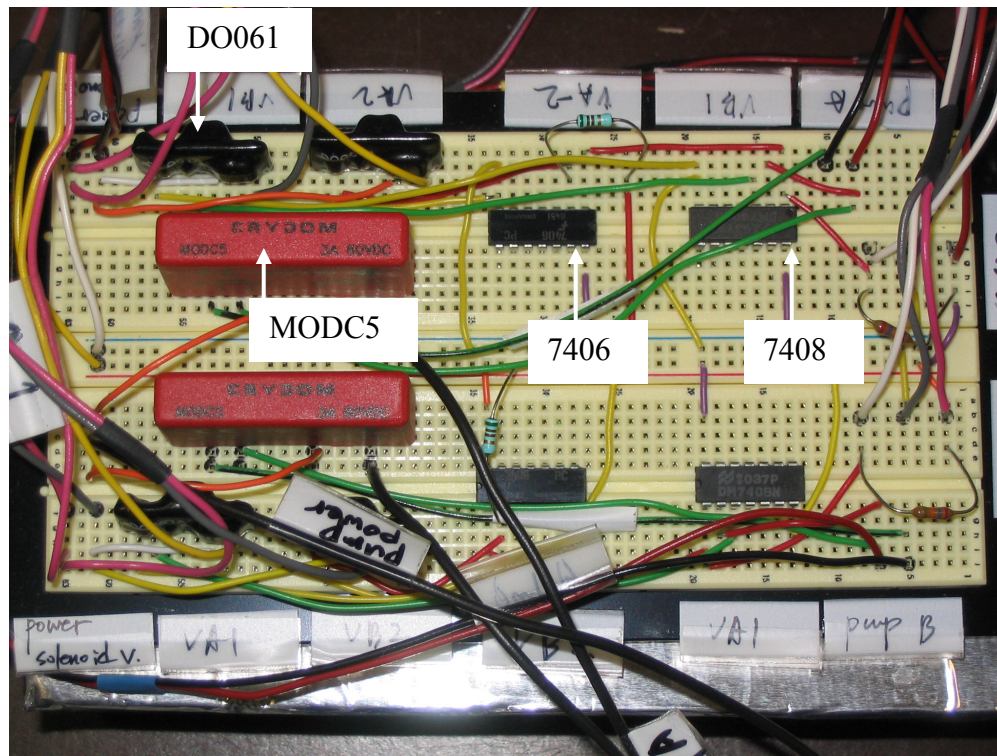
Figure 94. Control circuit board.

8.4. Test results of the final SMA actuator system

The final actuator system based on the newly designed rectangular channel, the SMA strip, the multi-channel combustor/heat exchanger and the micro-tube heat exchanger generates faster actuation frequency compared to the first- and second-generation SMA actuator systems. Most of components and their functions are similar to those of the second-generation system. Water was used as the heating and the cooling mediums. The actuator was connected to the loading frame with an adjustable compression spring. For the actuation tests, initially the restoring force was adjusted to around 90 N. This value was decided upon by considering the actuation displacement of the SMA actuator and

the spring constant. The SMA actuation displacement was obtained from a pre-test actuation of the SMA strip using hot air. Upon SMA transformation, the force was increased to 225 N. This represents a 2.4 mm displacement (2.0 % strain=2.3mm/114.3 mm). The test was conducted in an open-loop configuration and in a closed-loop configuration, where the hot and cold fluids are circulated in the heating and cooling circuits. The hot water, after heating the SMA strip in the channel, returned to multi-channel combustor/heat exchanger and got enough energy from the fuel in the combustor/heat exchanger to compensate for its energy losses by the SMA strip and by the mixing. The cold water cooled the SMA strip to the martensite phase by forced convection and returned to the micro-tube heat exchanger with a fan dissipating the thermal energy obtained from the SMA strip to the surroundings via forced air convection.

8.4.1. Open loop test of the final actuator

In the open-loop configuration, the hot and cold water are not circulated in the system. From the open-loop test, the available maximum actuation frequency based on system characteristics can be determined. From the results of the open-loop test, the actuation frequency of the close-loop system can be predicted. The tests were conducted for three actuation frequencies: 0.5, 0.75 and 1 Hz.

8.4.1.1. 0.5 Hz

Figure 95 and Figure 96 show the displacement and force variations with time at 0.5 Hz. The spring constant is 56.6 N/mm, thus a 2 mm displacement can generate 25.4 lbf (113N) force increment. The effective length of the SMA strip is 114.7 mm (4.5 inch). To compare with the results of the second-generation actuator system, the average stress of the final actuator is adjusted to the same value (71 MPa) or little higher.
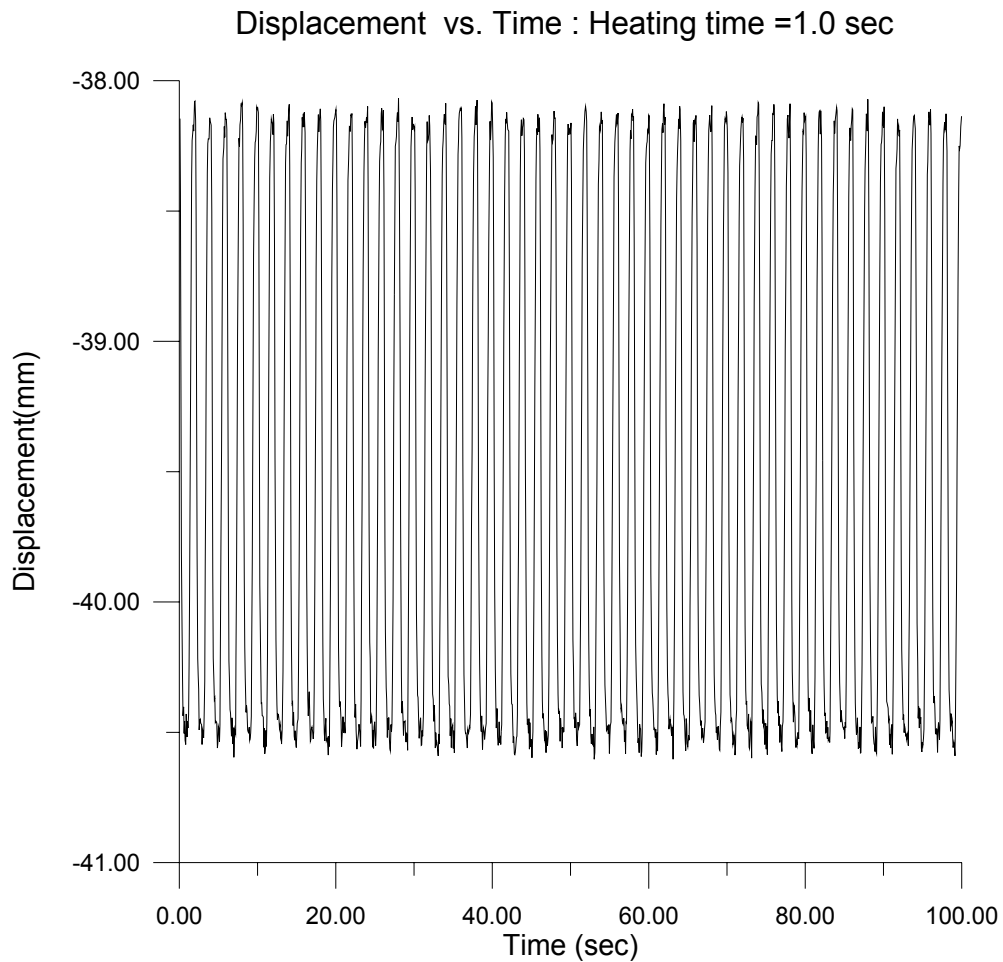
Figure 95. Displacement vs. time of the final actuator system at 0.5 Hz.
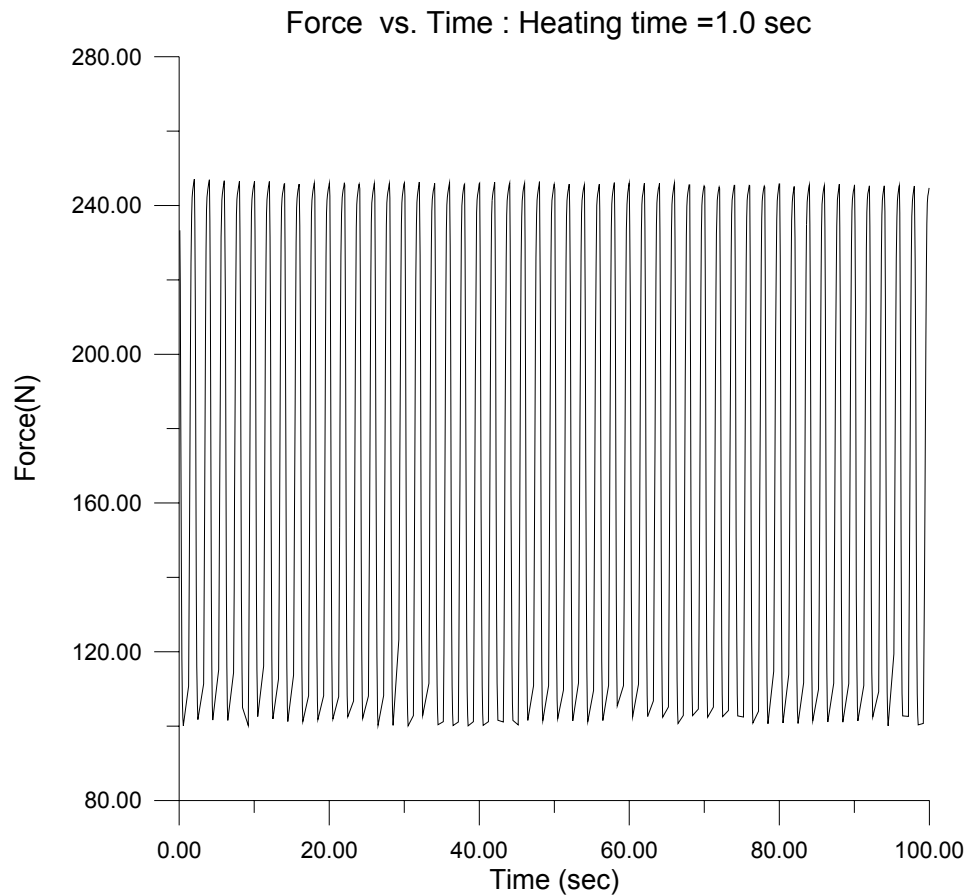
Figure 96. Force vs. time of the final actuator system at 0.5 Hz.

At 0.5 Hz, around 2 % (2.4 mm) strain and 116 MPa (250 N) recovery stress were obtained. The SMA strip was properly heated and cooled at the given conditions during the test.

8.4.1.2. 0.75 Hz

The following two figures (Figure 97 and Figure 98) show the displacement and force responses at 0.75 Hz actuation frequency. The 0.75 Hz actuation tests also sow that the SMA strip was properly actuated during the prescribed heating and cooling intervals.
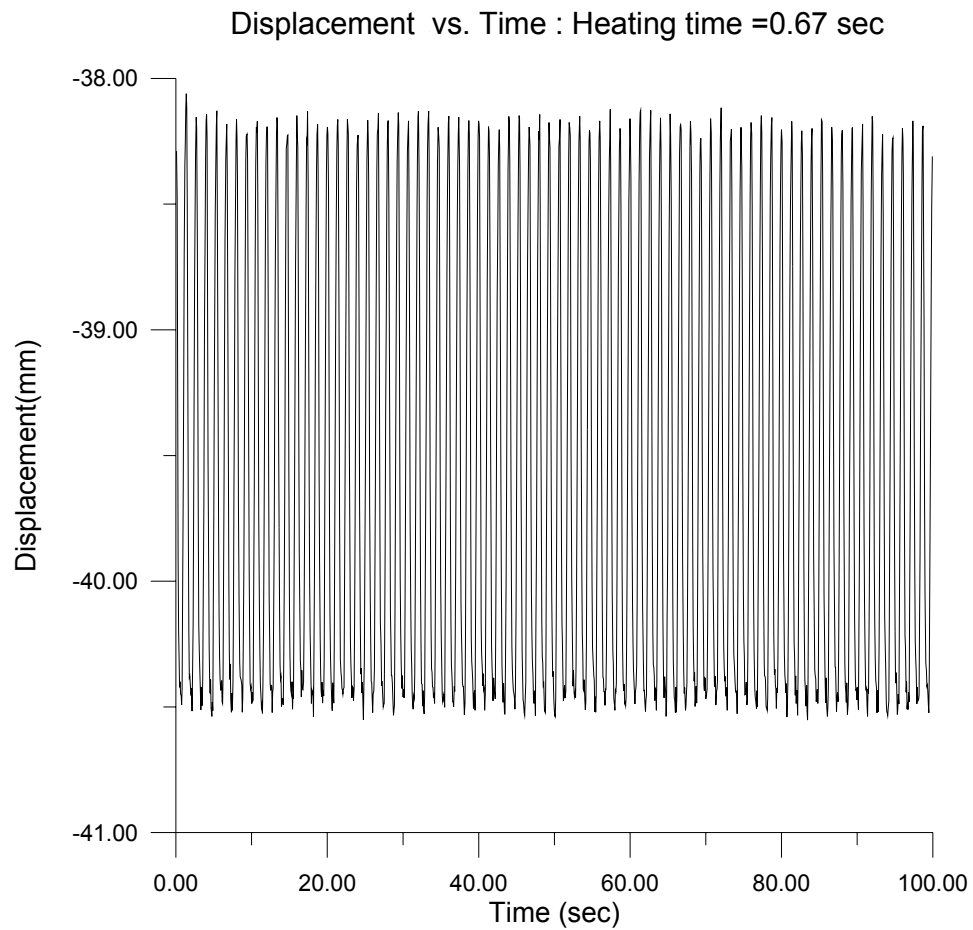
Figure 97. Displacement vs. time of the final actuator system at 0.75 Hz.

From these open-loop tests at 0.75 Hz, the strain was around 2% (2.3 mm) and the force was around 250 N (116 MPa), which were the same as the results of the 0.5 Hz actuation tests.
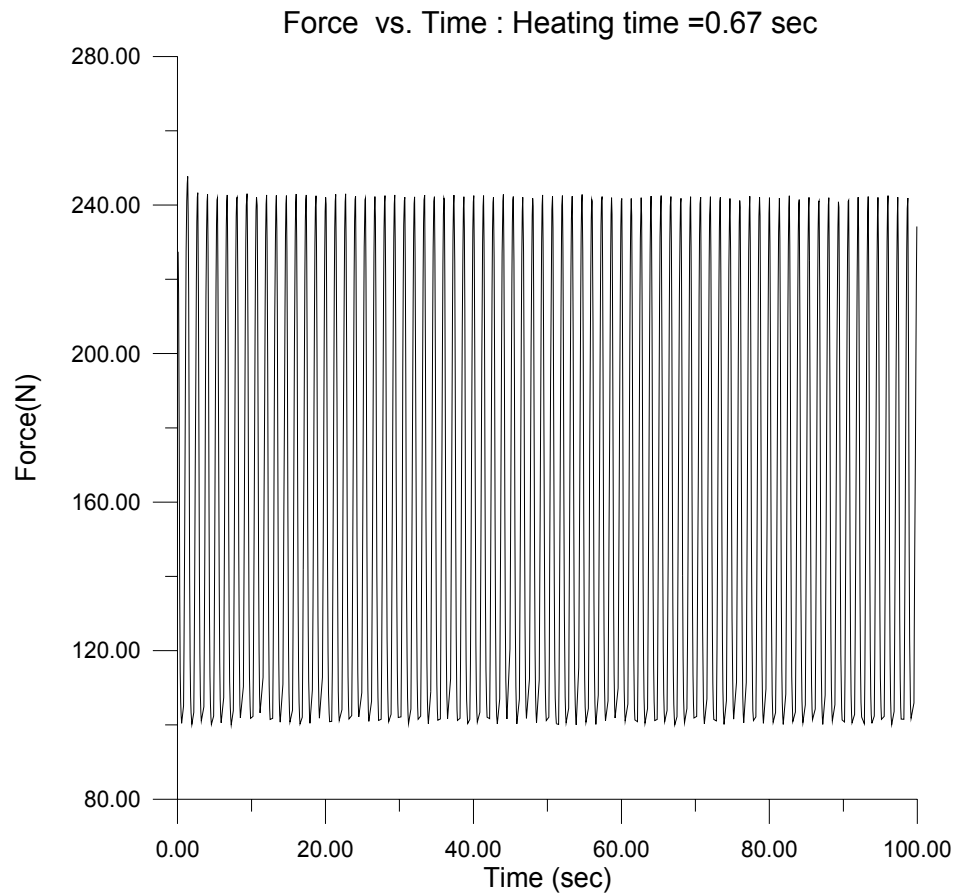
Figure 98. Force vs. time of the final actuator system at 0.75 Hz.

8.4.1.3. 1.0 Hz

Figure 99 and Figure 100 also show the displacement and force variations at 1.0 Hz. These test show that the SMA strip was in 2 % strain and in 116 MPa stress. The strain and stress for the 1.0 Hz case were slightly smaller that those of the 0.5 Hz case. From the open-loop tests, we can estimate the achievable actuation frequency of the SMA actuator system as 1.0 Hz at 116 MPa (maximum stress during the actuation).
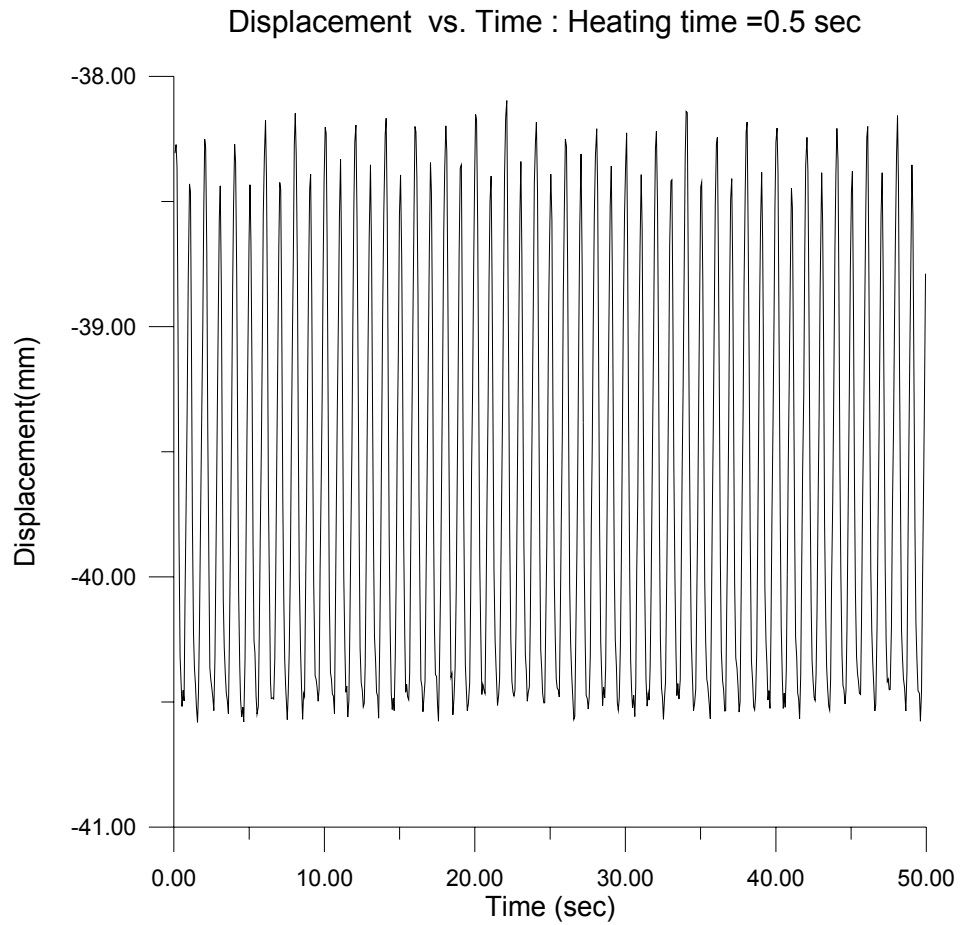
Figure 99. Displacement vs. time of the final actuator system at 1.0 Hz.
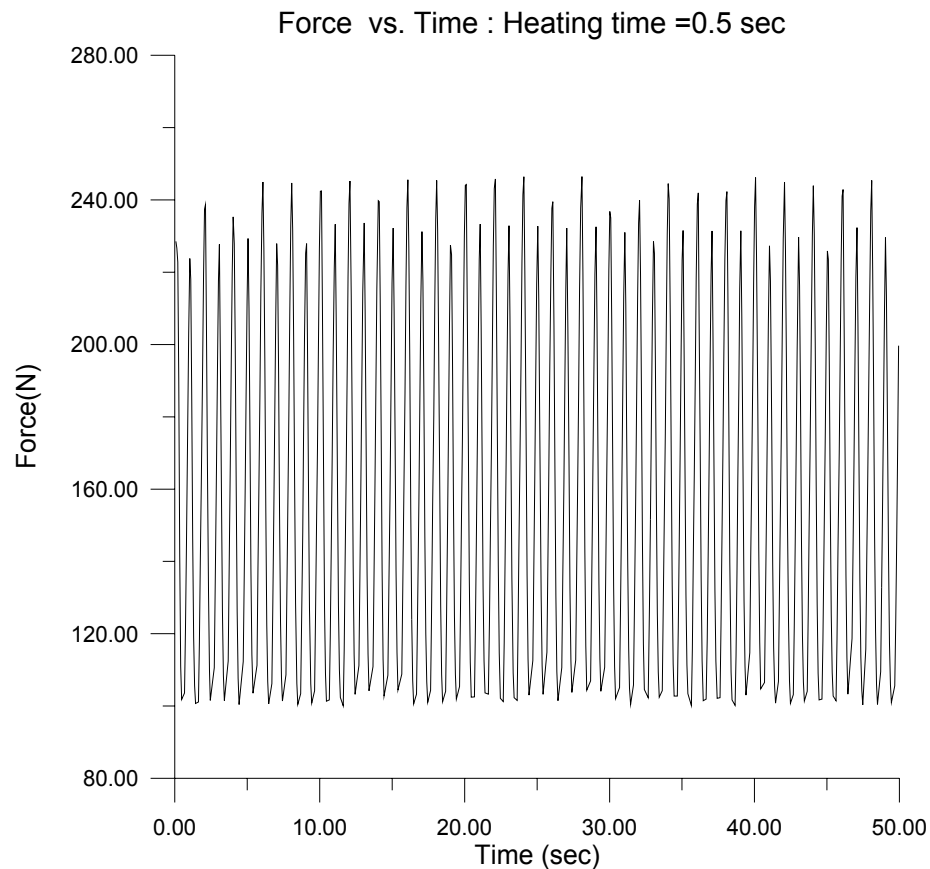
Figure 100. Force vs. time of the final actuator system at 1.0 Hz.

8.4.2. Closed-loop test

The SMA actuator system includes the multi-channel combustor/heat exchanger and the micro-tube heat exchanger with the fan. Small amount of hot and cold water were circulated by the gear pumps in the system during the heating and cooling cycles. From the close-loop tests, the heat exchanger and combustor/heat exchanger can also be evaluated as to weather they have enough power to heat and cool the SMA element and fluids sufficiently.

8.4.2.1. 0.5 Hz

The following figures show close-loop test results at 0.5 Hz actuation frequency. The displacement was around 2.0 mm and force was between 225 N (104 MPa) and 92 N (43 MPa), which vary depending on the initial condition. The force and displacement were similar to those of the open-loop tests. The maximum recovery stress was around 100 MPa, which was dependent on the initial stress and spring settings.

Figure 101. Displacement vs. time of the final actuator system at 0.5 Hz (closed-loop test).

Force vs. Time : Heating time =1.0 sec
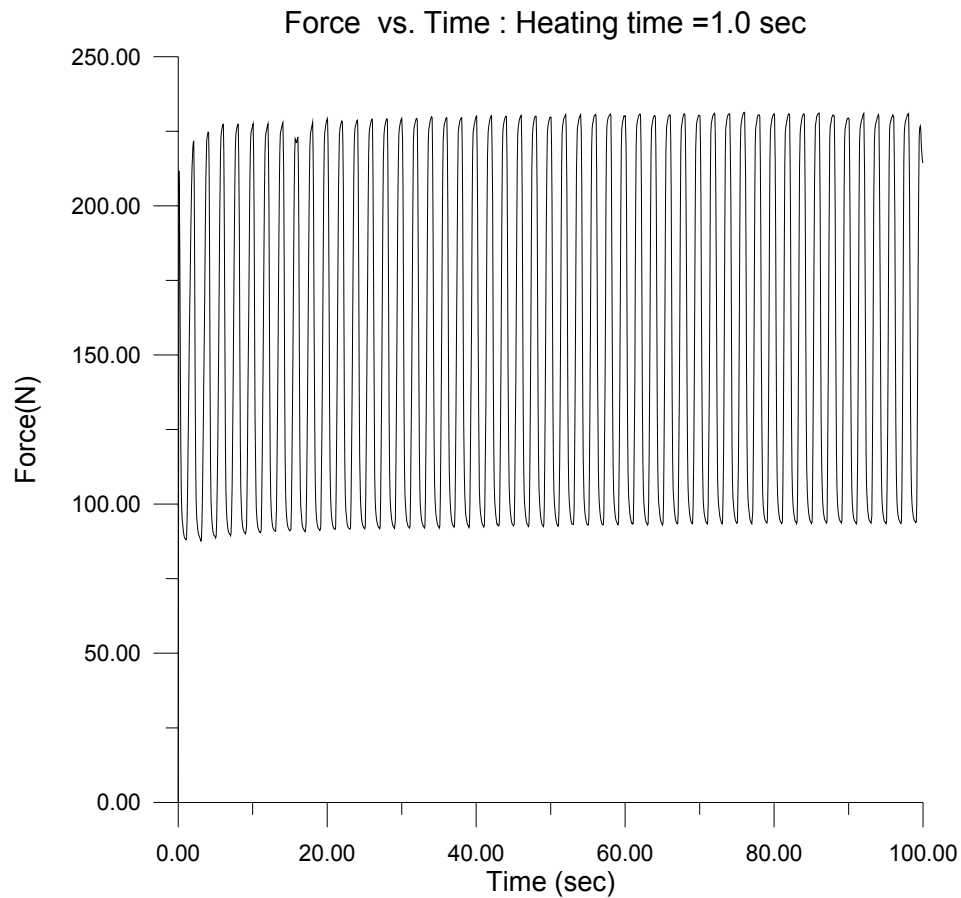
Figure 102. Force vs. time of the final actuator system at 0.5 Hz (closed-loop test).

During the test, the combustor/heat exchanger transferred too much energy to the hot medium and could make the hot medium boil. The temperature of the cooling medium increased by a very small during the testing. Thus the mixing between hot and cold water was small and the performance of the main components, such as combustor/heat exchanger and radiator, were enough to overcome the mixing problems and provide the energy requirements at the given conditions. A flowmeter and valve were used to control the input power to the hot water.

8.4.2.2. 0.75 Hz

Figure 103, Figure 104, Figure 105 and Figure 106 show closed-loop test results at 0.75 Hz actuation frequency. Hot water was filled in the bellows before starting the test. But the water temperature of the heating circuit was not enough high to induce proper actuation in the initial stages of the test.
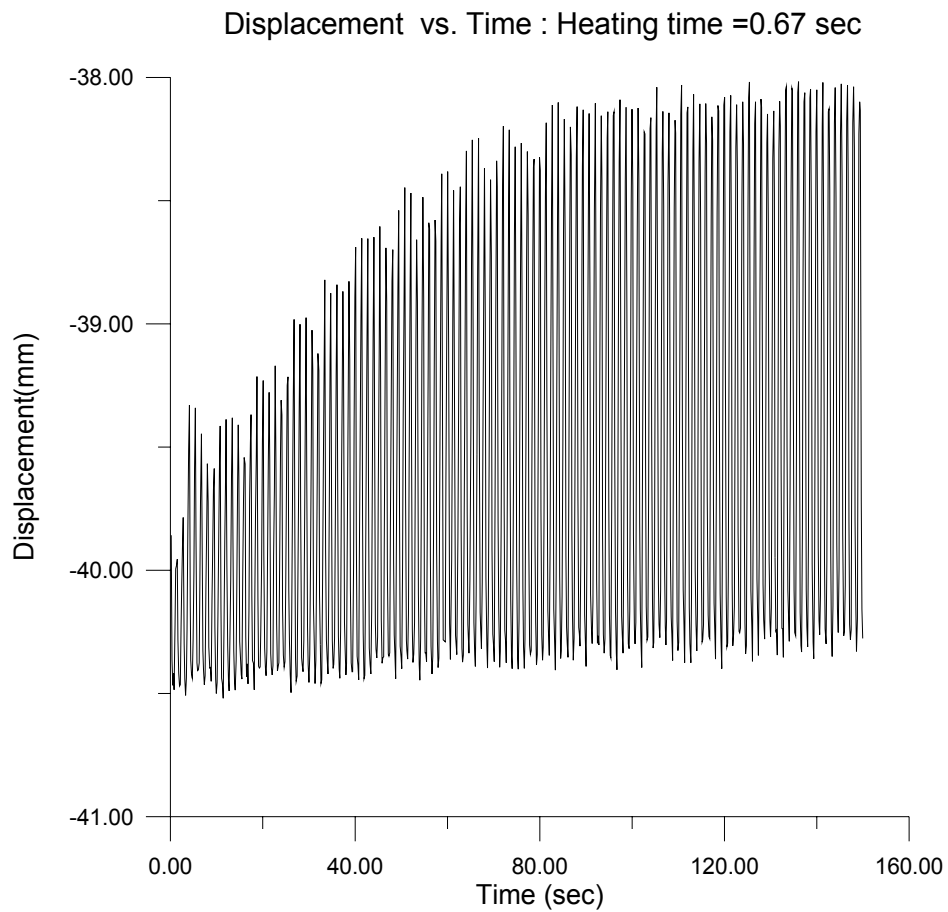
Figure 103. Displacement vs. time of the final actuator system at 0.75 Hz (closed-loop test).
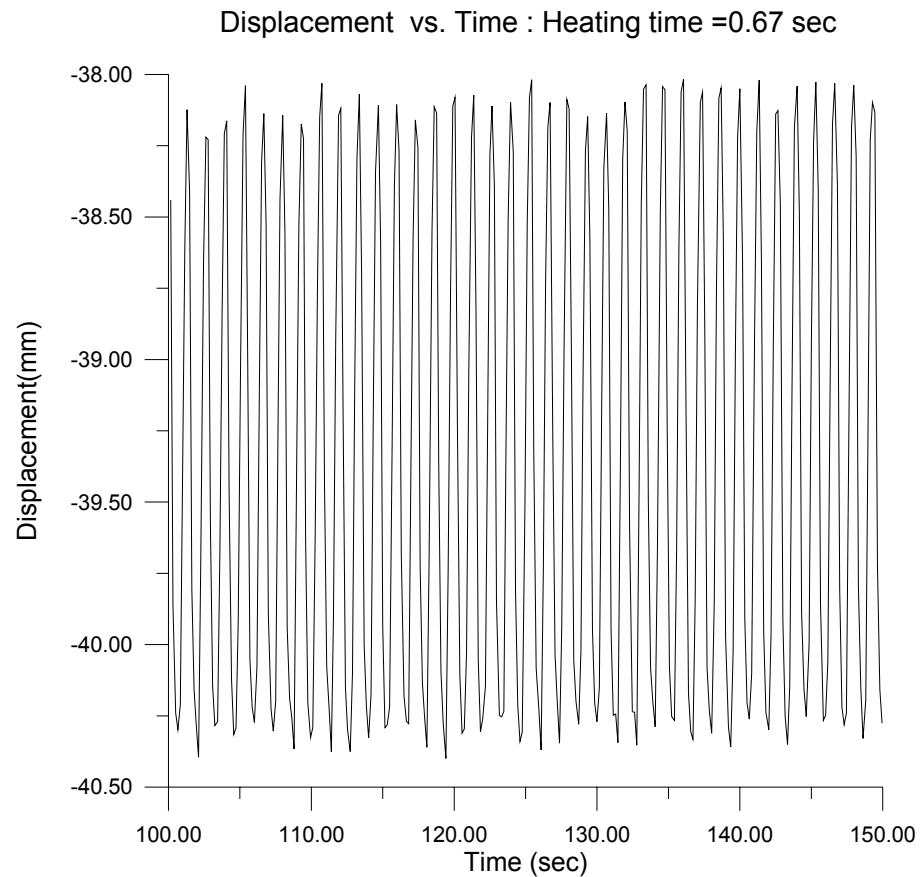
Figure 104. Displacement vs. time of the final actuator system at 0.75 Hz (100-150 seconds).

Figure 103 shows that the temperature of the fluid in the heating circuit increases gradually and finally reaches a limit and saturates. The displacement was around 2.0 mm and the force was between 245 N (114 MPa) and 110 N (51 MPa), which is somewhat higher compared to the 0.5 Hz actuation case. The force and displacement plots show that the combustor/heat exchanger and the radiator have enough power to overcome the mixing problems and provide the energy requirement at 0.75 Hz actuation frequency.
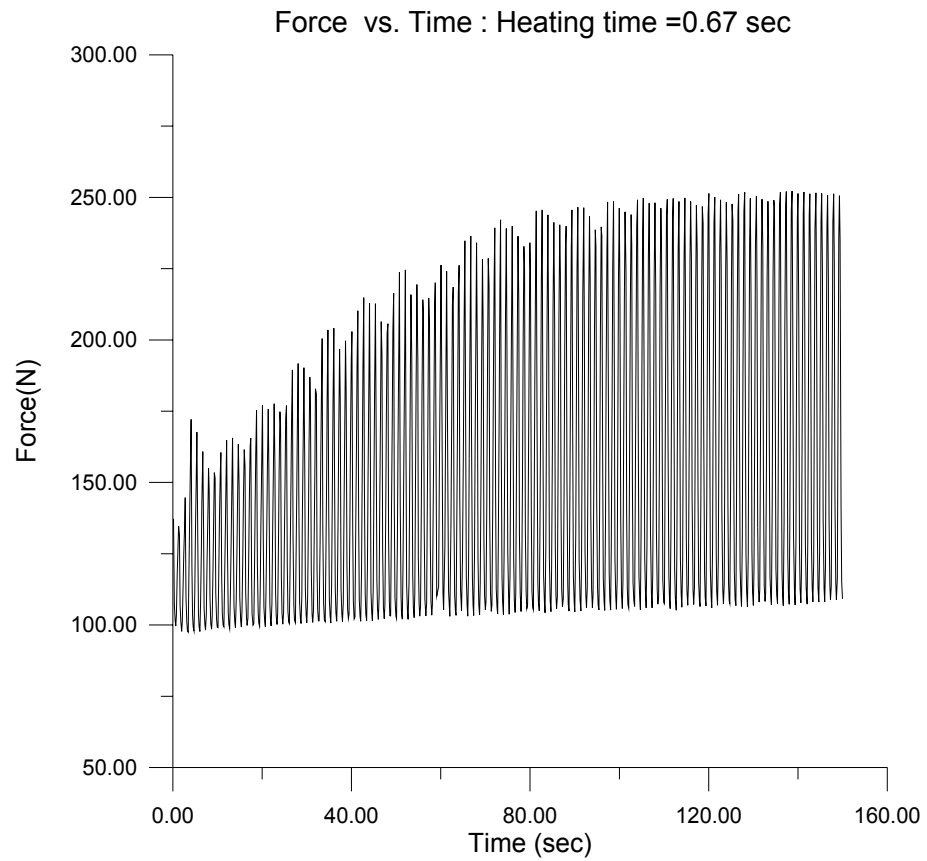
Figure 105. Force vs. time of the final actuator system at 0.75 Hz (closed-loop test).

Force vs. Time : Heating time =0.67 sec
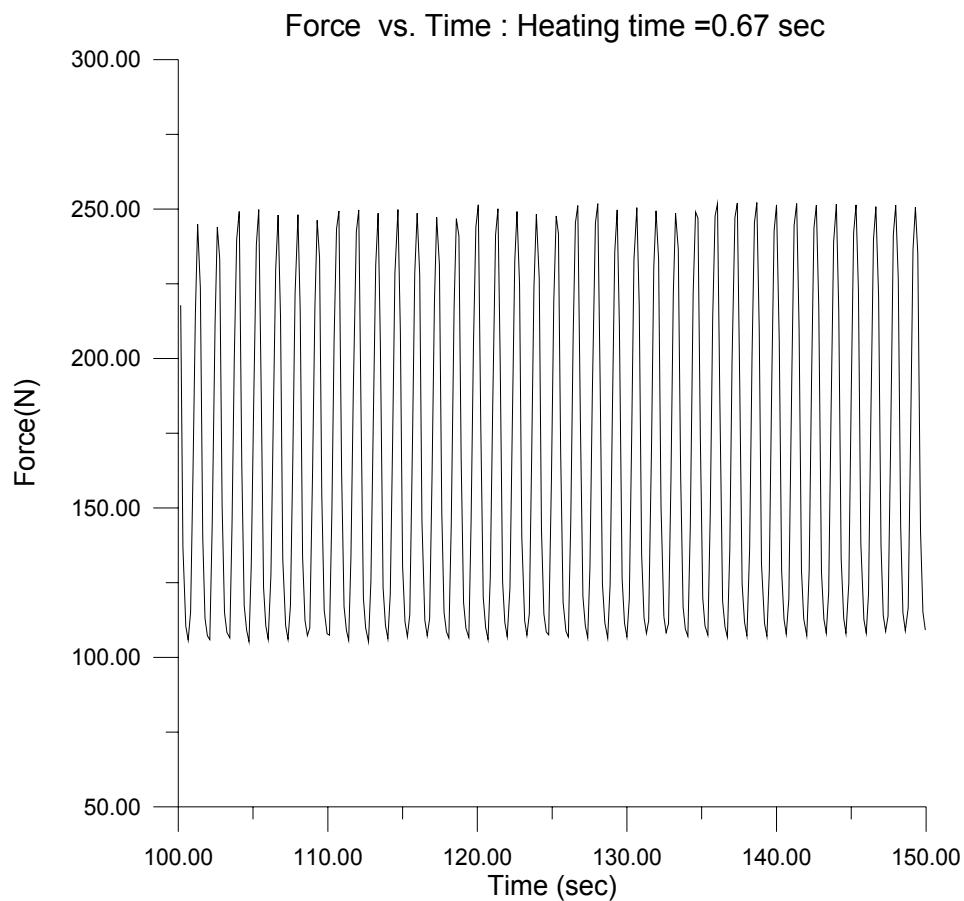
Figure 106. Force vs. time of the final actuator system at 0.75 Hz (closed-loop test, 100-

150 sec).

8.4.2.3 1.0 Hz

Figure 107, Figure 108, Figure 109 and Figure 110 show closed-loop test results at 1.0

Hz actuation frequency. The heating and the cooling periods of the SMA strip were 0.5

second each. These plots also show that the combustor/heat exchanger and radiator have

enough power at the given conditions. The mass of each circuit is balanced after 150 sec.

The displacement was around 2 mm and the maximum stress was 114 MPa, which are

the same values as in the 0.5, 0.75 Hz and 1.0 Hz tests of open- and closed-loop systems. Thus the actuation frequency of the final SMA actuator system was 1.0 Hz in closed-loop configuration at the given conditions. This value is 4 times faster than that of the second-generation SMA system.
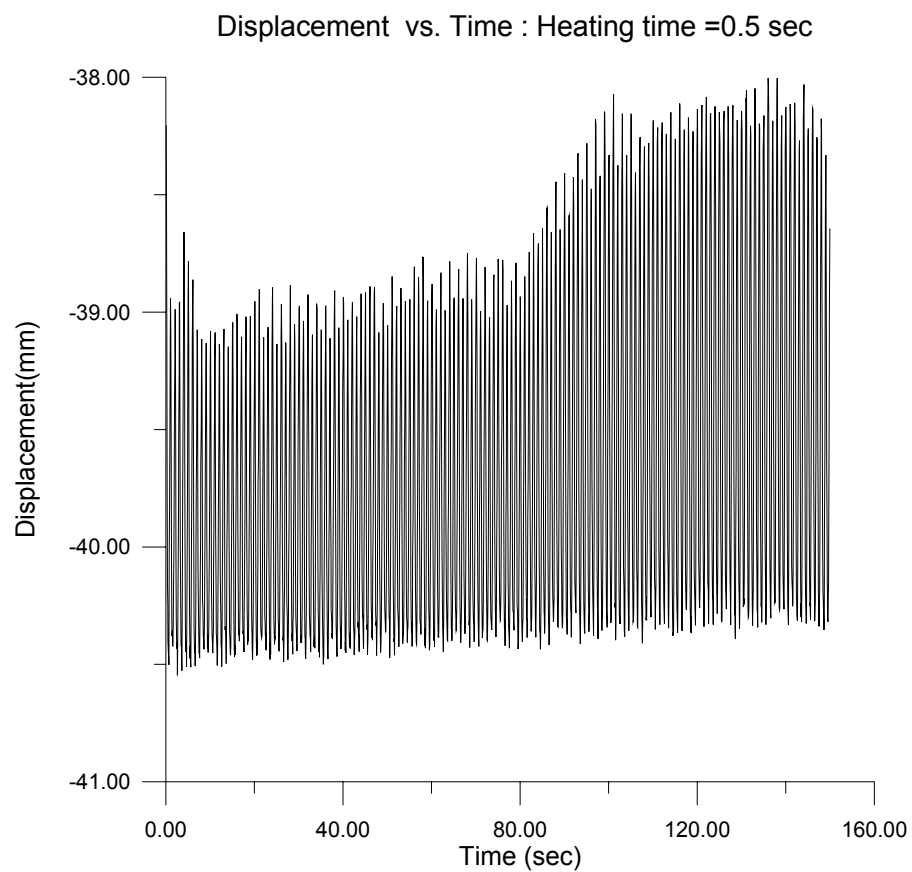
Figure 107. Displacement vs. time of the final actuator system 1.0 Hz (closed-loop test).
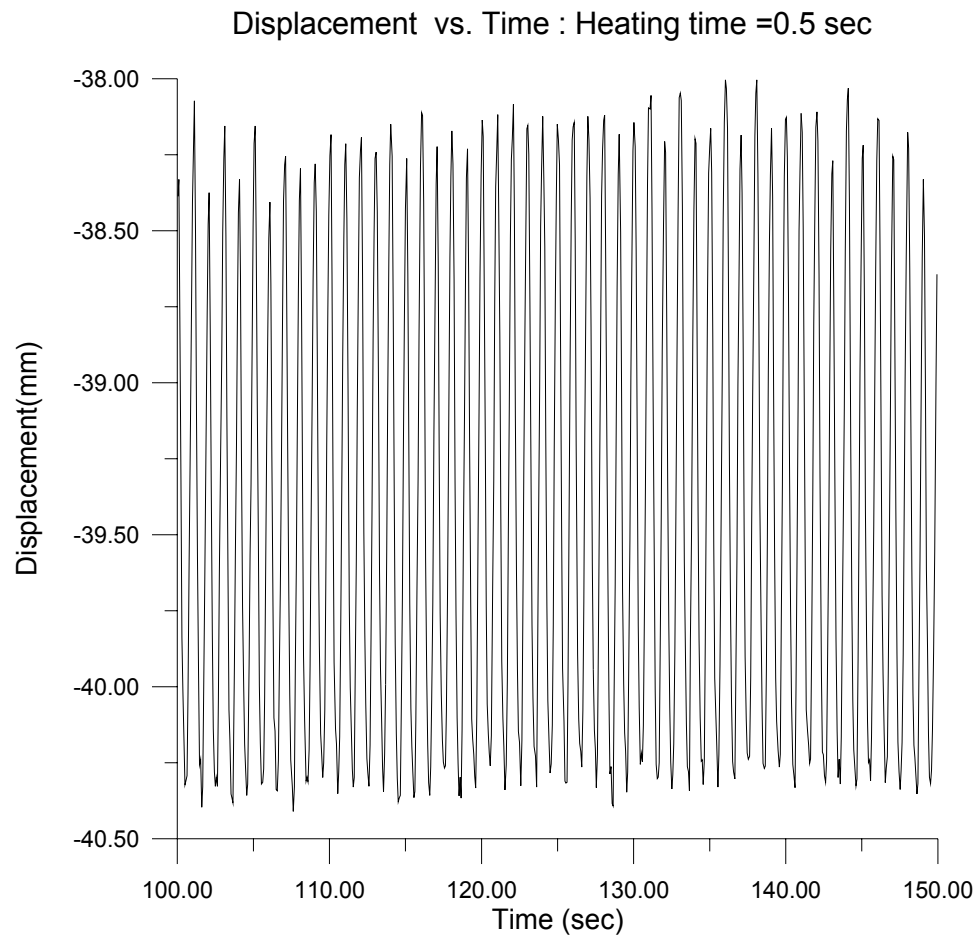
Figure 108. Displacement vs. time of the final actuator system at 1.0 Hz (closed-
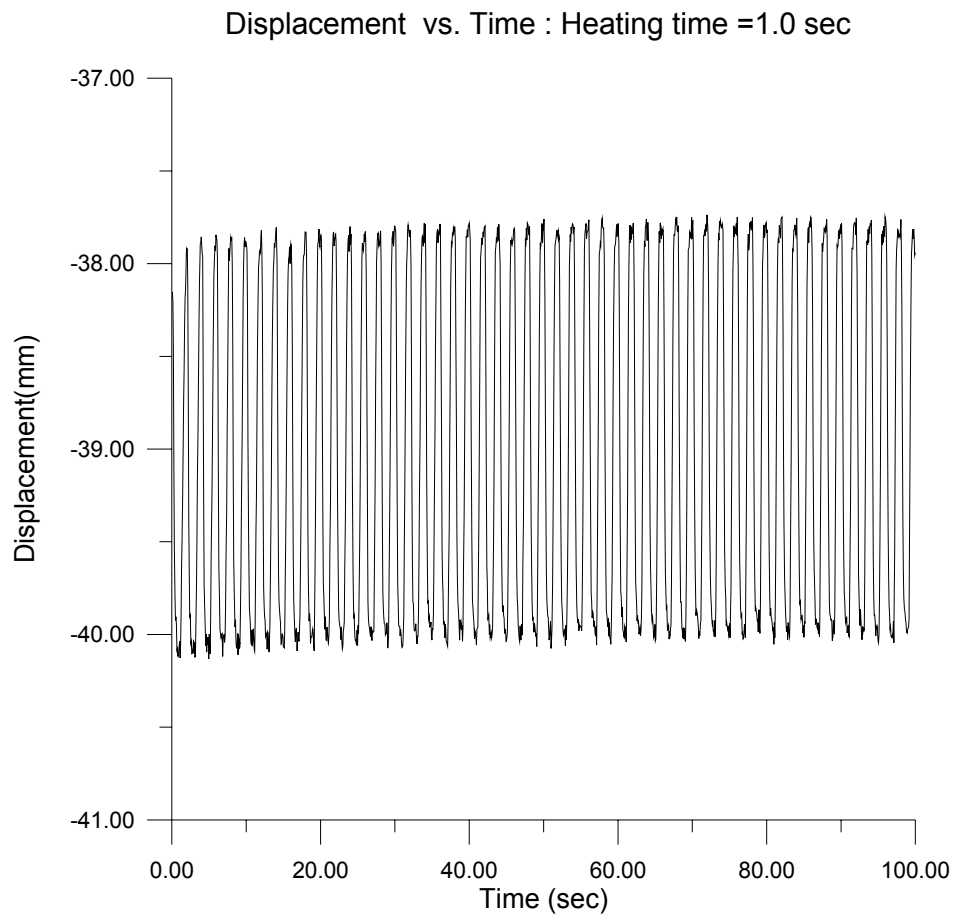
loop test, 100-150 sec).
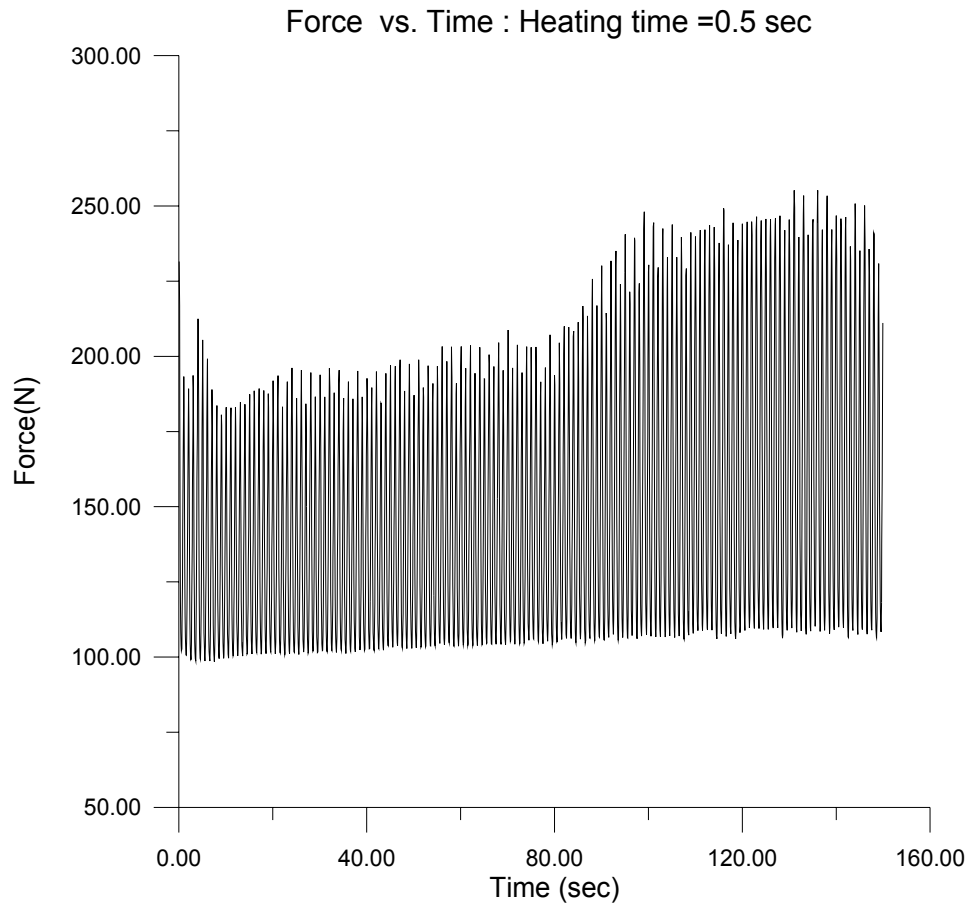
Figure 109. Force vs. time of the final actuator system at 1.0 Hz (closed-loop test).
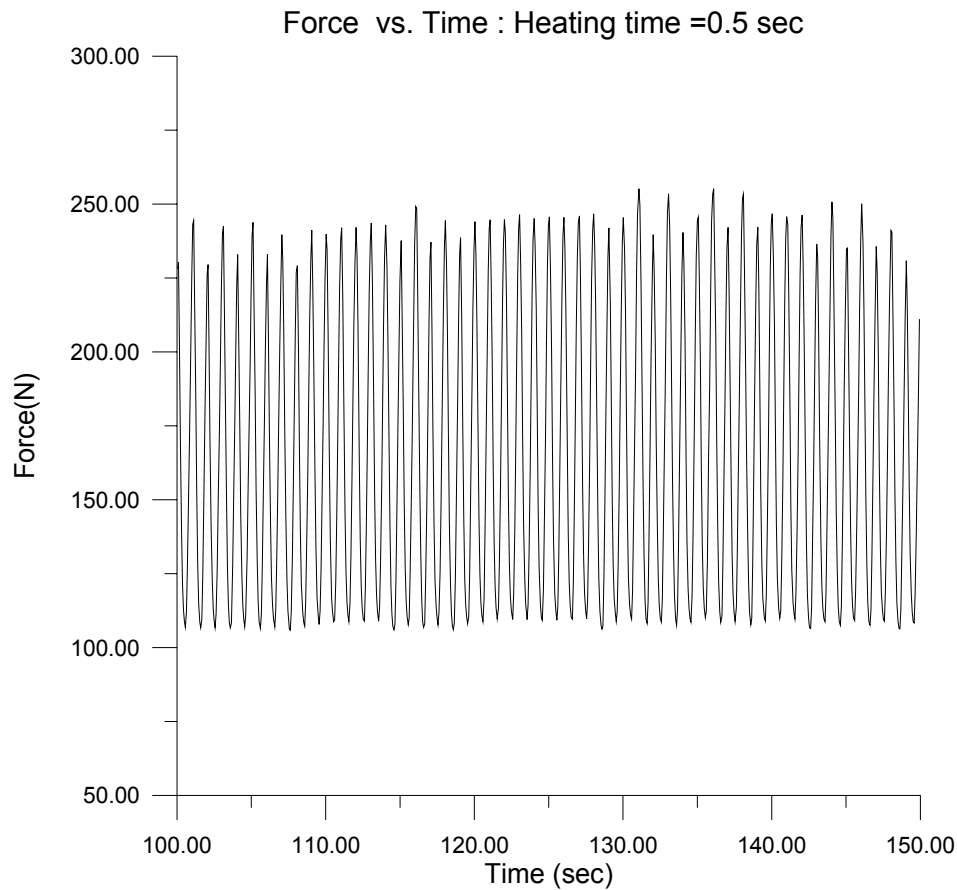
Figure 110. Force vs. time of the final actuator system at 1.0 Hz (closed-loop test, 100-150 sec).

Figure 111 and Figure 112 show the inlet and outlet temperature variations of the combustor/heat exchanger and the micro-tube heat exchanger at 1.0 Hz actuation frequency. The magnetic fields due to the DC motors and temperature variations due to the mixing caused fluctuations in the temperature data. Especially, the thermocouple at the inlet of the micro-tube heat exchanger, close to the DC motor, showed much higher data fluctuations compared to the temperature data from the other 3 thermocouples. The combustor/heat exchanger has enough power to supply the energy requirement of the

system, thus the water temperature at the outlet of the combustor/heat exchanger increased continuously during the test. From 140 seconds to 160 seconds, the fuel flow rate was decreased to prevent boiling of the hot water, as shown in Figure 111. Also the micro-tube heat exchanger has enough heat transfer rate to the surroundings, since the temperature of the heat exchanger saturated around 32 ºC or was in equilibrium state during the test at 1.0 Hz.
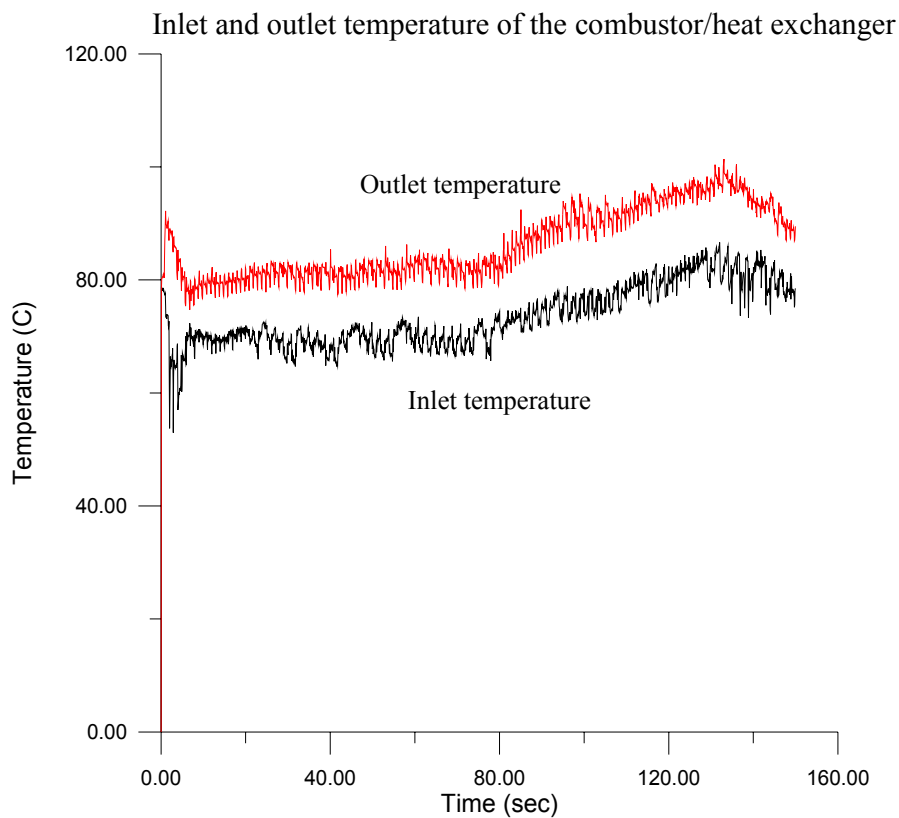
Figure 111. Inlet and outlet temperature of the combustor/heat exchanger at 1.0 Hz.
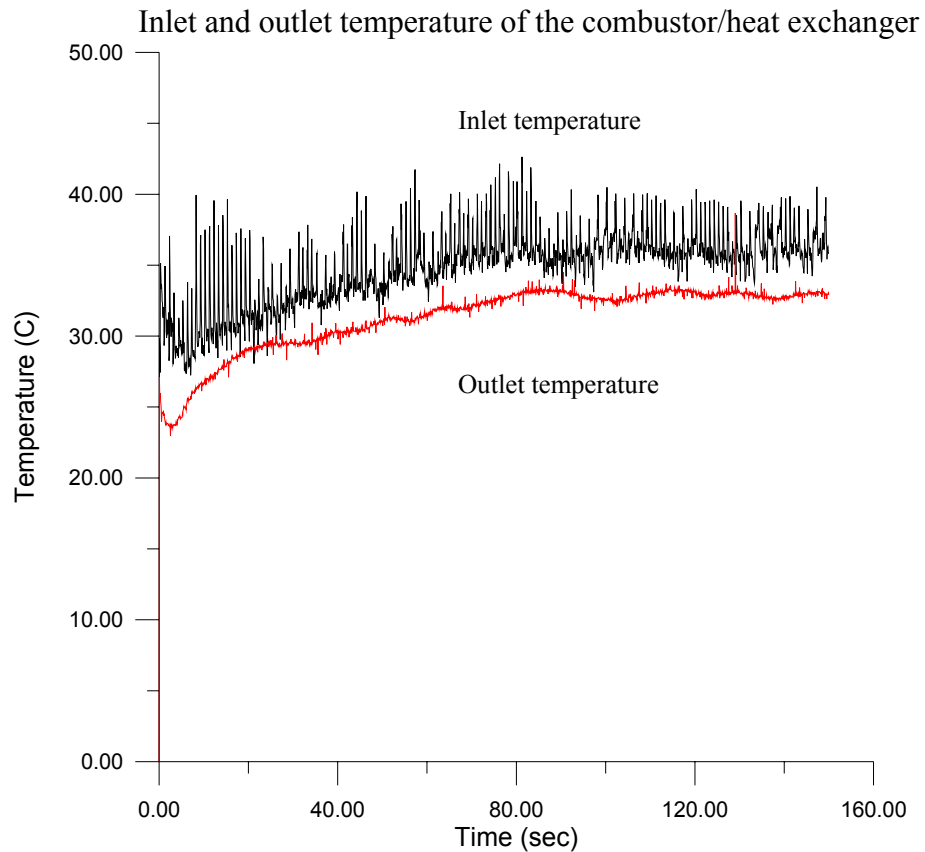
Figure 112. Inlet and outlet temperature of the micro-tube heat exchanger at 1.0 Hz.

The austenite finish transformation temperature of the SMA element was around 363 °K (90 °C) at 150 MPa. Some boiling of the water occurred in the combustor/heat exchanger, which caused some problems in operating the system, especially running the pumps. The working fluid temperature should be kept less than 90 °C to prevent boiling inside of the heat exchanger. The high boiling point of fluids such as ethylene glycol can prevent boiling and can result in higher SMA stress and strain by increasing the hot fluid temperature to more than 90 °C.

8.5. Efficiency and energy density of the final fuel-powered SMA actuator system

The energy density and efficiency of the final SMA actuator system can be obtained by measuring mass of the system, input fuel energy, input electrical power and output work (power), which is based on the experimental results, such as force, displacement and actuation frequency.

8.5.1. Energy density of the system

Table 8 shows the mass of each component and mass of the system. Table 9 shows the electrical power requirement of the SMA actuator system. The total mass of the system is 4.138 Kg including fuel and battery mass required to run 3600 cycles at 1.0 Hz actuation frequency. The energy density of propane is assumed as 50.4 MJ/Kg and the energy density of a battery (lithium-ion battery) is assumed as 540 KJ/Kg.

Table 8. Mass of the system.

Component	Unit mass (g)	Number	Total (g)
Solenoid valve	132	4	538
Brass pump	356	1	356
Plastic pump	234	1	234
SMA actuator + connectors	200	1	200
Combustor/heat exchanger	400	1	400
Heat exchanger +fan	1330	1	1330
Water + bellows	130	2	260
Tube + connectors+ check valves	300	1	300
Fuel with tank (3600 cycle)	80	1	80
Battery with cables (3600 cycle)	400	1	400
Total mass of the system			4138

Table 9. Electrical power requirement of the system.

Component	Power
Pump	12V x 2 A = 24 Watts
Valves	12V x 1 A = 12 Watts
Fan	6 Watts
Control circuit	1 Watt
Total power	43 Watts

The work and power generated during actuation were 0.5 J and 0.5 W with 2 mm displacement and 250 N at 1.0 Hz actuation frequency, respectively. Thus the energy density of the system is obtained as,

$$Energy\_density\_system = \frac{Total\_mechanical\_work}{Mass\_system} = \frac{1800J}{4.138Kg} = 435J/Kg \quad (40)$$

Where the total mechanical work, 1800 J, is given by 1 cycle work (0.5 J) x 3600 cycle.

8.5.2. Efficiency

The following calculation shows the ideal efficiency of the SMA actuator based on the results of the experimental tests, such as 2 mm displacement (2 % strain), 250 N (115 MPa stress), and 1.0 Hz actuation frequency. But the mass of SMA strip, based on the effective actuation length (4.5 inch), is 2.5g instead of 2.95g.

$$Efficiency_{ideal} = \frac{Output}{Input\ Energy} = \frac{Output(Work)}{C_p \cdot M_{SMA} \cdot \Delta T + M_{SMA} \cdot \Delta H} = 0.78\% \quad (41)$$

Where C_p=550 J/kg/°K, M_{SMA}=2.5 g, ΔT=30°K (temperature increment to induce a phase transformation of the SMA strip) and ΔH=9.138 J/g (latent heat during the heating).

Also the actual efficiency of the system can be obtained by measuring input fuel energy and output work from SMA actuator. The fuel input power was around 450 Watts at 1.0 Hz actuation frequency, thus the total input power was 493 Watts including electrical power for pumps, a fan and valves.

$$Efficiency\_system = \frac{0.5}{(450 + 43)} = 0.1\% \tag{42}$$

The system has shown the low energy efficiency like other SMA actuators [15]. Generally, SMA actuation can only be justified when its compactness and its energy density is more important than its efficiency as explained in Chapter I.

8.5.3. Energy density of a parasitic energy system

If the energy source of SMA actuator is the parasitic energy from a plant or a vehicle, an SMA actuator system would be just an SMA actuator and the energy density would increase significantly according as the number of actuation cycle increases. The parasitic actuator system will not need any additional devices and power by using the existing devices. The following calculation of energy density is based on 3600 cycles at 1.0 Hz actuation frequency.

$$Energy\_density = \frac{Total\_mechanical\_work}{Mass\_SMA\_actuator} = \frac{1800J}{0.2Kg} = 9000J/Kg \tag{43}$$

Also the energy density of SMA material at 3600 cycles becomes tremendous in parasitic energy system, as the number of cycles increases.

$$Energy\_density\_SMA\_strip = \frac{Total\_mechanical\_work}{Mass\_SMA} = \frac{1800J}{2.95g} = 610.2J/g \tag{44}$$

These results show that the energy density of a parasitic energy system by equation (43) is much higher than the energy density of the final actuator system by equation (40). Thus, using parasitic heat from a plant or a vehicle can result in high energy density SMA actuator. Table 10 shows energy densities and efficiencies of systems.

Table 10. Energy densities and efficiencies under 3600 cycles at 1.0 Hz.

Work (1 cycle)	2 mm x 250 N = 0.5 J
Power	2 mm x 250 N = 0.5 W
Energy density of the system	435 J/Kg
Energy density of a parasitic energy system	9000 J/Kg
Energy density of SMA material of a parasitic energy system	610.2 J/g
Ideal efficiency of the system	0.78 %
Actual efficiency of the system	0.1 %

8.6. Conclusions

The actuator system was modified and improved to increase the actuation frequency and to achieve high energy and power densities. A rectangular channel, with a rectangular piston running along it, was selected for the final actuator system to house the SMA strip in order to decrease mixing in the SMA actuator system. The control logic operating the heating and cooling circuits, alternatively, according to the SMA actuation cycle, worked well along with the Hall effect sensor. The final system was integrated and included the multi-channel combustor/heat exchanger, a small brass gear pump and the

micro-tube heat exchanger. The final system was focused on miniaturization and compactness. The system was able to work effectively with small amounts hot and cold water circulated by the pumps during the tests. The strip had a 0.9 mm x 2.5 mm (0.1 inch x 0.034 inch) cross-sectional area, which is 1/5 of the strip for the second-generation actuator system. The actuation frequency of the final system was around 1.0 Hz generating 116 MPa recovery stress and 2 mm strain in closed-loop operation. Since there were no differences between the results of the open-loop operation and the results of the closed-loop operation, the mixing in the final system seemed to have decreased significantly. The combustor/heat exchanger and the micro-tube heat exchanger demonstrated good performance during the actuation tests and were able to meet the energy requirements of the system. The energy density of the final SMA actuator system is 435 J/Kg at 1 hour operation with 1.0 Hz actuation frequency. Also the energy density of a parasitic energy system is 9000 J/kg, which shows energy saving benefits that SMAs present to us for systems with abundant parasitic heat. Heating of the SMA by utilizing existing parasitic energy in a vehicle/plant can result in high energy density.

The actuation frequency of the system can be improved by increasing the velocity of hot fluid, as well as utilizing a high boiling point fluid, such as Ethylene Glycol. The channel size is still big compared to the SMA strip size due to the size of the screws, which are used to hold together the piston parts. Thus, more optimization of the system is possible, will increase the actuation frequency and will finally enhance the energy density of the system.

The estimated frequency obtained from the numerical analysis was 1.25 Hz under 150 MPa, while the fastest frequency attainable for close-loop tests was 1.0 Hz under 114 MPa. Considering the pressure loss in the channel due to the movement of the piston and discontinuous flow due to the on/off operation of pump, the numerical result shows good agreement with the experimental tests. Hence the numerical analysis is useful in designing the SMA actuator, predicting the available actuation frequency of the system, and determining the optimal channel geometry. The electric energy, needed to run the pumps, solenoid valves and the fan, was much smaller than that required for resistive heating and forced convection cooling system of such as a SMA actuator system like one used in [26] to actuate a biomimetic hydrofoil.

CHAPTER IX

CONCLUSIONS

9. Summary and conclusions

9.1. Summary

This research has addressed the development of a fuel powered compact SMA actuator system and its main components, such as the SMA actuator, the miniature gear pump, the multi-channel combustor/heat exchanger and the micro-tube heat exchanger. Energy density and efficiency comparisons were carried out in order to select the best system, which has the highest energy density and power density. From these comparisons, the combustor-SMA actuator system was chosen, and forced convection heating and cooling heat transfer was adopted for the SMA actuator system. To determine optimal channel geometry and to estimate the period of the heating and cooling cycles (i.e., actuation frequency), numerical analyses were carried out with commercial packages, such as FLUENT and GAMBIT. The numerical analysis suggested that a rectangular cross-section channel results in better heat transfer rate to the SMA strip than a circular channel. Hence, for the final SMA actuator, a rectangular channel was selected. Hall effect sensors and a rectangular piston with a magnet housed on top of the piston were utilized in order to decrease the mixing between the hot and cold water. The mixing was caused by sharing common flow paths such as the SMA actuator channel. The final actuator system was composed of pumps, solenoid valves, check valves, bellows, a

micro-tube heat exchanger, a multi-channel combustor/heat exchanger and a control unit. The multi-channel combustor/heat exchanger was utilized to burn the fuel and to transfer that energy to the fluid passing through the heat exchanger. The operation of the combustor/heat exchanger was based on the laminar convective heat transfer mechanisms. The compressed air and fuel were introduced into the mixing chamber of the combustor/heat exchanger and were burned on a porous metal sheet, which generated a laminar blue flame and worked as a flash arrestor. The exhaust gas passed through the multiple channels of the combustor and transferred most of its energy to the heat exchanger and finally to the fluid. This micro-tube heat exchanger was used for dissipating, to the surroundings, the energy obtained by the cooling fluid/water from the SMA strip and the mixing between hot and cold fluids. The micro-tube heat exchanger was composed of 561 copper tubes and was operated under laminar flow conditions like the combustor/heat exchanger. These two main components utilized micro/miniature technology and were machined by using CNC drilling and CNC cutting.

9.2. Conclusions

9.2.1. Combustor/Heat exchanger

The size of the second-generation combustor/heat exchanger is 81.3 mm x 76.2 mm, which is about ¼ of the first-generation combustor/heat exchanger. The channel size of the heat exchanger is 7.62 mm x 0.81 mm (spacing: 0.81 mm), while the channel size of the combustor side is 2.5 mm x 0.81 mm (spacing: 0.81 mm). The total number of channels is 39. The combustor/heat exchanger power output ranged up to 800 Watts. The

efficiency of the combustor/heat exchanger was around 70 %, which is higher than that of the commercial propane burner. The multi-channel combustor/heat exchanger achieved high compactness, lightness and high efficiency, which can make the SMA actuator system more compact. The flame was contained in the combustion chamber and the temperature of the exit gas from the channels of the combustor was much lower than the flame temperature, thus it will be possible to make a portable actuator system regardless of the high temperature of the flame. The numerical analysis was useful in the designing stage of the multi-channel combustor/heat exchanger.

The test results of the final actuator system at 1.0 Hz actuation frequency demonstrated that the combustor/heat exchanger has enough power output to meet the energy requirements of the system.

9.2.2. Micro-tube heat exchanger

The micro-tube heat exchanger is composed of inlet and outlet fittings, multi-hole tube headers, a fan and 561 copper micro-tubes. The size of the micro-tube heat exchanger is 114.3 mm x 178 mm x 28 mm (core size=100 mm x 140 mm x 20 mm). It dissipates around 380 Watts under a 24 °C inlet temperature difference between the two fluids (air and water). The numerical calculations have shown good agreements with the results of the experimental tests. The numerical analysis was useful in the designing stage, for example, in determining the volume and geometric parameters of the heat exchanger. Using the micro-tube heat exchanger has resulted in high compactness and high heat-transfer-rate per volume compared to commercial heat exchangers. These types of heat

exchangers can be run under high operating pressure and have less leakage compared to the micro channel heat exchangers [23], that are fabricated by chemical processing and LIGA. Also the inlet air velocity has strong effects on the performance of the micro-tube heat exchanger.

9.2.3. Fuel-powered compact SMA actuator

The first-generation actuator system was composed of a pump, four solenoid valves, a bellows, a radiator and a combustor/heat exchanger. The SMA element was embedded in a circular silicon tubing. The mixing, between the hot and cold fluids caused by sharing common flow paths, such as the actuator channel and the inside volume of the pump, resulted in the low actuation frequency in the closed-loop operation. The first-generation actuator was modified and improved to increase the actuation frequency and to achieve high energy and power densities. A rectangular channel, with a rectangular piston running along it, was selected to house the SMA strip in order to decrease mixing in the SMA actuator system. The actuation frequency of the second-generation actuator system was 0.25 Hz, which was 2.5 times that of the first-generation actuator system under closed-loop operation. The final actuator system was focused on miniaturization and optimization and was based on the second-generation actuator system. The size of the SMA strip of the final system was 0.9 mm x 2.5 mm, which is around 1/5 times of the strip for the second-generation actuator system. The final system was integrated and included the developed multi-channel combustor/heat exchanger, a small brass gear pump and the micro-tube heat exchanger. The actuation frequency of the final system

was around 1.0 Hz generating 100 MPa recovery stress and 2 mm displacement in closed-loop operation. The energy density of the final SMA actuator system is 435 J/Kg at 1 hour operation with 1.0 Hz actuation frequency. Since there were no differences between the results of the open-loop operation and the results of the closed-loop operation, the mixing in the final system seemed to have decreased a lot. The combustor/heat exchanger and the micro-tube heat exchanger demonstrated good performance during the actuation tests and were able to meet the energy requirements of the system. The results of the numerical heat transfer analysis were useful and compared reasonably to the results of experimental tests. In designing a thermally induced SMA actuator, the transient heat transfer analysis with the SMA latent taken into account, should be carried out numerically to determine design parameters and operating conditions. The electric energy, needed to run the pumps, solenoid valves and the fan, was much smaller that that required for resistive heating and forced convection cooling of the actuator system utilized for a biomimetic hydrofoil we previously developed [16, 26]. Fuel, such as butane and propane, is relatively cheap, easy to handle and easy to store in compact module like gas cartridges. Hence the operating cost of a fuel-powered actuator system will be lower compared to that of batteries and fuel cells. This research also demonstrates the energy saving benefits that SMAs present to us with for systems with abundant parasitic heat. Heating of the SMA by utilizing existing parasitic heat in a vehicle/plant will yield relatively high energy density. The fuel-powered compact SMA actuator system is the first SMA actuator system in adopting a forced convection heating mechanism instead of resistive heating of the SMA strip. The fuel-powered SMA

actuator system can be operated in a stand-alone mode, needing, besides the fuel, a small battery for running the small pumps, the fan and the electronic circuitry. Hence this SMA actuator system can be utilized as a self-contained actuator system, independent of other supporting hardware n the plant it is used in. Thus, its use can reduce complexity, weight, and maintenance costs, while increasing the reliability and compactness. The system can replace current actuators such as hydraulic actuators which are maintenance intensive and are prone to leakage as they operate under in high pressures.

9.3. Future tasks

The final SMA actuator system demonstrated its potential for compactness and miniaturization by using the chemical energy of fuels as its main energy source. The built actuator system is not optimally compact even though micro/miniature technology was applied for the development of the multi-channel combustor/heat exchanger and the micro-tube heat exchanger in order to increase the compactness of the system. The combustor/heat exchanger seems to have abundant power, so it can be optimized based on the actual power requirements of the heating circuit. An oxygen and fuel supply system for the combustor will be more compact and lighter compared to the air and fuel supply system currently used. The high boiling point of fluids such as ethylene glycol can prevent boiling, can result in higher SMA stress and strain by increasing the hot fluid temperature and can increase the stability of the system. Smaller size of channels in the combustor/heat exchanger and smaller diameter of the micro-tubes in the heat exchanger will increase the compactness and power to volume ratio even though it will

cause higher pressure losses. Thus the study and optimization of the tube array configuration and tube size in the micro-tube heat exchanger, and the channel size of the combustor/heat exchanger would be useful. The temperature of the combustion products entering the combustor channels and the actual temperature variation along the channels were not discussed in this research. Also the composition of the exhaust gas from the combustor was not analyzed. Future work on these temperature variations and quantitative NO_x emissions analysis of the combustor would be useful. The Nusselt number or heat transfer coefficient used for the design of the micro-tube heat exchanger should be improved or updated based on the experimental tests to avoid underestimation of the performance. Work on the numerical heat transfer analysis of the SMA actuator channel with commercial packages based on the actual flow pattern in the channel, rather than using constant flow pattern would be useful.

REFERENCES

[1] Funakubo H 1987 *Shape Memory Alloys* (New York: Gordon and Breach Science)

[2] Brinson L C, Bekker A and Hwang S 1994 Temperature induced deformation in shape memory alloys *Active Materials and Smart Structures Proceedings* vol **2427** 234-244

[3] Olsen G B and Cohen M 1982 Stress assisted isothermal martensite transformation application to TRIP steels *Metall. Trans. A* **13A**, 1907-1914

[4] Buehler W J and Wiley R C 1965 *Nickel-base alloys* U.S. Patent 3, 174, 851

[5] Mavroidis C, Pfeiffer C and Mosley M 2000 Conventional actuators, shape memory alloys, and electrorheological fluids In: Bar-Cohen Y (Editor) *Automation, Miniature Robotics and Sensors for Non-Destructive Testing and Evaluation* Ch. 5 pp 189-214 (Columbus OH: American Society for Nondestructive Testing)

[6] Entchev P B 2002 Micromechanical modeling of porous shape memory alloys *Ph.D dissertation* Texas A&M University

[7] Lexcellent C., Leclercq S, Gabry B and Bourbon G 2000 The two way shape memory effect of shape memory alloys: an experimental study and a phenomenological model *International Journal of Plasticity* **16** 1155-1168

[8] Godard O J 2002 Space applications of shape memory alloys *MS thesis* Texas A&M University

[9] Ikuta K 1990 Micro/miniature shape memory alloy actuator *Proceedings of the IEEE International Conference on Robotics and Automation* pp 2156-2161 (Cincinnati, OH)

[10] Stalmans R and Humbeeck J V 1994 Shape memory alloys: functional and smart *Proceedings of 4th International Conference on New Actuators* pp 312-316 (Bremen, Germany)

[11] Peffer A, Fosness E, Carpenter B, and Denoyer K 2000 On orbit experiments and applications of shape memory alloy mechanisms *Proceedings of Smart Structures and Materials 2000: Industrial and Commercial Applications of Smart Structures, SPIE* vol. **3991** pp187-194

[12] Lagoudas D C, Rediniotis O K and Khan M M 1999 Applications of shape memory alloys to bioengineering and biomedical technology *Proceedings of 4th International Workshop on Matermatical Methods in Scattering Theory and Biomedical Technology* pp 195-207 (Perdika, Greece)

[13] Gil FJ and Planell JA 1999 Thermal efficiencies of NiTiCu shape memory alloys *Thermochimica Acta* **327** 151-154

[14] Reynaerts D and Brussel H V 1998 Design aspects of shape memory actuators *Mechatronics* **8** 635-656

[15] Russel R A and Gorbeit R B 1995 Improving the response of SMA actuators *Proceedings of IEEE International Conference on Robotics and Automation* vol 3 pp 2299-2304

[16] Wilson L N 2000 The Development of a shape memory alloy actuated biomimetic hydrofoil *MS thesis* Texas A&M University

[17] Boyd, J. G and Lagoudas, D.C 1994 Thermomechanical response of shape memory composites *J. Intell. Mater. Struct* **5** 336-346

[18] Bhattcharyya A, Lagoudas D C, Wang Y and Kinra V K 1995 On the role of thermoelectric heat transfer in the design of SMA actuators; theoretical modeling and experiment *Smart Materials and Structures* **4** 252-263

[19] Johnson A D 1977 *Memory alloy heat engine and method of operation* U.S. Patent 4,055,955

[20] Ginell W S, McNichols J L, and Cory J S 1978 Low grade thermal energy conversion : Joule effect heat engines *Intersociety Conference on Environmental Systems* ASME Paper No. **78-ENAS-7** (San Diego, CA)

[21] Aguado-Monsonet M A and Bonotoux L *New battery technologies: promising developments* Institute for Prospective Technological Studies webpage http://www.jrc.es/iptsreport/vol36/english/ENE1E366.htm [Accessed August 2003]

[22] Drost M K, Call C J, Cuta J M and Wegeng R S 1997 Microchannel integrated evaporator/combustor thermal processes *Journal of Microscale Thermophysics Engineering* **1**(4) 321-333

[23] Harris C, Despa M, and Kelly K 2000 Design and fabrication of a cross flow micro heat exchanger *Journal of Microelectromechanical Systems* **9**(4) 502-508

[24] Rediniotis O K, Lagoudas D C, Garner L and Wilson N 1998 Experiments and analysis of an active hydrofoil with SMA actuators *36th AIAA Aerospace Sciences Meeting* AIAA Paper No. **98-0102** (Reno, NV)

[25] Webb G, Wilson L, Lagoudas D C and Rediniotis O.K 2000 Adaptive control of shape memory alloy actuators for underwater biomimetic applications *AIAA Journal* **38** (2) 325-334

[26] Rediniotis O K, Lagoudas D C and Wilson L N 2000 Development of a shape memory alloy actuated underwater biomimetic vehicle *38th Aerospace Science Meeting and Exhibit* AIAA Paper No. **2000-0522** (Reno, NV)

[27] Lin B 1999 Conceptual design and modeling of hydrogen fuel cell scooters for urban Asia *MS thesis* Princeton University

[28] Fuel Cell Technologies Ltd *underwater vehicle power* webpage http://www.fct.ca/alum.html [Accessed August 2003]

[29] Tompson M *Generic battery technology comparison* webpage http://www.madkatz.com/ev/batteryTechnologyComparison.html [Accessed August 2003]

[30] Lagoudas D C and Bhattcharyya A 1998 Modeling of thin layer extensional thermoelectric SMA actuators *International Journal of Solids Structures* **35** 331-362

[31] Jardine A P 1989 Calorimetric techniques for the evaluation of thermal efficiencies of shape memory alloys *Journal of Materials Science* **24** 2587-2593

[32] Jardine A P 1998 Calorimetric measurements of transformation thermodynamics and thermal efficiencies of NiTi helices *Journal of Materials Science* **23** 3314-3320

[33] Cunningham B and Ashbee K H G 1977 Marmen engines *Acta Metallurgica* **25** 1315-1321

[34] Miller D A and Lagoudas D C 2000 Thermo-mechanical characterization of NiTiCu and NiTi SMA actuators: Influence of plastic strains *Smart Materials and Structures* **9** (5**)** 275-293

[35] Rediniotis O K, Lagoudas D C, Jun H Y and Allen R D 2002 Fuel-powered compact SMA actuator *SPIE's 10th Annual International Symposium on Smart Structures and Materials* Paper No. **4698-44** (San Diego, CA)

[36] Rumminger M D 1996 Numerical and experimental investigation of heat transfer and pollutant formation in porous direct-fired radiant burners *Ph.D. dissertation* University of California, Berkeley

[37] ACOTECH *Metal fiber burners* Webpage http://www.acotech.com/mefibu02.htm [Accessed September 2003]

[38] Alzeta Corporation 2001 Report for California Energy Commission *Low NOx gas turbine combustors for distributed power generation* web page http://www.energy.ca.gov/reports/2002_01-11_600-01-002.PDF [Accessed August 2003]

[39] Cho K W, Han K, Lee Y K, Noh D, Yoon H M, Riu K, Lee K 2001 Premixed combustion of coke oven gas in a metallic fiber mat *Fuel* **80** 1033-1036

[40] Eco Ceramics *Ceramic foam burner* web page

http://www.ecoceramics.nl/foamburners/datashee/ecofoamdatasheet.htm

[Accessed September 2003]

[41] Trimis D, Durst F, Pickenacker O and Pickenacker K 1997 Porous medium combustor versus combustion systems with free flames *Advances in Heat Transfer Enhancement and Energy Conservation* pp 339-345 (Guangzhou, China: South China University of Technology Press)

[42] Knight R W, Hall D J, Goodling J S, and Jaeger R C 1992 Heat sink optimization with application to microchannels *IEEE Transactions on Components, Hybrids, and Manufacturing Technology* **15** (5**)** 832-842

[43] Frank M. White 1996 *Fluid Mechanics* 2nd edn (New York: McGraw-Hill)

[44] Frank P. Incropera and David P.De Witt 1990 *Fundamentals of Heat and Mass Transfer* 3rd edn (New York: John Wiley & Sons)

[45] Richard E. Sonntag, Gordon J. Van Wylen 1988 *Fundamentals of Classical Thermodynamics* 3rd edn (New York: McGraw-Hill)

[46] Paitoonsurikarn S, Kasagi N, and Suzuki Y 2000 Optimal design of micro bare-tube heat exchanger *Proc. Symp. Energy Engineering* vol 3 pp 972-979 (HongKong, China)

[47] Boman A and Doty D 2002 Design and manufacture of ultra-low-mass, cryogenic heat exchangers *Cryogenics* **41** 797-803

[48] Mills A F 1992 *Heat Transfer* (Boston: Irwin)

[49] Zhukauskas, A A 1972 Heat transfer from tubes in cross flow *Advances in Heat Transfer* **8** 93-160

[50] Greylor Pump Company *Miniature gear pumps* webpage

http://ww.greylor.com/pq_spec.htm [Accessed September 2003]

VITA

Hyoung Yoll Jun

Permanent address

> 7-31 2 Dong Guworl, NamDong Gu
> Inchun, Korea 405-220
> 82-32-467-8981
> hyounyoll@hotmail.com

Personal

> Date of birth: September 3, 1969
> Place of birth: Inchun, Korea

Education

Ph.D.	Aerospace Engineering (December 2003) Texas A&M University, College Station, TX.
M.S.	Aerospace Engineering (February 1996) Inha University, Inchun, Korea.
B.S.	Aerospace Engineering (February 1994) Inha University, Inchun, Korea.

Professional Experience

> Graduate Research Assistant (August 1999 ~ December 2003)
> Department of Aerospace Engineering
> Texas A&M University, College Station, TX.
>
> Thermal Engineer (November 1997 ~ March 1998)
> Hyundai Electronics Ind. Co., LTD, Satellite Business Division
>
> Thermal Engineer (February 1996 ~ August 1997)
> Korea Telecom, Satellite Business Division
>
> Korea Navy (January 1991 ~ June 1992)